Density fitted local configuration interaction singles method for calculating optical band gaps in periodic systems

Dissertation

zur Erlangung des Doktorgrades der Naturwissenschaften (Dr. rer. nat.)
der Fakultät
- Chemie und Pharmazie -
der Universität Regensburg

vorgelegt von

Marco Lorenz

aus Regensburg

2012

Promotionsgesuch eingereicht am:	20.09.2012
Tag des Kolloquiums:	09.11.2012
Diese Arbeit wurde angeleitet von:	Prof. Dr. Martin Schütz
Prüfungsausschuss:	
Vorsitzender:	Prof. Dr. Henri Brunner
Erstgutachter:	Prof. Dr. Martin Schütz
Zweitgutachter:	Prof. Dr. Bernhard Dick
Drittprüfer:	Prof. Dr. Arno Pfitzner

For the 0.1%.

Die Ergebnisse dieser Arbeit sind bereits veröffentlicht worden:

Chapter 2

M. Lorenz, D. Usvyat and M. Schütz

"Local ab initio methods for calculating optical band gaps in periodic systems: I. Periodic density fitted local configuration interaction singles method for polymers"

Journal of Chemical Physics

134, 094101 (2011), doi: 10.1063/1.3554209

Chapter 3

M. Lorenz, L. Maschio, M. Schütz and D. Usvyat

"Local ab initio methods for calculating optical band gaps in periodic systems: II. Periodic density fitted local configuration interaction singles method for solids"

Journal of Chemical Physics

submitted, xy (2012)

Chapter 4

C. Pisani, M. Schütz, S. Casassa, D. Usvyat, L. Maschio, M. Lorenz and A. Erba

"CRYSCOR: a program for the post-Hartree-Fock treatment of periodic systems"

Physical Chemistry Chemical Physics

14, 7615 (2012), doi: 10.1039/C2CP23927B

Acknowledgements

An dieser Stelle möchte ich mich bedanken bei:

Prof. Dr. Martin Schütz für die interessante und herausfordernde Aufgabenstellung, seine wissenschaftlichen Anregungen und intensive Förderung, sowie seine konstruktive Kritik,

Prof. Dr. Bernhard Dick für die Erstellung des Zweitgutachtens,

Dr. Denis Usvyat für die wissenschaftliche Betreuung, seine konstruktive Kritik und seine Auskunftsfreudigkeit zu jedweden wissenschaftlichen Unklarheiten,

Dr. Lorenzo Maschio für die fruchtbare Zusammenarbeit in Turin und via Skype,

Prof. Dr. Cesare Pisani (†) für die Gastfreundschaft in Turin, seine wissenschaftliche Unterstützung und vor allem die Ehre, ihn gekannt zu haben,

Prof. Dr. Roberto Dovesi für die Gastfreundschaft in Turin und seine wissenschaftliche Unterstützung,

Matteo Ferrabone für seine Hilfe zum Verstehen des Hobbit-Codes,

meinen ehemaligen Kollegen Keyarash Sadeghian, Daniel Kats und Dominik Schemmel, sowie meinen aktuellen Kollegen Stefan Loibl, Thomas

Merz, Katrin Ledermüller, Oliver Masur, Gero Wälz, David David, Alexander Schinabeck und Petra Eichenseher für die angenehme Büroatmosphäre,

Klaus Ziereis für seine Hilfe in technischen Dingen,

sowie der Turiner Arbeitsgruppe (ehemalig, temporär und aktuell): Dr. Alessandro Erba, Dr. Silvia Casassa, Gustavo Do Amaral Sophia, Prof. Dr. Michel Rérat, Dr. Raffaella Demichelis, Dr. Marco De La Pierre, Elisa Albanese, Jacopo Baima und Davide Presti für eine sonnige Zeit in Turin,

meinen ehemaligen Kommilitonen Roland, Sebastian, Christoph, Ulrike, Thomas und Daniela für eine schöne Zeit außerhalb der Uni,

sowie Elke, Markus, Lydia, Frank, Christine, Jürgen, Alexandra, Simona und Naomi für viele interessante Einsichten, ihre moralische Unterstützung und ihre Außergewöhlichkeit,

und insbesondere meinen Eltern und meiner Schwester Silke für ihre Unterstützung und Hilfe in jeglicher Art und Weise.

Publications and Presentations

Publications

M. Schütz, D. Usvyat, **M. Lorenz**, C. Pisani, L. Maschio, S. Casassa, M. Halo
"Density fitting for correlated calculations in periodic systems", Accurate Condensed-Phase Quantum Chemistry,
Series: Computation in Chemistry, 27 (2010)

M. Lorenz, D. Usvyat and M. Schütz
"Local ab initio methods for calculating optical band gaps in periodic systems: I. Periodic density fitted local configuration interaction singles method for polymers"
Journal of Chemical Physics
134, 094101 (2011), doi: 10.1063/1.3554209

C. Pisani, M. Schütz, S. Casassa, D. Usvyat, L. Maschio, **M. Lorenz** and A. Erba
"CRYSCOR: a program for the post-Hartree-Fock treatment of periodic systems"
Physical Chemistry Chemical Physics
14, 7615 (2012), doi: 10.1039/C2CP23927B

M. Lorenz, L. Maschio, M. Schütz and D. Usvyat
"Local ab initio methods for calculating optical band gaps in periodic systems: II. Periodic density fitted local configuration interaction singles

method for solids"
Journal of Chemical Physics
submitted, xy (2012)

Poster Presentations

M. Lorenz, D. Usvyat, L. Maschio, M. Schütz
"Periodic Density Fitted Local CIS"
SPP1145 Meeting, Bad Herrenalb (Germany), March 2010

M. Lorenz, L. Maschio, D. Usvyat, M. Schütz
"Local density-fitted Periodic CIS Method for Polymers"
Symposium on Theoretical Chemistry, Münster (Germany), September 2010

M. Lorenz, L. Maschio, D. Usvyat and M. Schütz
"Local CIS method for excited states in solids"
Symposium on Theoretical Chemistry, Karlsruhe (Germany), September 2012

Oral Presentations

M. Lorenz
"Calculating band gaps using the periodic local CIS method"
Seminar talk, Torino (Italy), March 2011

M. Lorenz
"Local CIS method for excited states in periodic systems"
Invited talk, Conference on *Ab initio Modeling in Solid State Chemistry*, Torino (Italy), September 2011

”Denn die Sache ist nicht in ihrem Zwecke erschöpft, sondern in ihrer Ausführung, noch ist das Resultat das wirkliche Ganze, sondern es zusammen mit seinem Werden.“

G. W. F. Hegel

Contents

Chapter 1

Introduction

The interaction of matter with electromagnetic radiation is one of the most interesting and important phenomena studied by natural sciences. Many accomplishments of today's life deal with the interaction of matter with light, for instance the bleaching of pulp with UV-light and without chlorine or the infrared remote control, to name two examples of a very broad field. Photosynthesis is one of the most important biochemical processes on earth. Photovoltaic cells (mainly built of silicon crystals) contribute to the production of electricity - and therefore to the driving force of modern society. Electricity in turn provides a possibility to emit light. There is a billion-dollar industry for light emitting devices (LEDs) using semiconducting materials or organic molecules (OLEDs) to produce visible light with very high efficiency, replacing light bulbs emitting infrared rather than visible light (efficiency less than 5%).

For all that and lot of other absorption and emission processes, properties of materials have to be identified and understood. In the framework of quantum chemistry, however, the basis to this knowledge is the investigation of electronically excited states.

Molecular quantum chemical investigations are far ahead of their solid state counterparts. Nowadays, there is usually a gap of about 20 years, until molecular techniques are translated to the solid state, because of

the more complex theory and intrinsically more complex algorithms, as well as the much higher computational effort. The Hartree-Fock method, published in 1930 [1] was first adopted for solids even more than 40 years later in 1973 by Euwema *et al.* [2] and made generally available from 1980 on by Pisani and Dovesi [3]. Local Møller-Pleset perturbation theory of second order (LMP2), first proposed for molecules by Pulay and Saebø in 1986 [4] took 19 years to reach the periodic case [5], with the density fitting approximation even more [6].

The configuration interaction singles (CIS) approach for excited states, first used under this name by Foresman *et al.* [7] in 1992, is seen there a first time as a starting point in the quantum chemical hierarchy of methods. Neither in this nor in other molecular CIS calculation, the robust three-term density fitting approximation [8, 9], which is essential for the efficiency of the calculation, but at the same time provides a major algorithmic complication, has ever been applied.

Now, 20 years later, within the framework of this dissertation, the first pure CIS method for solids (using the density fitting approximation and local orbitals) has been developed and test-calculations have been carried out.

1.1 Molecules

1.1.1 Excited state CIS theory

The CIS method approximates the exact non-relativistic wavefunction $|\Psi\rangle$ with

$$|\Psi\rangle \approx c_0|0\rangle + \sum_{ia} c_a^i|\Phi_i^a\rangle, \tag{1.1}$$

where $|0\rangle$ is the Hartree-Fock reference, i are occupied and a are virtual orbitals, $|\Phi_i^a\rangle$ are singly excited determinants, and c_0 and c_a^i denote the corresponding amplitudes, respectively.

For the ground state, the CIS determinant, due to the Brillouin theorem, does not improve the Hartree-Fock wavefunction. All amplitudes except c_0 are then zero, as well as the correlation energy.

The CIS wavefunction of the first excited state can then be obtained by projecting out the ground state wavefunction, which consists in this very case, as stated above, of the Hartree-Fock determinant. The projection operator $\hat{P}$ then becomes:

$$\hat{P} = 1 - |0\rangle\langle 0|, \tag{1.2}$$

and appliance to Eq. (1.1) leads to the excited state CIS wavefunction:

$$\begin{aligned} |\mathrm{CIS}\rangle = \hat{P}\Big(c_0|0\rangle + \sum_{ia} c_a^i|\Phi_i^a\rangle\Big) &= \underbrace{c_0|0\rangle - c_0|0\rangle\langle 0|0\rangle}_{=0} \\ &\quad + \sum_{ia} c_a^i|\Phi_i^a\rangle - \underbrace{\sum_{ia} c_a^i|0\rangle\langle 0|\Phi_i^a\rangle}_{=0} \\ &= \sum_{ia} c_a^i|\Phi_i^a\rangle, \end{aligned} \tag{1.3}$$

where the orthonormality of the Hartree-Fock wavefunction and its orthogonality to the singly excited determinants has been exploited. The CIS wavefunction can be rewritten as:

$$|\mathrm{CIS}\rangle = \sum_{ia} c_a^i|\Phi_i^a\rangle = \sum_{ia} c_a^i\hat{\tau}_i^a|0\rangle = \hat{C}_1|0\rangle, \tag{1.4}$$

where $\hat{\tau}_i^a$ is an excitation operator exciting an electron from the occupied orbital i into the virtual orbital a.

In our approach, the CIS Schrödinger equation,

$$\hat{H}\hat{C}_1|0\rangle = \omega_{\mathrm{CIS}}\hat{C}_1|0\rangle, \tag{1.5}$$

where $\hat{H}$ is the non-relativistic normal-ordered Hamilton operator, is projected onto the singly excited manifold $\langle\Phi_i^a|$ to obtain the eigenvalue and eigenvector equations:

$$\langle\Phi_i^a|\hat{H}\hat{C}_1|0\rangle = \omega_{\mathrm{CIS}}\langle\Phi_i^a|\hat{C}_1|0\rangle, \tag{1.6}$$

where ω_{CIS} denotes the CIS excitation energy. From all excitations on the right hand side of Eq. (1.6), only the one which excites from i to a survives, because of the orthogonality of the singly excited determinants, therefore it remains:

$$\langle \Phi_i^a | \hat{H} \hat{C}_1 | 0 \rangle = \omega_{\mathrm{CIS}} c_a^i. \tag{1.7}$$

Diagonalizing the matrix $\langle \Phi_i^a | \hat{H} \hat{C}_1 | 0 \rangle$ on the left hand side of Eq. (1.7) provides the CIS energies ω_{CIS} and the CIS coefficients c_a^i. Usually only few lowest eigenvalues are of interest, and the direct diagonalization is substituted by a smaller space diagonalisation procedure (Davidson diagonalization [10], *vide infra* Sec. 1.2.3).

The working equations in terms of integrals and coefficients can be obtained from Eq. (1.7) by applying the diagrammatic technique [11].

1.1.2 Diagrammatic technique for spatial orbitals

The diagrammatic technique is a graph method to construct algebraical expressions for the energy and amplitude equations. The Fock operator and Fluctuation operator, defined as the difference between the Hamilton (in the normal ordering) and Fock operators, are represented as horizontal (interaction) lines

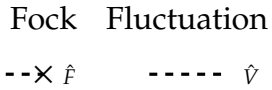

The Singles and Doubles operators are denoted as:

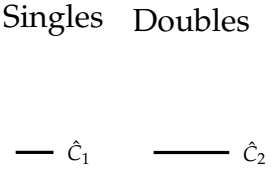

Those operators can be connected with vertical lines, representing hole (occupied orbitals) and particle (virtual orbitals) states:

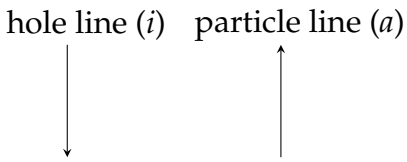

For each action on an electron, there originates a pair of hole and particle lines from the interaction line, *i.e.*, one ingoing and one outgoing line. Those points are called vertices. Consequently, one-electron operators, as Fock and Singles operator, have one vertex, whereas two-electron operators, as Fluctuation and Doubles operators, have two vertices, and so on. The top of the diagram then is assigned to the *bra* side of the expression, the bottom to the *ket* side, *e.g.* in

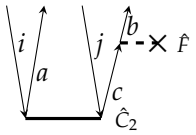

the *bra* side of the expression holds double excitations (4 external lines), $\langle \Phi_{ij}^{ab}|$, while the *ket* side is closed, therefore does not have any excitations and constitutes the reference, $|0\rangle$.

The diagrams are transformed into equations according to the following rules, valid for spatial orbitals: [12]

1. Hole lines (h) correspond to occupied ($j, j, k, ...$) and particle lines (p) to virtual ($a, b, c, ...$) spatial orbitals.

2. Internal lines, *i.e.*, lines connecting two vertices, are summed up.

3. Each vertex contributes an integral or an amplitude:

   - Fock operator: $F_{bc} = \langle b|\hat{F}|c\rangle = \langle \text{ out } | \hat{F} | \text{ in } \rangle$;
   - Singles and Doubles amplitudes: c_a^i and c_{ab}^{ij};
   - Fluctuation operator: (left-out left-in $|\hat{V}|$ right-out right-in), where the chemical (Mullikan) notation for two-electron integrals was used and the outgoing lines correspond to complex conjugated indices;

e.g.

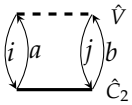

leads to

$$\sum_{iajb} c_{ab}^{ij}(ia|jb) = \sum_{iajb} c_{ab}^{ij} \int \phi_i^*(\mathbf{r}_1)\phi_a(\mathbf{r}_1)\frac{1}{|\mathbf{r}_1 - \mathbf{r}_2|}\phi_j^*(\mathbf{r}_2)\phi_b(\mathbf{r}_2)d\mathbf{r}_1 d\mathbf{r}_2.$$

4. The sign of a term is given by $(-1)^{h+L}$, with h and L denoting the number of hole lines and number of loops in the diagram, respectively; a pair of external hole and particles lines, originating on one single vertex, are also considered as a loop (external loop).

5. An internal loop yields a factor of 2.

6. Equivalent vertices yield a factor of 1/2; equivalent vertices are vertices on an operator, which are connected to vertices of another operator in the same way, *e.g.*

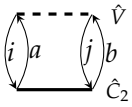

$$+2 * 2 * \frac{1}{2} \sum_{iajb} c_{ab}^{ij}(ia|jb).$$

7. An external particle line generates an overlap matrix between virtual orbitals, if originating from a vertex of an amplitude.

In contrary to the spin-orbital formalism [11], external lines are not equivalent.

1.1.3 Diagrams for CIS

Following those rules, the left hand side of Eq. (1.7),

$$\langle \Phi_i^a | \hat{H} \hat{C}_1 | 0 \rangle, \tag{1.8}$$

consequently leads for the singlet state to the following diagrams,

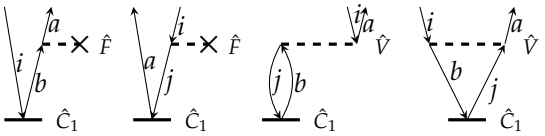

$$+ \sum_b F_{ab} c_b^i - \sum_{jb} S_{ab} c_b^j F_{ji} + 2 \sum_{jb} (ai|jb) c_b^j - \sum_{jb} (ji|ab) c_b^j,$$

where non-orthogonal virtual orbitals are assumed (*vide infra* Sec. 1.1.5). The CIS working equations (Eq. (1.7)) can be reformulated as

$$\sum_b F_{ab} c_b^i - \sum_{jb} S_{ab} c_b^j F_{ji} + 2 \sum_{jb} (ai|jb) c_b^j - \sum_{jb} (ji|ab) c_b^j = \omega_{\mathrm{CIS}} c_a^i, \tag{1.9}$$

or in the physicists notation for two-electron integrals as

$$\sum_b F_{ab} c_b^i - \sum_{jb} S_{ab} c_b^j F_{ji} + 2 \sum_{jb} [aj|ib] c_b^j - \sum_{jb} [ja|ib] c_b^j = \omega_{\mathrm{CIS}} c_a^i. \tag{1.10}$$

For the triplet state the third term vanishes because of spin orthogonality. Eq. (1.9) can be rewritten using a matrix notation with separated Fock and two-electron parts as

$$\mathbf{Hc} = \mathbf{Fc} + \mathbf{Vc} = \omega_{\mathrm{CIS}} \mathbf{c}. \tag{1.11}$$

A computational bottleneck are the four-index electron repulsion integrals (ERIs), which can be approximated utilizing the density fitting technique.

1.1.4 Density fitting approximation

In the density fitting framework, four-index electron repulsion integrals as appearing in Eq. (1.9),

$$\begin{aligned} (pq|rs) &= \int \mathrm{d}\mathbf{r}_1 \mathrm{d}\mathbf{r}_2 \phi_p^*(\mathbf{r}_1) \phi_q(\mathbf{r}_1) r_{12}^{-1} \phi_r^*(\mathbf{r}_2) \phi_s(\mathbf{r}_2) \\ &= \int \mathrm{d}\mathbf{r}_1 \mathrm{d}\mathbf{r}_2 \rho_{pq}(\mathbf{r}_1) r_{12}^{-1} \rho_{rs}(\mathbf{r}_2), \end{aligned} \tag{1.12}$$

are approximated by a sum of product of two three-index quantities. This is achieved by substituting the orbital product density ρ_{pq} by an approximated one, $\tilde{\rho}_{pq}$, to be expanded in an auxiliary basis set $\{\chi_P\}$,

$$\rho_{pq}(\mathbf{r}) \approx \tilde{\rho}_{pq}(\mathbf{r}) = \sum_P d_P^{pq} \chi_P(\mathbf{r}). \tag{1.13}$$

The fitting coefficients d_P^{pq} are usually determined by minimizing the error functional,

$$\begin{aligned} f(d_P^{pq}) &= \int \mathrm{d}\mathbf{r}_1 \mathrm{d}\mathbf{r}_2 \Big(\rho_{pq}(\mathbf{r}_1) - \tilde{\rho}_{pq}(\mathbf{r}_1)\Big) r_{12}^{-1} \Big(\rho_{pq}(\mathbf{r}_2) - \tilde{\rho}_{pq}(\mathbf{r}_2)\Big) \\ &= (pq|pq) - 2\sum_P d_P^{pq}(P|\rho_{pq}) + \sum_{PQ} d_P^{pq}(P|Q) d_Q^{pq}, \end{aligned} \tag{1.14}$$

with respect to d_P^{pq}, leading to a system of linear equations,

$$\begin{aligned} &\frac{\partial f(d_P^{pq})}{\partial d_R^{pq}} \stackrel{!}{=} 0 \\ &\quad = \frac{\partial}{\partial d_R^{pq}} \Big((\rho_{pq}|\rho_{pq}) - 2\sum_P d_P^{pq}(P|\rho_{pq}) + \sum_{PQ} d_P^{pq}(P|Q) d_Q^{pq} \Big) \\ &\quad \Rightarrow 0 = -2(R|\rho_{pq}) + 2\sum_P d_P^{pq}(P|R) \\ &\quad \Longleftrightarrow (R|\rho_{pq}) = \sum_P d_P^{pq}(P|R). \end{aligned} \tag{1.15}$$

Solving Eq. (1.15) for the fitting coefficients provides

$$d_P^{pq} = \sum_Q (P|Q)^{-1} (Q|\rho_{pq}). \tag{1.16}$$

To guarantee an error in the integrals of second order with respect to the fitting error in the densities, the robust formula proposed by Dunlap [8] should be used to express the integral $(pq|rs)$,

$$\begin{aligned} (pq|rs) &\approx (\tilde{\rho}_{pq}|\rho_{rs}) + (\rho_{pq}|\tilde{\rho}_{rs}) - (\tilde{\rho}_{pq}|\tilde{\rho}_{rs}) \\ &= \sum_P d_P^{pq}(P|\rho_{rs}) + \sum_P (\rho_{pq}|P) d_P^{rs} - \sum_{PQ} d_P^{pq}(P|Q) d_Q^{rs}. \end{aligned} \tag{1.17}$$

In the case of an identical fitting basis for all product densities this formula simplifies to

$$(pq|rs) \approx \sum_{PQ} (\rho_{pq}|Q)(Q|P)^{-1}(P|\rho_{rs}). \tag{1.18}$$

It is important to mention that the density fitting approximation does not improve the overall scaling with molecular size N, if the four-index integrals are assembled. There it only allows for better weighted and balanced storage of integrals and coefficients [13,14], which improves the performance, *e.g.* in the MP2 method, by an order of magnitude, and for crystals even more [6,15,16]. If the assembly of four-index integrals Eqs. (1.17) or (1.18) can be avoided, as in the CIS theory, also the scaling is improved by one order: $O(N^5)$ to $O(N^4)$ (*vide infra* Chapter 2.2.5).

The fitting basis set usually consists of GTOs centered on atoms. Alternatively, one can use another fitting basis set, which allows for a remarkable simplification of 3- and 2-index integrals in Eqs. (1.17) and (1.16). Since those functions are closely related to the Poisson equation, they are called the Poisson-type orbitals (PTOs). Considering a set of GTOs $\{g_Q(\mathbf{r})\}$, the corresponding PTO set, $\{p_Q(\mathbf{r})\}$ is defined the following way [17,18]:

$$p_Q(\mathbf{r}) = -\frac{1}{4\pi}\nabla^2 g_Q(\mathbf{r})\,. \tag{1.19}$$

Exploiting the identity (a form of the Poisson equation), [18]

$$\int \mathrm{d}\mathbf{r}' \frac{\nabla^2 g(\mathbf{r}')}{|\mathbf{r}-\mathbf{r}'|} = -4\pi g(\mathbf{r}), \tag{1.20}$$

the bra-vectors of type $p_Q(\mathbf{r})$ reduce to

$$(Q| = g_Q(\mathbf{r}). \tag{1.21}$$

A Coulomb integral (two-electron integral) involving the function p_Q reduces then to an one-electron integral with the function g_Q. This simplifies not only the integral evaluation, but also leads to entirely different decay properties of the integrals. The qualitative change in the decay rate constitutes the key to the convergence of the lattice sums, because the PTOs

do not hold multipole moments of any order. [19] Therefore the PTO basis set has to be complemented with a few multipole-holding functions. In our case those are GTOs, where one GTO for each angular momentum and center turns out to be enough to fit the actual multipole moments of the densities [19, 20].

1.1.5 Local space

The use of canonical orbitals for spanning the occupied and virtual space has many disadvantages. They are delocalized, which leads to a bad scaling behaviour and at the same time they do not allow to exploit the short-range nature of the dynamic correlation in nonmetallic systems (the latter means that the steep scaling of correlation methods is an artefact of a badly chosen space and has no physical reason). The use of spatially localized orbitals solves those issues. The occupied orbital space can be spanned by mutually orthogonal localized molecular orbitals (LMOs), generated from canonical occupied orbitals by unitary transformation $\mathbf{W}$,

$$|\phi_i\rangle = \sum_{\tilde{i}}^{n_{occ}} |\phi_{\tilde{i}}^{\text{can}}\rangle W_{\tilde{i}i} = \sum_{\mu}^{N_{AO}} |\chi_\mu\rangle L_{\mu i}. \tag{1.22}$$

Because of the diffuse character of virtual orbitals their localization is problematic. The basis functions for the virtual space are therefore constructed by projecting AOs onto the virtual space (projected AOs, PAOs):

$$|\phi_a\rangle = \left(1 - \sum_{i}^{n_{occ}} |\phi_i\rangle\langle\phi_i|\right)|\chi_a\rangle = \sum_{\mu}^{N_{AO}} |\chi_\mu\rangle P_{\mu a}, \tag{1.23}$$

with the projector matrix

$$\mathbf{P} = \mathbf{1} - \mathbf{L}\mathbf{L}^{\dagger}\mathbf{S}^{\mathbf{AO}}, \tag{1.24}$$

where $\mathbf{S}^{\mathbf{AO}}$ denotes the overlap matrix between AOs. Since AOs are not orthogonal, the PAOs are not mutually orthogonal either, but they are orthogonal to the LMOs by construction due to the projection (strong

orthogonality). Furthermore, they are, like AOs, assigned to a particular atom. Besides, since the number of virtual orbitals is smaller than that of AOs, PAOs form a redundant set of functions spanning a basis for the virtual space.

In molecules, the matrix **W** is usually constructed using well defined localization criterions as introduced by Boys [21] or Pipek-Mezey [22]. The former minimizes their spatial spread, while the latter minimizes the net number of atoms contributing to a LMO. The construction of well-localized occupied orbitals in periodic systems - Wannier functions (WFs) - is of more delicate matter than in molecules [23, 24]. The procedure utilized in this thesis uses two mutually dependent steps [23]. The first maximizes the separation of the centers of the WFs within the unit cell. The second reduces the number of supporting atoms by zeroing the support from atomic orbitals corresponding to atoms, whose population by the given WF drops below a certain threshold. The resulting "tail-cutted" WFs are projected against the occupied space and normalized. These two steps are repeated until the degree of localization remains unimproved. Since this procedure does not involve a well-defined localization functional, issues might appear in local techniques based on energy Lagrangian [25, 26], but are of no consequence in the present context.

1.2 Periodic systems

1.2.1 Excited state CIS theory

Bloch's theorem states that a Bravais lattice translation $\hat{T}_{\mathbf{R}}$ affects the excitonic wavefunction $\Psi_{\text{exc}}(\mathbf{k}_{\text{exc}})$ of the periodic Hamiltonian as follows:

$$\hat{T}_{\mathbf{R}}\Psi_{\text{exc}}(\mathbf{k}_{\text{exc}}) = \exp(\imath\mathbf{k}_{\text{exc}}\mathbf{R})\Psi_{\text{exc}}(\mathbf{k}_{\text{exc}}), \tag{1.25}$$

where $\exp(\imath\mathbf{k}_{\text{exc}}\mathbf{R})$ is a plane wave with periodicity $\mathbf{k}_{\text{exc}}$. In the case of CIS, the excitonic wavefunction is expanded in $\mathbf{k}_{\text{exc}}$-symmetry-adapted linear

combinations of singly excited determinants (*cf.* Sec. 1.1.1),

$$\Psi_{\text{exc}}(\mathbf{k}_{\text{exc}}) = \sum_{i\mathcal{I}a\mathcal{A}} c_{a\mathcal{A}}^{i\mathcal{I}}(\mathbf{k}_{\text{exc}})|\Phi_{i\mathcal{I}}^{a\mathcal{A}}\rangle, \tag{1.26}$$

where the calligraphic indices $\mathcal{I}$ and $\mathcal{A}$ denote the unit cells, where the functions i and a are centered, respectively.

From Eqs. (1.25) and (1.26) follows that only coefficients with the occupied index restricted to the reference cell are needed to be calculated,

$$c_{a\mathcal{A}}^{i\mathcal{I}}(\mathbf{k}_{\text{exc}}) = c_{a(\mathcal{A}\ominus\mathcal{I})}^{i}(\mathbf{k}_{\text{exc}}) \exp(-\imath\mathbf{k}_{\text{exc}}\mathbf{R}_{\mathcal{I}}), \tag{1.27}$$

and all other coefficients can be obtained by multiplying it with a phase factor $\exp(-\imath\mathbf{k}_{\text{exc}}\mathbf{R}_{\mathcal{I}})$.

The excitonic CIS wavefunction then can be rewritten as

$$\Psi_{\text{exc}}(\mathbf{k}_{\text{exc}}) = \sum_{\mathcal{I}} \exp(-\imath\mathbf{k}_{\text{exc}}\mathbf{R}_{\mathcal{I}}) \sum_{ia\mathcal{A}} c_{a(\mathcal{A}\ominus\mathcal{I})}^{i}(\mathbf{k}_{\text{exc}})|\Phi_{i\mathcal{I}}^{a\mathcal{A}}\rangle. \tag{1.28}$$

1.2.2 Γ-point excitations

In reciprocal space the CIS coefficients can be defined as the Fourier transforms of direct space coefficients as

$$\begin{aligned} c_{a\mathbf{k}_a}^{i\mathbf{k}}(\mathbf{k}_{\text{exc}}) \equiv \frac{1}{\sqrt{n_{\mathcal{A}}}} \frac{1}{\sqrt{n_{\mathcal{I}}}} \sum_{\mathcal{A}} \exp(-\imath\mathbf{k}_a\mathbf{R}_{\mathcal{A}}) \\ \times \sum_{\mathcal{I}} \exp(\imath\mathbf{k}_i\mathbf{R}_{\mathcal{I}}) c_{a\mathcal{A}}^{i\mathcal{I}}(\mathbf{k}_{\text{exc}}), \end{aligned} \tag{1.29}$$

where $\mathbf{k}_i$ and $\mathbf{k}_a$ are the translational symmetry indices of functions i and a, respectively, and $n_{\mathcal{I}}$ and $n_{\mathcal{A}}$ denote the number of unit cells in which the corresponding functions are centered. The minus sign in the Fourier transform of $\mathcal{I}$ originates from the complex conjugation of the i index in Eq. (1.9) or Eq. (1.10), while the a index is not complex conjugated (further explanations *cf.* Sec. 2.2.4).

Applying translational symmetry to the direct space CIS coefficients, as obtained in Eq. (1.27), and changing the order of the infinite summation

over lattice indices from $\mathcal{I}$ to $\mathcal{A}' \equiv \mathcal{A} \ominus \mathcal{I}$,

$$c_{a\mathbf{k}_a}^{i\mathbf{k}_i}(\mathbf{k}_{\text{exc}}) = \frac{1}{\sqrt{n_{\mathcal{A}}}} \frac{1}{\sqrt{n_{\mathcal{I}}}} \sum_{\mathcal{A}'} c_{a\mathcal{A}'}^{i}(\mathbf{k}_{\text{exc}}) \exp(\imath(\mathbf{k}_{\text{exc}} - \mathbf{k}_i)\mathbf{R}_{\mathcal{A}'}) \times \underbrace{\sum_{\mathcal{A}} \exp(-\imath(\mathbf{k}_{\text{exc}} + \mathbf{k}_a - \mathbf{k}_i)\mathbf{R}_{\mathcal{A}})}_{n_{\mathcal{A}}\delta_{\mathbf{k}_{\text{exc}},\mathbf{k}_a-\mathbf{k}_i}}, \tag{1.30}$$

leads, due to the second orthogonality relation for irreducible representations of the translational group ($\mathbf{k}_{\text{exc}} + \mathbf{k}_a - \mathbf{k}_i = 0$) [27], to the translational symmetry relations for the reciprocal space excitations:

$$\mathbf{k}_{\text{exc}} = \mathbf{k}_a - \mathbf{k}_i. \tag{1.31}$$

Consequently, not all excitations in reciprocal space are compatible with the corresponding symmetry of the exciton $\mathbf{k}_{\text{exc}}$.

When considering only vertical excitations, *i.e.*, excitations from occupied orbitals to virtual orbitals belonging to the same $\mathbf{k}$-point, $\mathbf{k}_a = \mathbf{k}_i$, the symmetry of the exciton according Eq. (1.31), corresponds to the Γ-point, $\mathbf{k}_{\text{exc}} = 0$, and can be expressed as

$$c_{a\mathbf{k}_a}^{i\mathbf{k}_i} = \begin{cases} c_a^i(\mathbf{k}) & \text{if } \mathbf{k}_i = \mathbf{k}_a = \mathbf{k}, \\ 0 & \text{otherwise.} \end{cases} \tag{1.32}$$

The direct space CIS coefficients Eq. (1.27) then become translational invariant and the index $\mathbf{k}_{\text{exc}}$ can be omitted (*cf.* Sec. 2.2.1):

$$c_{a\mathcal{A}}^{i\mathcal{I}} = c_{a(\mathcal{A}\ominus\mathcal{I})}^{i}. \tag{1.33}$$

The CIS coefficients are computed utilizing the Davidson technique [10].

1.2.3 Davidson diagonalization

In 1975, Ernest R. Davidson proposed an inexpensive technique to calculate several of the lowest (or higher) eigenvalues and corresponding eigenvectors of large Hermitian matrices [10]. The method implies diagonalization

of the matrix projected to a smaller subspace, which is iteratively adjusted to contain the eigenvectors of the needed eigenvalues.

A smaller space Hamilton matrix $\mathbf{h}$ (to be referred as "small $\mathbf{h}$-matrix") in the n-th iteration can be written as (*cf.* left hand side of Eq. (1.9)),

$$\begin{aligned} h_{rs}^{(n)} &= \Delta\mathbf{c}^{\dagger(r)}\mathbf{H}\Delta\mathbf{c}^{(s)} \\ &= \Delta\mathbf{c}^{\dagger(r)}(\mathbf{H}\Delta\mathbf{c})^{(s)}, \end{aligned} \tag{1.34}$$

where the CIS trial vectors are denoted by $\Delta\mathbf{c}$, and the upperscript indices count the iterations n ($r, s = 0, 1, \ldots, n-1$). The first vector $\Delta\mathbf{c}^{(0)}$ is obtained from an initial guess (for a discussion on different ways to generate an initial guess for CIS, *vide infra* Sec. 2.3.5). The elements of the eigenvectors $\boldsymbol{\sigma}$ of the small $\mathbf{h}$-matrix,

$$\mathbf{h}^{(n)}\boldsymbol{\sigma}^{(n)} = \omega_{\mathrm{CIS}}^{(n)}\boldsymbol{\sigma}^{(n)}, \tag{1.35}$$

are then used as coefficients for a linear combination of the CIS vectors $\Delta\mathbf{c}$, *i.e*, the small space vector $\boldsymbol{\sigma}$ is projected onto the full space $\Delta\mathbf{c}$,

$$\mathbf{c}^{(n)} = \sum_{r=1}^{n} \sigma_r^{(n)}\Delta\mathbf{c}^{(r)}, \tag{1.36}$$

The vector $\mathbf{c}^{(n)}$ and the CIS energy $\omega_{\mathrm{CIS}}^{(n)}$ can be plugged into the full eigenvalue problem,

$$(\mathbf{Hc})^{(n)} \begin{cases} \neq \omega_{\mathrm{CIS}}^{(n)}\mathbf{c}^{(n)} \text{ if not converged,} \\ \approx \omega_{\mathrm{CIS}}^{(n)}\mathbf{c}^{(n)} \text{ if converged.} \end{cases} \tag{1.37}$$

The residual vector thus reads

$$\begin{aligned} \mathbf{r}^{(n)} &= (\mathbf{Hc})^{(n)} - \omega_{\mathrm{CIS}}^{(n)}\mathbf{c}^{(n)} \\ &= \sum_{r=1}^{n} \sigma_r^{(n)}\Big((\mathbf{H}\Delta\mathbf{c})^{(r)} - \omega_{\mathrm{CIS}}^{(n)}\Delta\mathbf{c}^{(r)}\Big), \end{aligned} \tag{1.38}$$

where Eq. (1.36) was used. If the norm of the residual vector,

$$\left\|\mathbf{r}^{(n)}\right\| = \sum_{\bar{i}\bar{a}\mathbf{k}} \left|r_{\bar{i}\bar{a}}^{\bar{i}}(\mathbf{k})\right|^2, \tag{1.39}$$

is smaller than a predefined threshold, the Davidson procedure is assumed to be converged. If so, the N dimensional eigenvalue problem is well described within n dimensions for the lowest eigenvalue and eigenvector.

A next iteration basis vector for the smaller space is constructed in the framework of the first-order perturbation theory. Consider the $(n+1)$th eigenvalue problem

$$\mathbf{H}\Big(\mathbf{c}^{(n)} + \Delta\mathbf{c}^{(n)}\Big) = \omega_{\mathrm{CIS}}^{(n)}\Big(\mathbf{c}^{(n)} + \Delta\mathbf{c}^{(n)}\Big) \tag{1.40}$$

or

$$(\mathbf{H}\Delta\mathbf{c})^{(n)} - \omega_{\mathrm{CIS}}^{(n)}\Delta\mathbf{c}^{(n)} = -\Big((\mathbf{H}\mathbf{c})^{(n)} - \omega_{\mathrm{CIS}}^{(n)}\mathbf{c}^{(n)}\Big), \tag{1.41}$$

where $\Delta\mathbf{c}^{(n)}$ is considered as a first order correction to zeroth order $\mathbf{c}^{(n)}$.

The matrix $\mathbf{H}$ can be splitted into a zeroth and first order part by means of Møller-Pleset perturbation theory,

$$\mathbf{H} = \underbrace{\mathbf{F}}_{\text{0th order}} + \underbrace{\mathbf{V}}_{\text{1st order}}, \tag{1.42}$$

and the matrix-vector product on the left-hand side of Eq. (1.41) can be treated at first order,

$$(\mathbf{H}\Delta\mathbf{c})^{(n)} \approx (\mathbf{F}\Delta\mathbf{c})^{(n)}. \tag{1.43}$$

Now, exploiting the diagonality of the Fock matrix in the canonical space, the update for the new trial vector takes the following form:

$$\begin{aligned}(\Delta\mathbf{c}^{(n)})_{\bar{a}}^{\bar{i}}(\mathbf{k}) &= -\frac{(\mathbf{H}\mathbf{c}^{(n)})_{\bar{a}}^{\bar{i}}(\mathbf{k}) - \omega_{\mathrm{CIS}}^{(n)}(\mathbf{c}^{(n)})_{\bar{a}}^{\bar{i}}(\mathbf{k})}{\varepsilon_{\bar{a}}(\mathbf{k}) - \varepsilon_{\bar{i}}(\mathbf{k}) - \omega_{\mathrm{CIS}}^{(n)}} \\ &= -\frac{(\mathbf{r}^{(n)})_{\bar{a}}^{\bar{i}}(\mathbf{k})}{\varepsilon_{\bar{a}}(\mathbf{k}) - \varepsilon_{\bar{i}}(\mathbf{k}) - \omega_{\mathrm{CIS}}^{(n)}}.\end{aligned} \tag{1.44}$$

Here, the labels $\bar{i}$ and $\bar{a}$ denote occupied and virtual canonical orbitals, respectively, and the single symmetry index $\mathbf{k}$ is a translational symmetry

vector, fulfilling the symmetry requirements for Γ-point excitons (*cf*. Eq. (1.32)).

The update $(\Delta\mathbf{c}^n)^{\bar{i}}_{\bar{a}}(\mathbf{k})$ is orthogonalized to the trial vectors of the previous iterations and normalized.

1.3 Structure of the thesis

This thesis is organized as follows. In the next chapter theory and implementation of a local configuration interaction singles (CIS) method using the density fitting approximation for polymers is presented and applied to several prototypical test-systems. Chapter 3 describes the techniques allowing for generalization of the method to 2D and 3D systems. Besides, the effect of the choice of the atomic orbital basis sets on the CIS excitation energy is investigated in Chapter 4. Chapter 5 summarizes the results of this thesis.

Chapter 2

Periodic DF local CIS method for polymers

2.1 Introduction

Quantum chemistry offers a wide range of ab initio techniques of increasing accuracy and cost for calculating the electronic structure of both ground and excited states of molecules. The lowest ranking in the hierarchy occupy the relatively inexpensive, and at the same time not very accurate Hartree-Fock (HF) (for the ground state) and configuration interaction singles (CIS) (for the excited states) methods. Among the highly accurate, but at the same time still feasible, at least for not very extended systems, methods one can mention the CCSD(T) and MRCI – "golden standards" for the single-reference ground state and multi-reference ground and excited state calculations, correspondingly. As a reasonable compromise between the accuracy and cost of the calculations one usually considers second order methods like MP2 for the ground state and CC response, [28] ADC(2), [29] CIS(D) [30] or CASPT2 [31] for the excited state, which can be applied to rather extended systems, especially when combined with local schemes [32, 33].

For periodic systems, quantum chemical treatments are much more complicated and costly. As a consequence, the density functional theory (DFT) is the most common technique used for ground state periodic calculations. Recently, the MP2 method has been generalized to the 3D periodic case within the Laplace-transform [34], local [16] and canonical plane wave [35] formulations. However, so far most of the quantum chemical approaches to the ground state of periodic systems are based on finite cluster models. [36–38] For excited states, the finite cluster approach [39] is more problematic, making periodic schemes preferable. Most of these methods use the Green's function formalism [40–46], including MP2-based quasi-orbital approaches. [34,47–50] Periodic CIS and time dependent HF (TD-HF) methods and their DFT counterparts (TDA, TD-DFT) have been formulated [51] and implemented for 1D periodic systems [47,51–55]. The periodic CIS treatment has been complemented with schemes, allowing for a low level inclusion of the correlation effects. [47,48] The most elaborate scheme within the theoretical description of excited states in periodic systems presently is EOM-CC theory with periodic boundary conditions which was applied to polyethylene. [56] This method turned out to be computationally extremely costly, but at the same time provided accurate results. As an example of an early calculation of excitonic effects in a 3D solid one can mention a TD-HF method, employing approximate Wannier functions of the valence and lowest conduction bands, which has been applied to diamond. [57] Nowadays, the excitonic states are usually studied by solving the Bethe-Salpeter equation, for quasi-particles obtained within DFT/GW approach. [42,43,58–62] This method is quite expensive, but delivers accurate excitation energies. Formally, it reduces to a TD-HF- or CIS-like equation but with a screened rather than the bare Coulomb kernel.

Despite the existence of a number of periodic excited state methods the Kohn-Sham (more rarely HF) HOCO-LUCO (highest occupied and lowest unoccupied crystalline orbital) difference still remains the most popular

estimate for the excitation energies in periodic systems. The TD-DFT method, which has proven to be quite successful in molecular studies, is not as useful in the periodic case. In fact, the intrinsic problem of the standard DFT — the self interaction error, which causes a substantial underestimation of charge transfer state energies by TD-DFT, can lead to extreme consequences in infinite systems. As was shown in Refs. 52 and 63, the lowest excitation energy of semi-local TD-DFT in a crystal is equal to the ordinary DFT HOCO-LUCO difference [63]. This fact questions both the usefulness and adequacy of the TD-DFT approach in the periodic context. Indeed, since the TD-DFT result can be obtained with much smaller effort by performing a simple DFT calculation, it, at least for the lowest excited state, implicitly ignores the electron-hole attraction, essential for the correct description of an exciton.

This work is the first step towards the development of a hierarchy of quantum chemical excited state methods for periodic systems. Such methods would be a valuable complement to the existing Green's function based approaches for periodic systems (*vide supra*). In this paper we describe a local CIS method applicable to polymers. This method is the lowest in the hierarchy and is not expected to provide high accuracy, since electron correlation effects are not included. At the same time, it captures the excitonic nature of the excited state and can be a good starting point for more elaborate and accurate correlated treatment, which is planned to be implemented at a later stage.

Our formalism is based on Gaussian-type-orbital (GTO) basis set and localized orbitals both for occupied and virtual states. The local representation allows for significant computational savings compared to the canonical one for strongly and intermediately bound excitons and fits into the intuitive picture of a localized hole interacting with a localized electron. The attractive feature of the local description of excitons has been noticed very early, so that Wannier functions (WFs) – localized orbitals in periodic systems – were introduced for the first time in the conjunction with

this particular problem [64]. However this approach remained illustrative, rather than practical due to the difficulty in obtaining well localized virtual functions. In the current work we apply the technique, adopted in the local correlation methods for the ground state [65,66] where the virtual space is spanned by mutually non-orthogonal, and even partially redundant, but well localized projected atomic orbitals (PAOs).

The paper is organized as follows. In Section 2.2 we present the general formalism of the periodic local CIS method. The details of the implementation are given in Section 2.3. The results of the test calculations and their analysis are reported in Section 2.4. Section 2.5 concludes the paper.

Throughout the paper we use the following convention: the indices $(i, j, ...)$ and $(a, b, ...)$ denote Wannier functions and projected atomic orbitals, respectively, or their Fourier images. The indices $(\bar{i}, \bar{j}, ...)$ and $(\bar{a}, \bar{b}, ...)$ label the canonical occupied and virtual orbitals. $(P, Q, ...)$ represent auxiliary fitting functions and $(\mu, \nu, ...)$ atomic orbitals (AOs). The calligraphic indices $(\mathcal{I}, \mathcal{J}, ...)$, $(\mathcal{A}, \mathcal{B}, ...)$, $(\mathcal{P}, \mathcal{Q}, ...)$ and $(\mathcal{M}, \mathcal{N}, ...)$ identify the lattice vectors to the cells, where the functions $(i, j, ...)$, $(a, b...)$, $(P, Q, ...)$ and $(\mu, \nu, ...)$ are centered. The vectors $(\mathbf{k}_i, \mathbf{k}_j, ...)$, $(\mathbf{k}_a, \mathbf{k}_b, ...)$ and $(\mathbf{k}_P, \mathbf{k}_Q, ...)$ indicate the wave-vectors from the first Brillouin zone corresponding to the occupied, virtual, or auxiliary functions (to be referred to in the following as **k**-vectors or **k**-points). With the term **k**-mesh or **k**-net we will designate the actual sets of the **k**-points used in the calculations. The chemical (Mulliken) notation is employed for the two-electron integrals.

2.2 Periodic local CIS method

2.2.1 The excitonic CIS wavefunction

The CIS wavefunction $|\Psi_{\text{exc}}(\mathbf{k}_{\text{exc}})\rangle$ for an exciton with the translational symmetry $\mathbf{k}_{\text{exc}}$ is defined as

$$|\Psi_{\text{exc}}(\mathbf{k}_{\text{exc}})\rangle = \hat{C}_1(\mathbf{k}_{\text{exc}})|0\rangle, \tag{2.1}$$

where $|0\rangle$ is the Hartree-Fock determinant and $\hat{C}_1(\mathbf{k}_{\text{exc}})$ is a linear combination of single excitation operators. It can be considered in the local basis, defined in the direct space, as

$$\hat{C}_1(\mathbf{k}_{\text{exc}}) = \sum_{i\mathcal{I}a\mathcal{A}} c_{a\mathcal{A}}^{i\mathcal{I}}(\mathbf{k}_{\text{exc}})\hat{\tau}_{i\mathcal{I}}^{a\mathcal{A}}, \tag{2.2}$$

where $\hat{\tau}_{i\mathcal{I}}^{a\mathcal{A}}$ is an excitation operator in second quantization, which excites an electron from the local occupied orbital (Wannier function) i located in the $\mathcal{I}$-cell into a projected atomic orbital a located in the $\mathcal{A}$-cell, and $c_{a\mathcal{A}}^{i\mathcal{I}}(\mathbf{k}_{\text{exc}})$ are the corresponding amplitudes.
The wavefunction can be alternatively and equivalently written in the canonical basis:

$$\hat{C}_1(\mathbf{k}_{\text{exc}}) = \sum_{\bar{i}\mathbf{k}_i\bar{a}\mathbf{k}_a} c_{\bar{a}\mathbf{k}_a}^{\bar{i}\mathbf{k}_i}(\mathbf{k}_{\text{exc}})\hat{\tau}_{\bar{i}\mathbf{k}_i}^{\bar{a}\mathbf{k}_a}, \tag{2.3}$$

where $\hat{\tau}_{\bar{i}\mathbf{k}_i}^{\bar{a}\mathbf{k}_a}$, which excites an electron from the occupied Bloch orbital $\bar{i}$ with translational symmetry $\mathbf{k}_i$ into the virtual Bloch orbital $\bar{a}$ with translational symmetry $\mathbf{k}_a$, is weighted with the corresponding amplitude $c_{\bar{a}\mathbf{k}_a}^{\bar{i}\mathbf{k}_i}(\mathbf{k}_{\text{exc}})$.

The Bloch theorem states, that for a Γ-point exciton, *i.e.* $\mathbf{k}_{\text{exc}} = 0$, a Bravais lattice translation $\hat{T}_{\mathbf{R}}$ does not affect the wavefunction:

$$\hat{T}_{\mathbf{R}}|\Psi_{\text{exc}}(\mathbf{k}_{\text{exc}} = 0)\rangle = \hat{T}_{\mathbf{R}}|\Psi_{\text{exc}}^{\Gamma}\rangle = |\Psi_{\text{exc}}^{\Gamma}\rangle. \tag{2.4}$$

In the following we focus on the excitons of this particular symmetry and therefore omit for brevity the index $\mathbf{k}_{\text{exc}}$.
From Eqs. (2.2) and (2.4) it follows that the CIS amplitudes in the local representation possess the translational invariance:

$$c_{a\mathcal{A}}^{i\mathcal{I}} = c_{a(\mathcal{A}\ominus\mathcal{I})}^{i}. \tag{2.5}$$

This means, that only the amplitudes, where, *e.g.* the occupied index is restricted to the reference cell, are symmetry unique and therefore need to be calculated.
The CIS amplitudes for the Γ-point excitons in canonical representation

(and generally in the **k**-space representation), also have a symmetry restriction:

$$c^{\bar{i}\mathbf{k}_i}_{\bar{a}\mathbf{k}_a} = \begin{cases} c^{\bar{i}}_{\bar{a}}(\mathbf{k}) & \text{if } \mathbf{k}_i = \mathbf{k}_a = \mathbf{k}, \\ 0 & \text{otherwise.} \end{cases} \tag{2.6}$$

Thus, only the coefficients corresponding to vertical (in **k**-space sense) excitations are nonzero and just one Fourier transform between direct and reciprocal space has to be carried out for the amplitudes between direct and reciprocal space (*vide infra*). The corresponding excitation operator from Eqs. (2.2) and (2.3) then reduces to:

$$\hat{C}_1 = \sum_{ia\mathcal{A}} c^{i}_{a\mathcal{A}} \sum_{\mathcal{I}} \hat{\tau}^{a(\mathcal{A}+\mathcal{I})}_{i\mathcal{I}} = \sum_{\bar{i}\bar{a}\mathbf{k}} c^{\bar{i}}_{\bar{a}}(\mathbf{k}) \hat{\tau}^{\bar{a}}_{\bar{i}}(\mathbf{k}). \tag{2.7}$$

2.2.2 The CIS equations

Projecting the excitonic CIS Schrödinger equation (with a normal ordered Hamiltonian $\hat{H}_N$),

$$\hat{H}_N \hat{C}_1 |0\rangle = \omega_{\mathrm{CIS}} \hat{C}_1 |0\rangle, \tag{2.8}$$

onto singly excited determinants $\langle \Phi^{a\mathcal{A}}_{i}|$ or $\langle \Phi^{\bar{a}}_{\bar{i}}(\mathbf{k})|$ yields:

$$\begin{aligned} &\sum_{b\mathcal{B}} F_{a\mathcal{A}\, b\mathcal{B}} c^{i}_{b\mathcal{B}} - \sum_{j\mathcal{J}b\mathcal{B}} S^{\mathrm{PAO}}_{a\mathcal{A}\, b\mathcal{B}} c^{j\mathcal{J}}_{b\mathcal{B}} F_{j\mathcal{J}\, i} \\ &+ 2 \sum_{j\mathcal{J}b\mathcal{B}} (a\mathcal{A}\, i|j\mathcal{J}\, b\mathcal{B}) c^{j\mathcal{J}}_{b\mathcal{B}} - \sum_{j\mathcal{J}b\mathcal{B}} (j\mathcal{J}\, i|a\mathcal{A}\, b\mathcal{B}) c^{j\mathcal{J}}_{b\mathcal{B}} \\ &= \omega_{\mathrm{CIS}} c^{i}_{a\mathcal{A}} \end{aligned} \tag{2.9}$$

or

$$\begin{aligned} &\Big(\varepsilon_{\bar{a}}(\mathbf{k}) - \varepsilon_{\bar{i}}(\mathbf{k})\Big) c^{\bar{i}}_{\bar{a}}(\mathbf{k}) \\ &+ 2 \sum_{\bar{j}\bar{b}\mathbf{k}'} (\bar{a}\mathbf{k}\, \bar{i}\mathbf{k}|\bar{j}\mathbf{k}'\, \bar{b}\mathbf{k}') c^{\bar{j}}_{\bar{b}}(\mathbf{k}') - \sum_{\bar{j}\bar{b}\mathbf{k}'} (\bar{j}\mathbf{k}'\, \bar{i}\mathbf{k}|\bar{a}\mathbf{k}\, \bar{b}\mathbf{k}') c^{\bar{j}}_{\bar{b}}(\mathbf{k}') \\ &= \omega_{\mathrm{CIS}} c^{\bar{i}}_{\bar{a}}(\mathbf{k}) \end{aligned} \tag{2.10}$$

respectively. Here the Fock matrix is denoted by **F** and the orbital energies by ε. Since in the present formalism the virtual local orbitals are not orthogonal (*vide infra*) the corresponding overlap matrix $\mathbf{S}^{\mathrm{PAO}}$ appears. For the triplet state the first two-electron integral on the left hand side of (2.9) and (2.10) vanishes because of the orthogonality between the spin states.

On the one hand, the contraction with the Fock matrix becomes trivial in the canonical representation [Eq. (2.10)]. On the other hand, the evaluation of the two-electron part in the direct space and local representation, *i.e.*, according to Eq. (2.9), is preferable. Indeed, the locality of the orbitals allows for exploitation of the sparsity in the integrals and the CIS coefficients. Moreover, there is no need for a slowly convergent Fourier transform of the AO two-electron integrals into the reciprocal space, as in Ref. 52. And finally, efficient density fitting techniques for the two-electron integrals in the local representation, employed in the periodic local MP2 method [6, 16, 20, 67] can be applied to the CIS formalism (*vide infra*).

Separating thus the Fock matrix and two-electron parts and introducing the matrix notation one can write Eqs. (2.9) and (2.10) as:

$$\mathbf{Hc} = \mathbf{Fc} + \mathbf{Vc} = \omega_{\mathrm{CIS}}\mathbf{c}. \tag{2.11}$$

2.2.3 Davidson procedure

Equation (2.11) is the standard CI Hermitian eigenvalue problem, with the lowest eigenvalue corresponding to the optical band gap at the Γ-point. In order to calculate it we employ the Davidson diagonalization method. [10] This method represents a combination of an iterative updating of the eigenvector and a matrix diagonalization in the small subspace spanned by the approximate eigenvectors generated by the iterative procedure. Its convergence is much superior to a straight iterative method. A similar procedure was used by Roos and Siegbahn in their direct CI method. [68] The smaller space Hamilton matrix (to be referred to as "small **h**-matrix")

in the n-th iteration can be written as:

$$h_{rs}^{(n)} = \Delta\mathbf{c}^{\dagger(r)}(\mathbf{H}\Delta\mathbf{c})^{(s)}, \tag{2.12}$$

where the CIS trial vectors are denoted by $\Delta\mathbf{c}$, and the upper-script indices count the iterations ($r, s = 0, 1, ..., n-1$).

Exploiting the diagonality of the Fock matrix in the canonical basis, we evaluate the update or the new trial vector for the next iteration within first order perturbation theory in the Møller-Plesset partitioning as

$$(\Delta\mathbf{c}^{(n)})_{\bar{i}}^{\bar{a}}(\mathbf{k}) = -\frac{(\mathbf{H}\mathbf{c}^{(n)})_{\bar{i}}^{\bar{a}}(\mathbf{k}) - \omega_{\mathrm{CIS}}^{(n)}(\mathbf{c}^{(n)})_{\bar{i}}^{\bar{a}}(\mathbf{k})}{\varepsilon_{\bar{a}}(\mathbf{k}) - \varepsilon_{\bar{i}}(\mathbf{k}) - \omega_{\mathrm{CIS}}^{(n)}}. \tag{2.13}$$

Here, $\mathbf{c}^{(n)}$ denotes the vector in the full canonical space constructed from the eigenvector of the small $\mathbf{h}$-matrix, corresponding to its lowest eigenvalue $\omega_{\mathrm{CIS}}^{(n)}$. The new trial vector $\Delta\mathbf{c}^{(n)}$ is orthogonalized to the trial vectors of the previous iterations and normalized.

Once the trial vector for n-th iteration has been obtained, the Fock part $\mathbf{F}\Delta\mathbf{c}^{(n)}$ is directly calculated. Transformation of the trial vector to the direct space allows to evaluate the two-electron part $\mathbf{V}\Delta\mathbf{c}^{(n)}$, which then is subsequently transformed back to the canonical representation and added to the Fock part. Finally the small $\mathbf{h}$-matrix for the next iteration is constructed via (2.12) in the canonical basis. The particular choice of the local basis and the corresponding transformations, essential for the scheme are discussed in the next section.

2.2.4 Local representation

Definition of the local orbitals

As mentioned above the introduction of the local basis and the contraction of the CIS coefficients with the two electron integrals in the direct space is one of the key features of the present scheme. Although formally straight-forward, this scheme can be efficient in practice only when both

the occupied and virtual orbitals are well-localized, which is not trivial to achieve, especially for the virtual orbitals.

Construction of well-localized occupied orbitals in periodic systems – Wannier functions – is a more complicated matter than in molecules. However in the last two decades several efficient methods for their generation have been proposed [23, 24]. For the virtual states, the same localization schemes can formally be applied, but the spread of such orbitals remains relatively large. One of the reasons for the poor localization is the the mutual orthogonality constraint entering the formalism of most of the localization methods, and a greater number of virtual states compared to the occupied ones. In the present work we use mutually non-orthogonal PAOs, which have shown to be instrumental in local correlation methods for the ground state. [16, 66] In this case the virtual manifold is spanned by AOs projected onto the virtual space. The orbitals constructed in such a way are usually quite well localized, but at the same time non-orthogonal and moreover redundant. The latter property introduces some complications in the formalism, however, this is offset by the gain due to localization.

Wannier functions $|\phi_{i\mathcal{I}}^{\mathrm{WF}}\rangle$ can be written as linear combinations of canonical Bloch functions $|\phi_{\bar{i}}^{\mathrm{CAN}}(\mathbf{k})\rangle$:

$$|\phi_{i\mathcal{I}}^{\mathrm{WF}}\rangle = \frac{1}{\sqrt{n_{\mathbf{k}}}} \sum_{\mathbf{k}} \exp(-\imath \mathbf{k}\mathbf{R}_{\mathcal{I}}) \sum_{\bar{i}} W_{\bar{i}i}(\mathbf{k}) |\phi_{\bar{i}}^{\mathrm{CAN}}(\mathbf{k})\rangle. \tag{2.14}$$

Here, $n_{\mathbf{k}}$ is the number of the points in the $\mathbf{k}$-mesh chosen for the discrete Fourier transform. The WFs are localized using the transformation matrices $\mathbf{W}(\mathbf{k})$, which mix the states of the occupied bands. As in the Cryscor's periodic local MP2 approach, the Wannier functions are generated using the Crystal code [69] (*vide infra*). Mutual orthogonality of the WFs implies the unitarity of the matrices $\mathbf{W}(\mathbf{k})$:

$$\mathbf{W}^{-1}(\mathbf{k}) = \mathbf{W}^{\dagger}(\mathbf{k}). \tag{2.15}$$

For convenience we introduce now the so called quasi-Bloch functions

$$|\phi_{i}^{\mathrm{WF}}(\mathbf{k})\rangle = \sum_{\bar{i}} W_{\bar{i}i}(\mathbf{k}) |\phi_{\bar{i}}^{\mathrm{CAN}}(\mathbf{k})\rangle, \tag{2.16}$$

which due to the unitarity of the discrete Fourier transform are the Fourier images of the WFs:

$$|\phi_i^{\mathrm{WF}}(\mathbf{k})\rangle = \frac{1}{\sqrt{n_{\mathbf{k}}}} \sum_{\mathcal{I}} \exp(\imath \mathbf{k}\mathbf{R}_{\mathcal{I}}) |\phi_{i\mathcal{I}}^{\mathrm{WF}}\rangle. \tag{2.17}$$

The unitarity of the $\mathbf{W}(\mathbf{k})$ matrices [Eq. (2.15)] allows to trivially invert Eq. (2.16),

$$|\phi_{\bar{i}}^{\mathrm{CAN}}(\mathbf{k})\rangle = \sum_i W_{\bar{i}i}^{\dagger}(\mathbf{k}) |\phi_i^{\mathrm{WF}}(\mathbf{k})\rangle. \tag{2.18}$$

The PAOs are evaluated in a principally different way compared to WFs. Denoting the projector onto the HF occupied manifold as $\hat{P}$, and a μ-th atomic orbital centered in a $\mathcal{M}$-th cell as $\phi_{\mu\mathcal{M}}^{\mathrm{AO}}$ we define the PAOs as [65, 66]

$$|\phi_{a\mathcal{A}}^{\mathrm{PAO}}\rangle = (1 - \hat{P}) |\phi_{\mu\mathcal{M}}^{\mathrm{AO}}\rangle|_{a=\mu, \mathcal{A}=\mathcal{M}}. \tag{2.19}$$

By construction they span the virtual space, and are inherently local because of the locality of the AOs and of the projector $\hat{P}$. [70] At the same time, due to the non-orthogonality of the AOs, the PAOs remain non-orthogonal as well. Moreover, it is clear from Eq. (2.19) that the number of PAOs is equal to the number of AOs and thus larger than the number of the virtual orbitals, which means that the PAOs form a redundant set. It is convenient to use unnormalized PAOs, otherwise the symmetry properties of the underlying AOs are lost.

Since the canonical virtual orbitals and the PAOs span the same space, the latter can be expressed via the former as in Eq. (2.14),

$$|\phi_{a\mathcal{A}}^{\mathrm{PAO}}\rangle = \frac{1}{\sqrt{n_{\mathbf{k}}}} \sum_{\mathbf{k}} \exp(-\imath \mathbf{k}\mathbf{R}_{\mathcal{A}}) \sum_{\bar{a}} Q_{\bar{a}a}(\mathbf{k}) |\phi_{\bar{a}}^{\mathrm{CAN}}(\mathbf{k})\rangle, \tag{2.20}$$

and the Fourier images of the PAOs are obtained as:

$$|\phi_a^{\mathrm{PAO}}(\mathbf{k})\rangle = \sum_{\bar{a}} Q_{\bar{a}a}(\mathbf{k}) |\phi_{\bar{a}}^{\mathrm{CAN}}(\mathbf{k})\rangle. \tag{2.21}$$

The $\mathbf{Q}$ transformation is given by rectangular matrices $Q_{a\bar{a}}(\mathbf{k})$ with the property:

$$\mathbf{Q}^{\dagger}(\mathbf{k})\mathbf{Q}(\mathbf{k}) = \mathbf{S}^{\mathrm{PAO}}(\mathbf{k}), \tag{2.22}$$

where $\mathbf{S}^{\mathrm{PAO}}(\mathbf{k})$ is the Fourier image of the PAO overlap matrix:

$$\begin{aligned} S^{\mathrm{PAO}}_{ab}(\mathbf{k}) &= \langle \phi^{\mathrm{PAO}}_{a}(\mathbf{k}) | \phi^{\mathrm{PAO}}_{b}(\mathbf{k}) \rangle \\ &= \sum_{\mathcal{B}} \exp(\imath \mathbf{k} \mathbf{R}_{\mathcal{B}}) \langle \phi^{\mathrm{PAO}}_{a0} | \phi^{\mathrm{PAO}}_{b\mathcal{B}} \rangle. \end{aligned} \tag{2.23}$$

The Fourier transform (2.20) is again easily inverted,

$$|\phi^{\mathrm{PAO}}_{a}(\mathbf{k})\rangle = \frac{1}{\sqrt{n_{\mathbf{k}}}} \sum_{\mathcal{A}} \exp(\imath \mathbf{k} \mathbf{R}_{\mathcal{A}}) |\phi^{\mathrm{PAO}}_{a\mathcal{A}}\rangle. \tag{2.24}$$

Since the sets of PAOs or their Fourier images are redundant, the inverse of $\mathbf{S}^{\mathrm{PAO}}(\mathbf{k})$ does not exist (only the pseudoinverse!) and inversion of Eq. (2.21) becomes non straight-forward. In order to carry it out we introduce a rectangular matrix

$$\bar{\mathbf{Q}}(\mathbf{k}) = \mathbf{X}(\mathbf{k}) \mathbf{Q}^{\dagger}(\mathbf{k}) \tag{2.25}$$

($\mathbf{X}$ is a yet unspecified matrix in the basis of the PAO reciprocal images) with the property

$$\sum_{a\bar{a}} |\phi^{\mathrm{PAO}}_{a}(\mathbf{k})\rangle \bar{Q}_{a\bar{a}}(\mathbf{k}) Q_{\bar{a}c}(\mathbf{k}) = |\phi^{\mathrm{PAO}}_{c}(\mathbf{k})\rangle. \tag{2.26}$$

Multiplying equation (2.26) with the bra PAO $\langle \phi^{\mathrm{PAO}}_{d}(\mathbf{k})|$ and integrating yields

$$\mathbf{S}^{\mathrm{PAO}}(\mathbf{k}) \bar{\mathbf{Q}}(\mathbf{k}) \mathbf{Q}(\mathbf{k}) = \mathbf{S}^{\mathrm{PAO}}(\mathbf{k}) \mathbf{X}(\mathbf{k}) \mathbf{S}^{\mathrm{PAO}}(\mathbf{k}) = \mathbf{S}^{\mathrm{PAO}}(\mathbf{k}) \tag{2.27}$$

defining the matrix $\mathbf{X}(\mathbf{k})$ as a pseudoinverse of the reciprocal image of the PAO overlap $\mathbf{S}^{\mathrm{PAO}}(\mathbf{k})$ [71]. Expressing the right hand side of Eq. (2.26) via the canonical virtuals according to (2.21), one sees that the matrix $\bar{\mathbf{Q}}$ can serve as the transformation from the PAO to the canonical basis,

$$|\phi^{\mathrm{CAN}}_{\bar{a}}(\mathbf{k})\rangle = \sum_{a} \bar{Q}_{a\bar{a}}(\mathbf{k}) |\phi^{\mathrm{PAO}}_{a}(\mathbf{k})\rangle. \tag{2.28}$$

Transformation of the amplitude vectors and matrix-vector products

Now we are in a position to determine the form of the transformations for the CIS vectors $\mathbf{c}$ and $\Delta\mathbf{c}$ and the matrix-vector products $\mathbf{V}\Delta\mathbf{c}$. According

to the scheme described in Sec. 2.2.3, the trial vectors are transformed in each iteration from the canonical representation to the local one, while the matrix-vector products, evaluated in the direct space, are transformed back. If the starting trial vector is constructed in the direct space (*vide infra*) the local-canonical transformation is to be carried out also for that vector.

As it is seen from Eqs. (2.9) or (2.10) (or from the physicists notation Eq. (1.10)) the **Vc** vectors are transformed like ("ket") Wannier functions and complex conjugated ("bra") PAOs. The direct space translational symmetry unique vectors have one of the indices, in our case the WF index, restricted to the reference cell (*cf.* Sec. 2.2.1). Therefore the Fourier transform of the vectors involves only the sum over the PAO cell index or PAO **k** vector complex conjugated with respect to Eqs. (2.24) and (2.20):

$$(\mathbf{Vc})_i^a(\mathbf{k}) = \frac{1}{\sqrt{n_\mathbf{k}}} \sum_{\mathcal{A}} \exp(-\imath \mathbf{k}\mathbf{R}_\mathcal{A})(\mathbf{Vc})_i^{a\mathcal{A}} \tag{2.29}$$

and

$$(\mathbf{Vc})_i^{a\mathcal{A}} = \frac{1}{\sqrt{n_\mathbf{k}}} \sum_{\mathbf{k}} \exp(\imath \mathbf{k}\mathbf{R}_\mathcal{A})(\mathbf{Vc})_i^a(\mathbf{k}). \tag{2.30}$$

Next, according to Eqs. (2.16), (2.18), (2.21) and (2.28) the transformations between the canonical and WF-PAO reciprocal-image representations are then given by

$$(\mathbf{Vc})_{\bar{i}}^{\bar{a}}(\mathbf{k}) = \sum_{ia} \bar{Q}^*_{a\bar{a}}(\mathbf{k}) W^\dagger_{i\bar{i}}(\mathbf{k})(\mathbf{Vc})_i^a(\mathbf{k}), \tag{2.31}$$

and

$$(\mathbf{Vc})_i^a(\mathbf{k}) = \sum_{\bar{i}\bar{a}} Q^*_{\bar{a}a}(\mathbf{k}) W_{\bar{i}i}(\mathbf{k})(\mathbf{Vc})_{\bar{i}}^{\bar{a}}(\mathbf{k}). \tag{2.32}$$

Having established these relations, we can focus on the transformation laws for the CIS vectors. According to Eq. (2.12), the Hermitian conjugate of the trial CIS vectors $(\Delta\mathbf{c}^*)^i_{a\mathcal{A}}$ or $(\mathbf{c}^*)^i_{a\mathcal{A}}$ transforms contravariantly as opposed to the covariant vector (**Vc**). [71] Therefore the expressions for the transformations of $(\mathbf{c}^*)^i_a(\mathbf{k})$ and $(\mathbf{c}^*)^{\bar{i}}_{\bar{a}}(\mathbf{k})$ can be obtained directly from (2.31)

and (2.32), which after the complex conjugation of the left and right hand sides read

$$(\mathbf{c})^{\bar{i}}_{\bar{a}}(\mathbf{k}) = \sum_{ia} Q_{\bar{a}a}(\mathbf{k}) W^{\dagger}_{i\bar{i}}(\mathbf{k}) (\mathbf{c})^{i}_{a}(\mathbf{k}), \tag{2.33}$$

and

$$(\mathbf{c})^{i}_{a}(\mathbf{k}) = \sum_{\bar{i}\bar{a}} \bar{Q}_{a\bar{a}}(\mathbf{k}) W_{\bar{i}i}(\mathbf{k}) (\mathbf{c})^{\bar{i}}_{\bar{a}}(\mathbf{k}). \tag{2.34}$$

The same argument holds for the Fourier transformations of the CIS vectors.

$$(\mathbf{c})^{i}_{a}(\mathbf{k}) = \frac{1}{\sqrt{n_{\mathbf{k}}}} \sum_{\mathcal{A}} \exp(-\imath \mathbf{k}\mathbf{R}_{\mathcal{A}}) (\mathbf{c})^{i}_{a\mathcal{A}}. \tag{2.35}$$

and

$$(\mathbf{c})^{i}_{a\mathcal{A}} = \frac{1}{\sqrt{n_{\mathbf{k}}}} \sum_{\mathbf{k}} \exp(\imath \mathbf{k}\mathbf{R}_{\mathcal{A}}) (\mathbf{c})^{i}_{a}(\mathbf{k}). \tag{2.36}$$

2.2.5 Calculation of the Vc terms

As was already discussed above, the two-electron integral part of the matrix vector products is evaluated in the direct space. One of the main features of such a treatment is the possibility to use the periodic density fitting techniques as already devised for the periodic local MP2 method. [6,16,20] **Vc** consists of two distinct contributions ($^{\text{coul}}\mathbf{Vc}$) and ($^{\text{exch}}\mathbf{Vc}$):

$$(^{\text{coul}}\mathbf{Vc})^{a\mathcal{A}}_{i} = \sum_{j\mathcal{J}b\mathcal{B}} (a\mathcal{A}\, i|j\mathcal{J}\, b\mathcal{B}) c^{j\mathcal{J}}_{b\mathcal{B}} \tag{2.37}$$

and

$$(^{\text{exch}}\mathbf{Vc})^{a\mathcal{A}}_{i} = \sum_{j\mathcal{J}b\mathcal{B}} (j\mathcal{J}\, i|a\mathcal{A}\, b\mathcal{B}) c^{j\mathcal{J}}_{b\mathcal{B}}. \tag{2.38}$$

By virtue of the time reversal symmetry, the direct space quantities can be chosen real. The permutation of the "bra" and "ket" functions in the integrals is thus allowed.

The first term (2.37), appearing only in the singlet case, describes the Coulomb interaction between the neutral charge clouds of all the electron-hole pairs within the chosen basis. The corresponding diagram can be

interpreted as hopping between electron-hole pairs driven by their mutual Coulomb (or, in the long range, dipole-dipole) interaction. The second term (2.38), which originates from the exchange-type diagram represents the Coulomb attraction between the hole and electron distributions. This is actually the key term in the non-correlated description of an exciton, which is missing in time-dependent DFT, based on semi-local functionals. [63]

The computational costs of both contractions (2.37) and (2.38) scale nominally as $O(N^4)$ with respect to the unit-cell size. However, the transformation of the 4-index two-electron integrals to the WF-PAO basis scales as $O(N^5)$, which constitutes the scaling bottle-neck of the whole method. The density fitting approximation [9] factorizes the 4-index integrals through 3-index quantities and reduces the overall scaling to $O(N^4)$.

Density fitted ($^{\mathrm{coul}}\mathbf{Vc}$) term

We start with the Coulomb term Eq. (2.37). One can notice that, due to the slow decay of the Coulomb interaction, the index-$\mathcal{J}$ summation, with the $\mathcal{B}$-vectors close to $\mathcal{J}$, is long-range, and is not affected by the locality of the exciton (*i.e.* the range of $(\mathcal{B}-\mathcal{J})$-vectors with significant $c_{b\mathcal{B}}^{j\mathcal{J}}$ coefficients). Since the occupied-virtual products have zero charge, the integrals decay with interorbital distance as R^{-3}, which implies slow but unconditional convergence in the 1D and 2D cases, and just conditional convergence in the 3D case. Reciprocal-space density fitting [6, 16, 20] is preferable in this case, since the need for long-range summations of the Fourier transforms are justified by the nature of the contraction. According to Eqs. (19) and (20) in Ref. 6 the Coulomb integrals from (2.37) are expressed as:

$$(a\mathcal{A}\, i|j\mathcal{J}\, b\mathcal{B}) = \frac{1}{n_{\mathbf{k}_P}} \sum_{\mathbf{k}_P} \exp(-i\mathbf{k}_P\mathbf{R}_{\mathcal{J}}) \times \sum_{P} (ia\mathcal{A}|P)(\mathbf{k}_P)\left(d_P^{j\, b(\mathcal{B}\ominus\mathcal{J})}(\mathbf{k}_P)\right)^{*}. \tag{2.39}$$

involving the Fourier images of the 3-index integrals:

$$(i\,a\mathcal{A}|P)(\mathbf{k}_P) = \sum_{\mathcal{P}} (i\,a\mathcal{A}|P\mathcal{P}) \exp(\imath \mathbf{k}_P \mathbf{R}_{\mathcal{P}}) \tag{2.40}$$

and the DF coefficients

$$d_P^{j\,b(\mathcal{B}\ominus\mathcal{J})}(\mathbf{k}_P) = \sum_{Q} (j\,b(\mathcal{B}\ominus\mathcal{J})|Q)(\mathbf{k}_P)(Q|P)^{-1}(\mathbf{k}_P), \tag{2.41}$$

with

$$(Q|P)(\mathbf{k}_P) = \sum_{\mathcal{P}} (Q|P\mathcal{P}) \exp(\imath \mathbf{k}_P \mathbf{R}_{\mathcal{P}}), \tag{2.42}$$

where $(P|Q)^{-1}(\mathbf{k}_P)$ denotes the inverse of the $(P|Q)(\mathbf{k}_P)$ matrix at the **k**-point $\mathbf{k}_P$.

Now, inserting the factorization (2.39) into Eq. (2.37), changing the order of the summation, and changing the summation index $\mathcal{B}$ to $\mathcal{B}' = \mathcal{B}\ominus\mathcal{J}$ yields

$$\begin{aligned}({}^{\text{coul}}\mathbf{Vc})_i^{a\mathcal{A}} =& \frac{1}{n_{\mathbf{k}_P}} \sum_{jb\mathcal{B}'} \sum_{\mathbf{k}_P} \sum_{P} (i\,a\mathcal{A}|P)(\mathbf{k}_P) \\ & \times \left(d_P^{j\,b\mathcal{B}'}(\mathbf{k}_P)\right)^* c_{b\mathcal{B}'}^{j} \sum_{\mathcal{J}} \exp(-\imath \mathbf{k}_P \mathbf{R}_{\mathcal{J}})\end{aligned} \tag{2.43}$$

and the summation over the $\mathcal{J}$-vector completely decouples. When the number of the $\mathcal{J}$ vectors matches the chosen $\mathbf{k}_P$-mesh (i.e. lies within the period defined by the discrete Fourier transform, see below and Ref. 27), this summation reduces to $n_{\mathbf{k}_P}\delta_{\mathbf{k}_P,0}$, which finally leads to a significant simplification for the $({}^{\text{coul}}\mathbf{Vc})$ term:

$$({}^{\text{coul}}\mathbf{Vc})_i^{a\mathcal{A}} = \sum_{P} (i\,a\mathcal{A}|P)^*\big|_{\mathbf{k}_P=0} \sum_{j\,b\mathcal{B}'} d_P^{j\,b\mathcal{B}'}\big|_{\mathbf{k}_P=0} c_{b\mathcal{B}'}^{j}. \tag{2.44}$$

In other words, the reciprocal density fitting is now restricted to a single **k**-point. A similar simplification has been utilized in the density fitted calculations of the Coulomb potential in periodic AO-based HF or DFT

calculations [72–74]. The long-range summation over the $\mathcal{J}$-vector index is implicit, while the actual long-range contribution to the Coulomb interaction is now evaluated at the stage of the Fourier-transformation of the 3- and 2-index integrals Eqs. (2.41) and (2.42).

Furthermore, only the p-type GTOs of the auxiliary basis contribute to the terms with the slowest decay (s-GTO auxiliary functions are not used for the Coulomb term, *vide infra*). Fitting basis sets in our implementation contain only one shell of p-GTOs per center, the rest is formed by dipole-free or even completely momentless orbitals, which imply a much faster decay of the corresponding integrals. This effect leads to a much smaller number of long range terms, compared to the conventional formulation, where each of the $\phi_j\phi_{b\mathcal{B}}$ densities contains generally a dipole moment.

Density fitted ($^{\mathbf{exch}}$Vc) term

For the exchange term (2.38) the reciprocal fitting is possible, but not the most efficient way to proceed. In fact, in contrast to the Coulomb term, the fitted densities contain charge, which makes the Fourier lattice summations (2.41) and (2.42) conditionally convergent already for the 1D case. At the same time, the actual contraction in Eq. (2.38) is short range, provided the exciton is at least moderately localized (for very delocalized excitons the local direct space approach is not efficient anyway). Indeed, the actual summation range for the $\mathcal{J}$-index is dictated by the overlap between the Wannier functions, while for the $\mathcal{B}$-index additionally by the decay rate of the CIS coefficients $c^{j}_{b\mathcal{B}'}$.

The local direct-space density fitting [20, 75, 76] scheme is more appropriate in this case. In the present implementation we use a unique fit-domain D for all the two-electron integrals involved in the exchange term which allows us to use one-term robust density fitting [9, 76]:

$$(j\mathcal{J}\ i|a\mathcal{A}\ b\mathcal{B}) = \sum_{P\mathcal{P}\in D} d^{i\,j\mathcal{J}}_{P\mathcal{P}}\,(P\mathcal{P}|a\mathcal{A}\ b\mathcal{B}) \tag{2.45}$$

with

$$d^{i\,j\mathcal{J}}_{P\mathcal{P}} = \sum_{Q\mathcal{Q}\in D} (i\;j\mathcal{J}|Q\mathcal{Q})(Q\mathcal{Q}|P\mathcal{P})^{-1}. \tag{2.46}$$

Now $(Q\mathcal{Q}|P\mathcal{P})^{-1}$ is the inverse of the square metric matrix within the D-fit-domain. For the unique fit-domain only a single matrix inversion has to be carried out. At the same time, the fit domain should be sufficiently large to be able to provide support for all the $\phi_i\phi_{j\mathcal{J}}$ and $\phi_{a\mathcal{A}}\phi_{b\mathcal{B}}$ product densities, appearing in the calculation. For polymers it is generally not problematic to fulfill this condition. However, for 2D or 3D systems it can become critical, since the matrix to be inverted might become very large. A work is in progress on implementing the density-specific fit-domain technique, similar to that of Refs. 20,77, which circumvents this problem, but requires a three-term robust density fitting formalism [9].

The expression for the exchange term with the local density fitting approximation takes the form:

$$\begin{aligned}
({}^{\text{exch}}\mathbf{Vc})^{a\mathcal{A}}_{i} &= \sum_{j\mathcal{J}} \sum_{P\mathcal{P}\in D} d^{i\,j\mathcal{J}}_{P\mathcal{P}} \sum_{b\mathcal{B}} c^{j}_{b(\mathcal{B}\ominus\mathcal{J})} \\
&\quad \times (P(\mathcal{P}\ominus\mathcal{J})|a(\mathcal{A}\ominus\mathcal{J})\; b(\mathcal{B}\ominus\mathcal{J})) \\
&= \sum_{j\mathcal{J}} \sum_{P\mathcal{P}\in D} d^{i\,j\mathcal{J}}_{P\mathcal{P}} \sum_{b\mathcal{B}'} c^{j}_{b\mathcal{B}'} \\
&\quad \times (P(\mathcal{P}\ominus\mathcal{A})|a\; b(\mathcal{B}'\ominus\mathcal{A}\oplus\mathcal{J})).
\end{aligned} \tag{2.47}$$

Here we used the translational invariance of the integrals and the CIS coefficients and again redefined the $\mathcal{B}$ vector.

2.3 Implementation

2.3.1 Introduction of a k-mesh and the supercell

Since in practical calculations analytic integration of the Brillouin zone is not feasible, one has to introduce a finite **k**-mesh for the numerical

integration through the discrete Fourier transform. The number of **k**-points of the mesh needed for the calculation is not known apriori and therefore set as an input parameter.

In fact, the density of the mesh, sufficient for the calculation is strongly dependent on the locality of the exciton in the direct space. The back-Fourier-transform Eq. (2.36) of the CIS coefficients $(\mathbf{c})^i_a(\mathbf{k})$ with a finite number of **k**-points generates a periodic direct space image of it, with a period forming a supercell with a size exactly matching the number of the **k**-points. The physically relevant part of the exciton is located in the zero Wigner-Seitz supercell, since its periodically repeated images are artifacts of the finiteness of the **k**-mesh. [6,27] Therefore, in our approach we always restrict the range for the $\mathcal{A}$ vectors of the CIS coefficients $(\mathbf{c})^i_{a\mathcal{A}}$ or the trial vectors $(\Delta\mathbf{c})^i_{a\mathcal{A}}$ to this supercell (sc), setting the values outside the supercell to zero:

$$(\mathbf{c})^i_{a\mathcal{A}} = \begin{cases} \frac{1}{\sqrt{n_\mathbf{k}}} \sum_\mathbf{k} \exp(\imath\mathbf{k}\mathbf{R}_\mathcal{A})(\mathbf{c})^i_a(\mathbf{k}) & \text{if } \mathcal{A} \in \text{(sc)}, \\ 0 & \text{if } \mathcal{A} \notin \text{(sc)}. \end{cases} \tag{2.48}$$

Furthermore, as is well known from the discrete Fourier-Transform theory, it can be considered as an accurate numerical quadrature only if the resulting function goes to zero at the borders of the supercell, defined by the given **k**-mesh, or in other words, is localized within this supercell. This implies that the number of **k**-points needed for the correct description of an exciton strongly depends on its nature: the more local it is the less **k**-points in the reciprocal representation of the CIS coefficients are needed.

Next, even if the CIS coefficients are restricted to the supercell, the range of non-zero matrix-vector products $(\mathbf{Vc})^{a\mathcal{A}}_i$, which also depends on the sparsity of the Hamiltonian, can go beyond this range. This might violate the invariance of the small **h**-matrix (2.12) with respect to the representation (direct or reciprocal) of $\Delta\mathbf{c}$ and $\mathbf{H}\Delta\mathbf{c}$. Consider the small $\mathbf{h}^{(\text{dir})}$-matrix, defined in (2.12), evaluated in the direct space:

$$h^{(\text{dir})}_{rs} = \sum_{ia\mathcal{A}} (\Delta\mathbf{c}^{\dagger(r)})^i_{a\mathcal{A}} (\mathbf{H}\Delta\mathbf{c}^{(s)})^{a\mathcal{A}}_i. \tag{2.49}$$

The $\mathcal{A}$-vectors in $(\mathbf{H}\Delta\mathbf{c})_i^{a\mathcal{A}}$ outside the supercell do not contribute to the matrix $\mathbf{h}^{(\mathrm{dir})}$, since the matching CIS coefficients are zero beyond the supercell by construction (2.48). However, if the $\mathbf{h}$-matrix is calculated in the reciprocal space employing the vector $(\mathbf{H}\Delta\mathbf{c})(\mathbf{k})$ (as is done in our approach), the inclusion of the outer tails of the $(\mathbf{H}\Delta\mathbf{c})_i^{a\mathcal{A}}$ in the Fourier transform (2.29), would have an effect on the result. Indeed, according to Eqs. (2.12) and (2.29) one obtains:

$$\begin{aligned} h_{rs}^{(\mathrm{recipr})} &= \sum_{ia\mathbf{k}} (\Delta\mathbf{c}^{\dagger(r)})_a^i(\mathbf{k})(\mathbf{H}\Delta\mathbf{c}^{(s)})_i^a(\mathbf{k}) \\ &= \sum_{ia\mathbf{k}} (\Delta\mathbf{c}^{\dagger(r)})_a^i(\mathbf{k}) \\ &\quad \times \left[\frac{1}{\sqrt{n_{\mathbf{k}}}} \sum_{\mathcal{A}} \exp(-\imath\mathbf{k}\mathbf{R}_{\mathcal{A}})(\mathbf{H}\Delta\mathbf{c}^{(r)})_i^{a\mathcal{A}} \right] \end{aligned} \tag{2.50}$$

The summation range of the index $\mathcal{A}$ can be separated in $\mathcal{A} \in (sc)$ and $\mathcal{A} \notin (sc)$. The former sum constitutes the direct space matrix $\mathbf{h}^{(\mathrm{dir})}$, whereas the latter appears as a generally non-zero term in the equation:

$$\begin{aligned} h_{rs}^{(\mathrm{recipr})} = h_{rs}^{(\mathrm{dir})} &+ \frac{1}{\sqrt{n_{\mathbf{k}}}} \sum_{\mathcal{A}\notin(sc)} \sum_{ia} (\mathbf{H}\Delta\mathbf{c}^{(r)})_i^{a\mathcal{A}} \\ &\times \sum_{\mathbf{k}} \exp(-\imath\mathbf{k}\mathbf{R}_{\mathcal{A}})(\Delta\mathbf{c}^{\dagger(r)})_a^i(\mathbf{k}). \end{aligned} \tag{2.51}$$

This shows that $\mathbf{h}^{(\mathrm{recipr})}$-matrix, evaluated in the reciprocal space, differs from $\mathbf{h}^{(\mathrm{dir})}$, if the elements of $(\mathbf{H}\Delta\mathbf{c})_i^{a\mathcal{A}}$ beyond the supercell are included in the Fourier transform. In our method we calculate the two-electron part $(\mathbf{V}\Delta\mathbf{c})_i^{a\mathcal{A}}$ of the full vector $(\mathbf{H}\Delta\mathbf{c})_i^{a\mathcal{A}}$ in the direct space and then transform it to the reciprocal space. In order to enforce the invariance of the $\mathbf{h}$-matrix, the values of $(\mathbf{V}\Delta\mathbf{c})_i^{a\mathcal{A}}$ beyond the supercell are not included in the Fourier transform (2.29) (and essentially not computed), thus making the second summand in Eq. (2.51) zero.

2.3.2 The norm of the CIS vector

Since the Davidson diagonalization procedure is carried out in the reciprocal space each new trial vector is orthogonalized to the previous ones and normalized to unity, which also guarantees the normalization of the actual CIS vectors in the reciprocal space. The reciprocal space images of the local CIS coefficients are also normalized,

$$N^{(\text{recipr})} = \sum_{iab\mathbf{k}} c_a^{i*}(\mathbf{k}) S_{a\,b}^{\text{PAO}}(\mathbf{k}) c_b^i(\mathbf{k}) = 1. \tag{2.52}$$

The direct space norm of the CIS vectors

$$\begin{aligned} N^{(\text{dir})} &= \sum_{iab} \sum_{\mathcal{AB}} c_{a\mathcal{A}}^{i*} S_{a\mathcal{A}\,b\mathcal{B}}^{\text{PAO}} c_{b\mathcal{B}}^i \\ &= \sum_{iab} \sum_{\mathcal{AB}} c_{a\mathcal{A}}^{i*} S_{a\,b(\mathcal{B}\ominus\mathcal{A})}^{(\text{PAO})} c_{b\mathcal{B}'}^i \end{aligned} \tag{2.53}$$

however, might differ from unity. Indeed, rewriting Eq. (2.53) via Fourier transforms of the reciprocal images of the involved quantities and restricting the values to the supercell yields:

$$\begin{aligned} N^{(\text{dir})} =& \frac{1}{n_{\mathbf{k}}^2} \sum_{iab} \sum_{\mathbf{k}\mathbf{k}'\mathbf{k}''} c_a^{i*}(\mathbf{k}) S_{a\,b}^{\text{PAO}}(\mathbf{k}') c_b^i(\mathbf{k}'') \\ &\times \sum_{A\in(\text{sc})} \exp(-\imath \mathbf{k}\mathbf{R}_{\mathcal{A}}) \\ &\times \sum_{\substack{\mathcal{B}\in(\text{sc}) \\ \forall(\mathcal{B}-\mathcal{A})\in(\text{sc})}} \exp(-\imath \mathbf{k}'(\mathbf{R}_{\mathcal{B}} - \mathbf{R}_{\mathcal{A}})) \exp(\imath \mathbf{k}'' \mathbf{R}_{\mathcal{B}}) \end{aligned} \tag{2.54}$$

In the last sum of (2.54) not all vectors $\mathcal{B}$ from the supercell are included, but only those, which for a given $\mathcal{A}$ fulfill the condition $(\mathcal{B} \ominus \mathcal{A}) \in (\text{sc})$, since otherwise the back-Fourier transform would generate artificial periodic images of the overlap matrix. This truncation actually destroys the direct link to the reciprocal norm (2.52). In order to reestablish this connection

we subtract and add the missing terms:

$$\begin{aligned} N^{(\text{direct})} =& \frac{1}{n_{\mathbf{k}}^2} \sum_{iab} \sum_{\mathbf{k}\mathbf{k}'\mathbf{k}''} c_a^{i*}(\mathbf{k}) S_{a\,b}^{\text{PAO}}(\mathbf{k}') c_b^i(\mathbf{k}'') \\ & \times \sum_{A\in(\text{sc})} \exp(-\imath(\mathbf{k}-\mathbf{k}')\mathbf{R}_{\mathcal{A}}) \\ & \times \Bigg[\sum_{\mathcal{B}\in(\text{sc})} \exp(-\imath(\mathbf{k}'-\mathbf{k}'')\mathbf{R}_{\mathcal{B}}) \\ & - \sum_{\substack{\mathcal{B}\in(\text{sc}) \\ \forall(\mathcal{B}\ominus\mathcal{A}) \\ \notin(\text{sc})}} \exp(-\imath(\mathbf{k}'-\mathbf{k}'')\mathbf{R}_{\mathcal{B}}) \Bigg] \\ =& \sum_{iab} \sum_{\mathbf{k}\mathbf{k}'\mathbf{k}''} c_a^{i*}(\mathbf{k}) S_{a\,b}^{\text{PAO}}(\mathbf{k}') c_b^i(\mathbf{k}'') \delta_{\mathbf{k}'',\mathbf{k}'} \delta_{\mathbf{k}',\mathbf{k}} \\ & - \sum_{A\in(\text{sc})} c_{a\mathcal{A}}^{i*} \sum_{\substack{\mathcal{B}\in(\text{sc}) \\ \forall(\mathcal{B}\ominus\mathcal{A})\notin(\text{sc})}} S_{a\,b(\mathcal{B}\ominus\mathcal{A})}^{\text{PAO}} c_{b\mathcal{B}}^i. \end{aligned} \tag{2.55}$$

The first term is actually the reciprocal norm, Eq. (2.52), *i.e.* 1, but the subtrahend is not necessarily zero. We note that, since both $\mathcal{B}$ and $\mathcal{A}$ belong to the supercell, their difference, which for this term is outside the supercell, can be brought there by adding or subtracting the supercell translation vector $\mathbf{R}_{\text{sc}}$. Since for any $\mathbf{k}$ point from the chosen mesh $\exp(\pm\imath\mathbf{k}\mathbf{R}_{\text{sc}}) = 1$, this exponential can be harmlessly added to the back Fourier transform of the overlap matrix $S_{a\,b}^{\text{PAO}}(\mathbf{k}')$, such that $S_{a\,b(\mathcal{B}\ominus\mathcal{A})}^{\text{PAO}}$ is replaced by the matrix $S_{a\,b(\mathcal{B}\ominus\mathcal{A}\pm\mathbf{R}_{\text{sc}}))}^{\text{PAO}}$. This simplifies the expression for the direct norm to

$$N^{(\text{dir})} = 1 - \sum_{A\in(\text{sc})} c_{a\mathcal{A}}^{i*} \sum_{\substack{\mathcal{B}\in(\text{sc}) \\ \forall(\mathcal{B}\ominus\mathcal{A}\pm\mathbf{R}_{\text{sc}}) \\ \in(\text{sc})}} S_{a\,b(\mathcal{B}\ominus\mathcal{A}\pm\mathbf{R}_{\text{sc}}))}^{\text{PAO}} c_{b\mathcal{B}}^i. \tag{2.56}$$

Now, due to the locality of the PAO overlap matrix an element $S_{a\,b(\mathcal{B}\ominus\mathcal{A}\pm\mathbf{R}_{\text{sc}}))}^{\text{PAO}}$ is non-negligible only if the vector $\mathbf{R}_{\mathcal{B}} - \mathbf{R}_{\mathcal{A}} \pm \mathbf{R}_{\text{sc}}$ is small (*i.e.* close to the reference cell). Since both vectors $\mathcal{A}$ and $\mathcal{B}$ are restricted to the Wigner-Seitz supercell, this happens only if both of them are located at its edges

(actually at the opposite sides of it). If the exciton is well localized within the supercell, the CIS coefficients $c^i_{a\mathcal{A}}$ and $c^i_{b\mathcal{B}}$ are small at the edges, which makes the second term in (2.56) close to zero, and the direct space norm to unity. In other words, when the chosen **k**-mesh is adequate for describing the exciton, the direct norm is close to the reciprocal one. This property suggests that the direct space norm can be used as an indicator for the reliability of the chosen **k**-mesh. This issue is illustrated in Sec. 2.4 on a set of test calculations.

2.3.3 Evaluation of the transformation matrices

The implemented CIS method needs the underlying Hartree-Fock ground state solution, which is provided by the CRYSTAL code. [69] Namely, it delivers the Fock matrix, and the information on the structural parameters, basis set and the symmetry. In addition, the CRYSTAL code generates Wannier functions according to the Wannierization-localization-symmetrization procedure by Zicovich-Wilson [23], Casassa [78] and coworkers. The constructed Wannier functions are represented via the AO expansion coefficients.

Using these quantities it is possible to evaluate the transformation matrices $\mathbf{W}(\mathbf{k})$, $\mathbf{Q}(\mathbf{k})$ and $\bar{\mathbf{Q}}(\mathbf{k})$ (*cf.* Sec. 2.2.4) and the explicit direct space AO representation of the PAOs, needed for the calculation of the $\mathbf{Vc}$-terms (*cf.* Sec. 2.2.5). First, the AO Fock matrix, overlap matrix and WF coefficients are Fourier transformed to the reciprocal space. Using the latter, the Fock matrix can be transformed to the basis of the Fourier images of the Wannier functions. The eigenvectors of this matrix at each **k**-point form the transformation matrices $\mathbf{W}^{+}(\mathbf{k})$ [Eq. ((2.18)].

Next, the projector from the occupied manifold (2.19) is also constructed

in the reciprocal space:

$$1 - \hat{P}(\mathbf{k}) = 1 - \sum_{\bar{i}} |\phi_{\bar{i}}^{\mathrm{CAN}}(\mathbf{k})\rangle\langle\phi_{\bar{i}}^{\mathrm{CAN}}(\mathbf{k})| = \sum_{\bar{a}} |\phi_{\bar{a}}^{\mathrm{CAN}}(\mathbf{k})\rangle\langle\phi_{\bar{a}}^{\mathrm{CAN}}(\mathbf{k})|, \tag{2.57}$$

and used to calculate the reciprocal images of the PAOs, which are then back-Fourier-transformed to the direct space. [79]

From (2.57) and (2.19) it follows that the reciprocal space AO expansion coefficients $C_{\mu a}^{\mathrm{PAO}}(\mathbf{k})$ of the PAOs can be expressed via the AO coefficients of canonical virtual orbitals $C_{\mu\bar{a}}^{\mathrm{CAN}}(\mathbf{k})$ as:

$$C_{\mu a}^{\mathrm{PAO}}(\mathbf{k}) = \sum_{\bar{a}\mu'} C_{\mu\bar{a}}^{\mathrm{CAN}}(\mathbf{k}) C_{\mu'\bar{a}}^{\mathrm{CAN}\dagger}(\mathbf{k}) S_{\mu'\nu}^{\mathrm{AO}}(\mathbf{k})|_{a=\nu} \tag{2.58}$$

Now, expressing the orbitals in the right- and left-hand-side of Eq. (2.21) via their AO expansion, and using Eq. (2.58) yields the formula for the practical evaluation of the $\mathbf{Q}(\mathbf{k})$-transformation:

$$Q_{\bar{a}a}(\mathbf{k}) = \sum_{\mu} C_{\bar{a}\mu}^{\mathrm{CAN}\dagger} S_{\mu\nu}^{\mathrm{AO}}(\mathbf{k})|_{a=\nu} \tag{2.59}$$

As mentioned in Sec. 2.2.4 the basis of the reciprocal images of the PAOs is redundant. Indeed, the number of the PAOs so-obtained at each $\mathbf{k}$-point is equal to the number of AOs, they are constructed from, while the actual virtual space has a dimensionality lower than that of the AOs by the number of the occupied states at a given $\mathbf{k}$-point. The pseudoinverse $\mathbf{X}(\mathbf{k})$ of the $\mathbf{S}^{\mathrm{PAO}}(\mathbf{k})$ matrix is constructed via its singular value decomposition, namely, by diagonalizing the $\mathbf{S}^{\mathrm{PAO}}(\mathbf{k})$ matrix, inverting its non-zero eigenvalues and back-transforming this diagonal matrix. The $\bar{\mathbf{Q}}(\mathbf{k})$-transformation is then generated according to (2.25).

2.3.4 Density fitting and the ranges for lattice summations

For the correct density fitting treatment of the Coulomb (2.44) and exchange (2.47) terms the ranges for various vector indices are to be determined. In

the Coulomb term (Eqs. (2.40) to (2.42) and (2.44)) these are the indices $\mathcal{P}$ and $\mathcal{B}$. The range for the latter index can be easily prescreened. It, firstly, should not go beyond the supercell, since the contraction along this index with the CIS coefficients outside the supercell is zero by construction. And, secondly, it should be sufficiently close to the reference cell, since otherwise the corresponding 3-index integral or fitting coefficient will be negligible.

The summations involving the $\mathcal{P}$-index in Eqs. (2.41) and (2.42) are more delicate. As mentioned above, the fitted densities are chargeless, which implies a slow but absolute $1/R^3$ convergence of the Fourier series in the 1D case. In order to maintain this convergence rate also the auxiliary functions have to be chargeless. This can be elegantly achieved by using a combined GTO/Poisson auxiliary basis sets [6, 19, 20]. The main body of the fitting basis is formed by the momentless Poisson type-orbitals (PTOs) — Laplacians of GTOs [17, 18]. Coulomb integrals with PTOs reduce to one-electron overlap or kinetic energy integrals, which are easier to calculate and, most importantly, decaying exponentially with the interorbital distance. This property makes the vast majority of the 3- and 2-index Coulomb integrals essentially short range. Since the momentless Poisson-type fitting functions alone cannot describe the true densities, the auxiliary basis sets are complemented with a few GTOs: one shell of each angular momentum (up to *g*-type) per center. Since the fitted densities in the Coulomb term are chargeless, *s*-GTOs, causing the most problematic divergent terms, are not needed. In the 1D case the Fourier series (2.41) and (2.42), involving all the included auxiliary GTOs converge. The evaluations and Fourier summations of the 3- and 2-index integrals are performed on the fly until the values of the integrals drop below a certain threshold (10^{-7} by default). Due to the small number of auxiliary GTOs and the need for only one $\mathbf{k}$-point in the Coulomb density fitting, this is an inexpensive procedure. In higher dimensionalities the convergence rate of these Fourier series will slow down, and the number of the integrals to be evaluated will grow considerably. In this case the multipole expansion of

the integrals combined with convergence acceleration techniques like the Ewald procedure will become a prerequisite.

The density fitting procedure used for the exchange term, as is seen from Eq. (2.47), is quite different. Firstly, the local fitting scheme is used, which implies an *a priori* truncation of the auxiliary space to a fit-domain. For the robust fitting the fit-domain should cover all the fitted densities, in our case it is $\phi_i\phi_{j\mathcal{J}}$ and $\phi_{a\mathcal{A}}\phi_{b\mathcal{B}}$. Due to the locality of the Wannier functions the integrals involving the $\phi_i\phi_{j\mathcal{J}}$ densities quickly fade to zero with increasing $\mathcal{J}$. Therefore the range for this index can be prescreened by comparing the products of the WFs LCAO coefficients with a certain threshold.

The densities $\phi_{a\mathcal{A}}\phi_{b\mathcal{B}}$ possess similar decay properties, now depending on the length of the $\mathcal{B}\ominus\mathcal{A}$ vectors, which can be prescreened. The restriction of the $\mathcal{A}$-vector to the supercell (*cf.* Sec. 2.3.1) determines the range for the possible values of the $\mathcal{B}$-vector. This range can be further reduced by taking into account the contraction of the integral with the CIS vectors $c_{b\mathcal{B}}^{j\mathcal{J}}$ (2.38). The latter quantity is zero if the vector $\mathcal{B}\ominus\mathcal{J}$ is outside the supercell. Then using the prescreened range for $\mathcal{J}$, one can sort out the unneeded $\mathcal{B}$-vectors. This range for the $\mathcal{B}$-vectors, which is the most extended among those considered here, determines the range for the $\mathcal{P}$ vectors of the fit-domain.

Analogously to the Coulomb term, a combined PTO/GTO fitting basis set is used for the fitting of the exchange term. Although the property of the exponential decay of the PTO-based integrals is here of less relevance, since the range of the fitting functions is anyway restricted to the fit domain, the savings in the integral generation are still significant. In contrast to the Coulomb-part, the fitted densities of the exchange-integrals do possess charges, which requires inclusion of the *s*-GTO auxiliary functions. Since evaluation of 3-index integrals with such functions within the fit-domain is relatively inexpensive, the *s*-type-orbital part of the auxiliary basis for the exchange term is represented solely by GTOs.

In the evaluation of both the ${}^{\text{coul}}\mathbf{Vc}$ and ${}^{\text{exch}}\mathbf{Vc}$ terms, the contraction of the ket-side 3-index integrals with the CIS coefficients is done first, as is shown in Eqs. (2.44) and (2.47). Subsequently the result of this contraction, which has a much smaller size than the initial 3-index integral, is contracted with the DF-coefficients. This order of matrix multiplications, which scales nominally as $O(N^4)$, explicitly avoids the expensive $O(N^5)$-scaling assembly of the 4-index integrals.

The actual scaling of the computational cost of the method can be considered relative to two parameters: the size of the unit cell, and the number of **k**-points, which defines the size of the supercell. The latter quantity essentially depends on the locality of the exciton and is not known beforehand. Since the ranges of both the excitonic $\mathcal{A}$ ($\mathcal{B}$) and auxiliary $\mathcal{P}$ lattice vectors are affected by the increase of the supercell, the contractions in Eqs. (2.44) and (2.47) scale quadratically with its size. On the other hand, when the unit cell size is increased, the computational cost scales only linearly, since the supercell size can then be proportionally decreased, if the locality of the exciton under consideration remains unchanged. If this is not the case, then the linear scaling with respect to cell size is weighted with the quadratic scaling due to the additional increase or decrease of the spread of the exciton. This analysis shows that the method is more sensitive to the diffuseness of the exciton than to the number of atoms in the unit cell. A further reduction of the former quadratic to linear scaling is possible when local density fitting schemes [20,75,77] are applied.

2.3.5 The initial guess for the Davidson procedure

Since the cost and correctness of the local scheme, as described above, essentially depends on the locality of the exciton, the starting guess for the Davidson procedure has to be chosen with care. Under such circumstances it is natural to use a direct-space defined starting guess, which can be constructed to be local. We have investigated three types of direct space starting guesses and one in reciprocal space:

1. Excitations from all WFs to all PAOs within the zero cell with an equal weight. This simple starting vector is well localized, but depends on the choice of the origin of the unit cell and favours totally symmetric excitons (with respect to the point symmetry group of the center of the unit cell).

2. Equiweighted excitations from the zero-cell WFs onto the PAOs within their Boughton-Pulay PAO-domains [66]. Such a vector is even more localized than in the previous case and at the same time does not depend on the choice of the origin. However, it is still totally symmetric, which can be inadequate for an exciton with some other symmetry.

3. Several starting vectors corresponding to smallest values of the differences between the diagonal elements of the Fock matrix in PAO/WF basis. This mimics HOMO-LUMO-like excitations, yet in direct space. The starting vectors can be of different symmetries, which makes it more flexible than the previous two cases. However, there is no guarantee that the vectors chosen in such a manner would contribute significantly to the lowest exciton. If not, this starting guess, which uses several starting vectors rather than just one, might increase the cost of the calculations without a significant gain in the convergence.

4. The staring vector in the reciprocal space with the equiweighted vertical excitations for all $\mathbf{k}$-points from the highest occupied band to the lowest virtual band. Since we are focusing on the lowest-energy exciton, these are the excitations which are expected to contribute the most. The symmetry of the exciton is also likely to be correctly described by these excitations. However, the locality of the starting vector transformed to the direct space might be lost. In fact, the convergence of the Fourier series is critically affected by discontinuities in the Fourier-expanded function. As was shown by Kohn [80] for

1D and des Cloizeaux [81] for 3D cases on the example of the Fourier transforms connecting Bloch and Wannier functions, the exponential decay of the latter can be achieved only if the corresponding band is separated from the other bands by energy gaps. In our context, the Fourier-transform of an improperly chosen reciprocal trial vector looses its localization in the direct space, which, when exceeding the supercell, can become troublesome for our method. Even when excitations from the whole band are included in the reciprocal starting guess, making it a smooth function of $\mathbf{k}$, a possible intersection with other bands can lead to non-analyticity [80] and, thus, to a poor localization in the direct space. Probably, such intersections are unlikely in the 1D case and, as the calculations have shown, this reciprocal starting guess is the most efficient for the systems studied here (*cf.* Sec. 2.4). However, in 3D systems, where the lower conduction band as a rule crosses with higher ones, this might no longer be the case.

2.4 Calculations

The method described above has been applied to several 1-D test systems. In these calculations we investigate the efficiency and reliability of the method, in particular the convergence with respect to the number of $\mathbf{k}$-points, the accuracy of the density fitting approximation, *etc*. We have considered van-der-Waals (Ar), H-bonded (H_2O), ionic (LiH) 1D chains and several "real" covalent polymers: polyethylene, polystyrene and polybiphenyl. Some of the studied systems do not exist in 1D form in reality, but can serve as prototypes for 3D solids and provide information on the locality of excitons, and thus the feasibility of the local scheme, for such crystals. Table 2.1 compiles the results of the CIS calculations for singlet and triplet Γ-point excitons. The geometries of the covalent polymers have been optimized with the CRYSTAL code [69] at the DFT/B3LYP level, for the other systems a 1D cut from the 3D solid was taken. Some of the

studied systems are sketched in Fig. 2.1, and all the structural data are given explicitly in the supplementary material in Appendix A.1.

(i) parallel polybiphenyl

(ii) perpendicular polybiphenyl

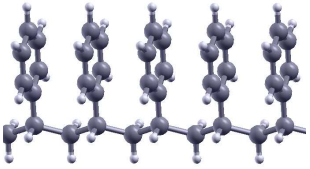

(iii) isotactic polystyrene

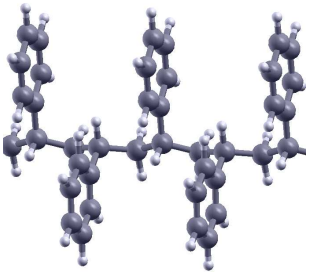

(iv) syndiotactic polystyrene

Figure 2.1: Polybiphenyl with parallel (i) and perpendicular (ii) alignment of the benzene rings and polystyrene in iso- (iii) and syndiotactic (iv) form.

The numbers of **k**-points reported in table 2.1 corresponds to the converged (with respect to this parameter) energies. This is one of the key parameters, since it reflects the locality of the excitons. One can see that in the weakly bound argon polymer, as anticipated, the excitons are rather local. In the ionic LiH and H-bonded water polymers they are somewhat

less localized (note the "doubled" unit cell in the latter system consisting of two molecular units). However, neither of these excitons can be considered as delocalized, so the **k**-meshes needed in such systems and the corresponding direct space supercells can be processed without big effort, also, presumably, in the 3-D case. On the other hand, in the covalent systems studied here the locality of the exciton depends essentially on the structure and the type of the excitation. In the case of polyethylene the lowest exciton, which spreads out along the C-C bonds, is noticeably less localized than in polystyrene, where it corresponds to a $\pi \rightarrow \pi^*$-type exciton well localized on the ring. In poly-biphenyl with parallel orientation of the rings the same $\pi \rightarrow \pi^*$-exciton can essentially delocalize. At the same time, the 90°-orientation of the rings in the perpendicular poly-biphenyl blocks this π-type delocalization and the exciton becomes well localized.

Apparently, there exists a link between the value of the excitation energy and the locality of the exciton. Indeed, the exciton in the argon chain, which has the largest HOCO-LUCO difference and highest excitation energy among the systems studied here, is the most localized. Similarly, the low excitation energy in parallel poly-biphenyl corresponds to a relatively delocalized exciton. However, this tendency is not unequivocal, since also short-range effects can influence the excitation energy significantly. Indeed, the excitons in LiH, and especially polystyrene are rather local and at the same time considerably less energetic than the much more delocalized exciton of polyethylene.

The Coulomb term (2.44), which is present in the CIS Hamiltonian only for the singlet states, is well known to produce a destabilizing contribution. This effect is reproduced in our calculations, where the triplet excitation energies are always lower than the corresponding singlet ones, and for $\pi \rightarrow \pi^*$-type of the excitation – quite substantially, indeed. Additionally, the Coulomb term might facilitate a further delocalization of the exciton, since in some (but not all) cases the triplet excitons are noticeably more localized. Similar effects have been observed also in local CC2 calculations

Table 2.1: Number of atoms per unit cell (n_{atoms}), Hartree-Fock HOCO-LUCO band gaps (E_g), negatives of the highest occupied orbital energies ($-\epsilon_{HOCO}$), number of **k**-points used, vertical excitation energies to the lowest singlet and triplet exciton state. The fitting basis set related to the cc-pVDZ AO basis was used. The elapsed times were measured on a single core Intel Xeon E5450 @ 3.00 GHz.

				singlet			triplet		
system	n_{atoms}	E_g / eV	$-\epsilon_{HOCO}$ / eV	$n_{\mathbf{k}}$	ω / eV	time	$n_{\mathbf{k}}$	ω / eV	time
Ar[a]	1	30.864	15.555	5	21.734	5s	4	20.519	3s
LiH[a]	2	11.485	9.269	8	6.606	18s	8	5.502	16s
H_2O[a,c]	6	18.834	13.172	5	10.378	54s	3	9.485	21s
all-*trans*-C_2H_4[a]	6	16.996	10.902	11	11.748	~11min	6	10.547	~4min
biphenyl (∥)[b]	11	7.754	6.497	14	3.835	~100min	11	2.192	~60min
biphenyl (⊥)[b,c]	22	12.301	8.860	3	6.385	~40min	3	3.274	~35min
styrene (iso)[b]	16	10.863	5.518	5	6.454	~80min	5	3.199	~50min
styrene (syn)[b,c]	32	12.281	8.141	3	6.350	~3h40min	3	3.316	~2h30min

[a] Calculated with 6-31G** orbital basis set.

[b] Calculated with 6-31G orbital basis set with increased exponent of the most diffuse sp-function of carbon from 0.16871448 to 0.18.

[c] The unit cell includes two molecular units.

on extended molecules. [33]

An interesting effect is observed in several of the examples studied, namely the argon chain, the polyethylene and the isotactic polystyrene, where the negative of the HOCO energy (*i.e.*, an uncorrelated and unrelaxed Koopmans theorem estimate of the ionization potential, is noticeably lower than the corresponding CIS excitation energy). This observation suggests that either the CIS/6-31G** treatment is inadequate or the physics of these system forbids bound excited states.

First we address the case of the polyethylene. The experimental values for the ionization potential and the band gap, which amount to 8.8 eV and 7.6 eV respectively, [82] confirm the existence of bound states in this system. At the same time, the discrepancy between the experimental and calculated excitation energy, which is more than 4 eV, is too large compared to the anticipated error of the CIS method of 1-2 eV (*cf.*, *e.g.* Refs 83 or 84). This issue has already been investigated in Ref. 48. Calculations, as well experiments on linear alkanes, [85] indicate that the lowest excited states in polyethylene are of a Rydberg type. This explains both the low values of the experimental or calculated ionization potential, and the inability of our calculation to reproduce the lowest excited states. In fact, a proper description of Rydberg states requires very diffuse basis functions, needed to represent the density of the excited electron perpendicular to the polymer chain. The authors of Ref. 48 did so by employing the 6-31++G basis and obtained a value of 9.2 eV, which lies within the typical CIS error bar. The CIS states, calculated by employing the non-diffuse 6-31G** basis, which obviously allows for delocalization, but only along the polymer chain, are rather valence states and not related to the experimentally observed Rydberg states. Our code presently does not allow for using very diffuse basis functions for covalent polymers, because of convergence problems in the underlying Hartree-Fock calculations. In order to be able to study such Rydberg states we are planning to adapt the dual basis set scheme developed for LMP2 [79]. However, in 3D closely packed systems Rydberg

states are not possible and the need for diffuse basis functions vanishes. Low-lying excited states in 3D-crystals are expected to be of valence type.

For the case of the argon chain, owing to the sparser atomic arrangement, it was possible to include diffuse basis functions. We have added in the basis set an additional sp-shell with a relatively diffuse exponent of 0.07 Bohr^{-2}. The effect of this addition on the lowest excitation is dramatic: it reduces the value of the excitation energy from 21.7 eV to 12.9 eV, well below the ionization potential, properly capturing the low-lying Rydberg states.

Finally, the effect of a lower ionization potential is also observed in the isotactic polystyrene, but not in the syndiotactic one. At the same time, the excitation energy for the lowest state, which represents the $\pi \rightarrow \pi^*$ transition on the benzene rings, is virtually the same for both. A possible reason for the shift of the HOCO energy in the isotactic conformer is a noticeable elongation of the aliphatic C-C bond (1.69 Å vs 1.55 Å in the syndiotactic one) due to the mutual repulsion of the benzene rings.

Concerning the efficiency, as discussed in Sec. 2.3.4 the computational time depends on the size of the unit cell (asymptotically linearly) and on the localization of the exciton (asymptotically quadratically). This scaling behaviour is almost exactly reproduced in our calculations on the two polybiphenyl or polystyrene conformers (*cf.* Table 2.1). Consider, for example, the cases of the singlet exciton in parallel and perpendicular polybiphenyl. The unit cell of the latter is twice as large as that of the former, which should lead to an increase of the computational time by a factor of 2, provided the **k**-net is reduced proportionally (*i.e.* from 14 to 7 **k**-points). However, the **k**-net due to an additional localization of the exciton in the perpendicular conformer has been reduced to 3 **k**-points, which should contribute to the reduction of the computational time by a square of 7/3. The product of these two factors $2(3/7)^2 = 0.367$ predicts a reduction of the computational time in the perpendicular polybiphenyl to 37 minutes, while the observed time was 40 minutes.

As the timings in Table 2.1 show, the local CIS calculations for polymers are generally not very expensive and linear scaling allows one to increase the unit cell size without a big computational effort. The diffuseness of the excitons is a more demanding issue, but in the case of 1D systems it is still not a severe problem as concerns the computational time. In 3D systems, however, the quadratic scaling can lead to a substantial loss in efficiency, since there it corresponds to a R^6 scaling with exciton localization radius R. As was mentioned above this undesired feature can be circumvented by introduction of a specific fit-domains for each product density to be fitted.

The direct space representation of an exciton provides an illustrative tool to analyze its locality. Fig. 2.2 shows the histogram of the maximal CIS coefficients $\max_{ia}|c^i_{a\mathcal{A}}|$ for different cells $\mathcal{A}$. It is seen that the lowest energy exciton in LiH is well localized within a supercell consisting of 8-9 unit cells, which matches the 8-**k**-point convergence of the energy (*cf.* Table 2.1). The two conformers of polybiphenyl is another good example to analyze the exciton's locality. The singlet exciton in the parallel conformation, as follows from table 2.1, requires 14 **k**-points, while the perpendicular conformer only 3 (but with doubled unit cell). Again the direct space interpretation of this behaviour can be observed in Fig. 2.2, where the exciton of the parallel polybiphenyl is localized within 15 unit cells, while its the perpendicular counterpart is substantially more localized and "needs" just 3 doubled unit cells.

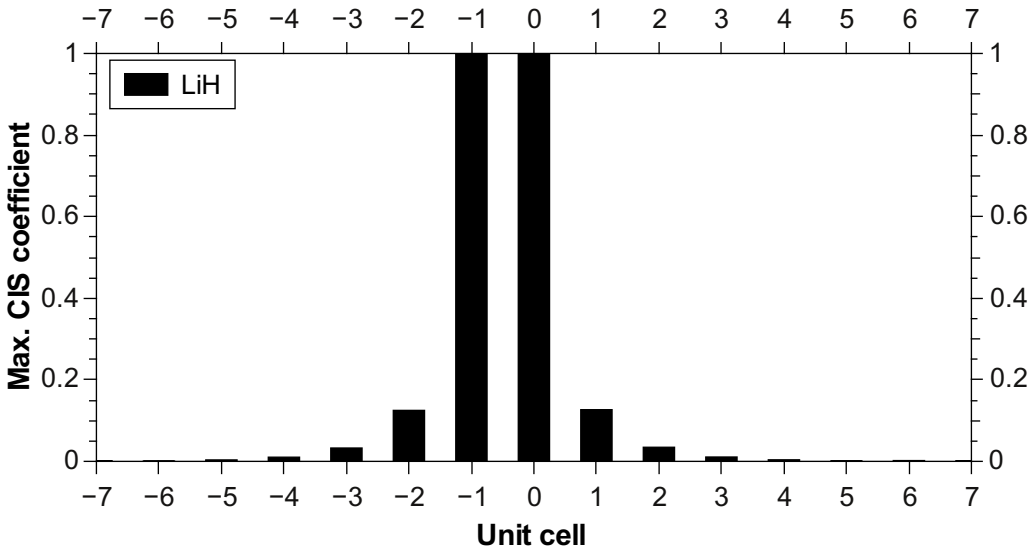

(i) LiH

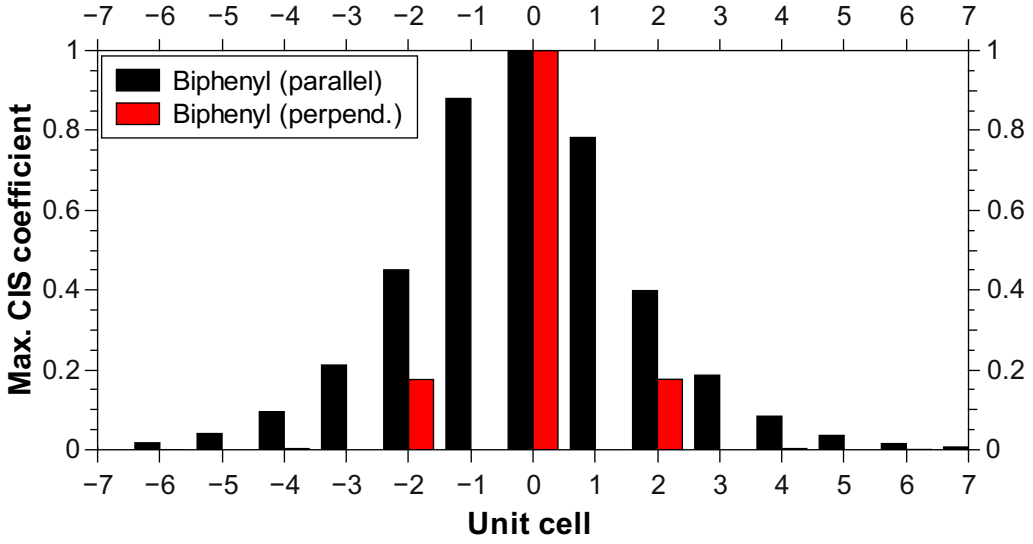

(ii) Biphenyl

Figure 2.2: Normed maximal CIS coefficients of (i) LiH and (ii) biphenyl per cell (singlet state)).

The local approach with non-orthogonal virtual states provides a very simple and useful indicator of the ability of the chosen **k**-mesh or the supercell to capture the studied exciton. As was shown in Sec. 2.3.2,

the direct space norm of the CIS vector can be different from unity. This difference, however, tends to zero when the values of the CIS vector at the edges of the supercell become small. Table 2.2 shows the convergence of the energies for the most diffuse exciton studied here with respect to the **k**-mesh size, together with the values of the direct space norm.

Table 2.2: Excitation energies for polybiphenyl (parallel) calculated with 6-31G (with upscaled exponent of the p-function of carbon) orbital basis set and VDZ fitting basis set, and the direct-space norm of the CIS vector.

	excitation energy / eV		norm of the CIS vector	
$n_{\mathbf{k}}$	ω_S	ω_T	singlet	triplet
5	3.7133	2.1438	0.98055	0.99319
6	3.7783	2.1745	0.98736	0.99562
7	3.8029	2.1828	0.99481	0.99869
8	3.8205	2.1886	0.99697	0.99923
9	3.8273	2.1904	0.99884	0.99978
10	3.8315	2.1914	0.99936	0.99987
11	3.8331	2.1918	0.99977	0.99997
12	3.8340	2.1919	0.99988	0.99998
13	3.8344	2.1920	0.99996	1.00000
14	3.8345	2.1920	0.99998	1.00000
15	3.8346	2.1921	0.99999	1.00000
16	3.8347	2.1921	1.00000	1.00000

Evidently the energy and the norm smoothly converge with the number of **k**-points. The norm gives a good estimate for the correctness of the description for a certain density of the **k**-mesh. Furthermore, judging on the value of the norm at a given **k**-point one can draw a conclusion about the diffuseness of the exciton under study. In Fig. 2.3 the dependence of the error in the direct space norm of singlet and triplet states for all the studied systems versus the number of the **k**-points is given. In all cases the norm

approaches unity more or less smoothly with the decay rate expressing the locality of the exciton.

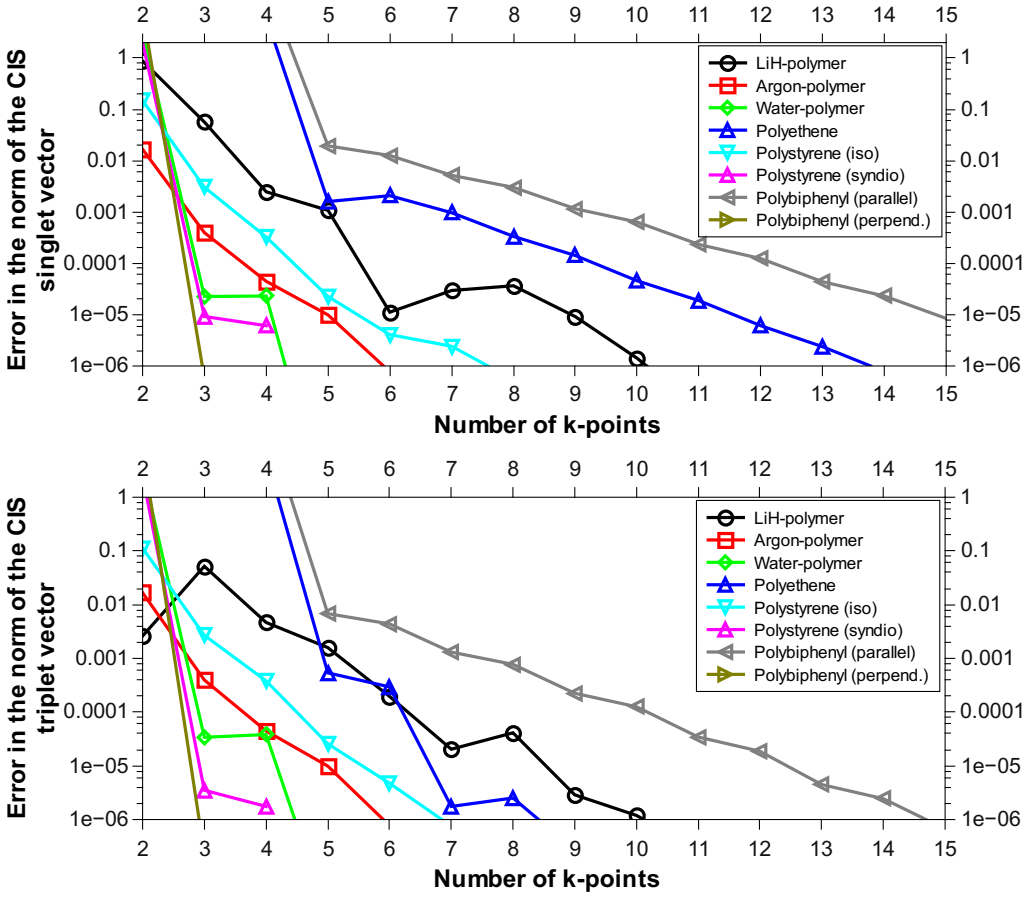

Figure 2.3: Errors in the direct space norm for singlet (top) and triplet (bottom) exciton state of different systems.

One of the approximations of the current scheme lies in the evaluation of the two-electron integrals via the density fitting technique. While this approximation is essential for the efficiency of the method, it is desirable that the effect on the accuracy of the results should be negligible. The periodic density fitting scheme in the ground state correlation calculations have been shown to cause errors in the energy of the order 10^{-5} Hartree per atom, [20] provided that the quality of the fitting basis set matches

that of the orbital basis set. In the present study we used orbital basis sets of the double-zeta quality. Table 2.3, which lists the energies, obtained employing fitting basis sets with increasing quality, shows that the density fitting errors are indeed tiny.

Table 2.3: Singlet/Triplet CIS excitation energies with the 6-31G** AO basis and fitting basis sets of different quality. GTO-fitting basis sets, optimized for MP2 calculations with cc-pVXZ orbitals basis sets and then converted to mixed PTO/GTO as explained in Ref. 20, are used and denoted as VXZ.

	ω_S / eV			ω_T / eV		
system	VDZ	VTZ	VQZ	VDZ	VTZ	VQZ
LiH	6.6060	6.6058	6.6060	5.5021	5.5018	5.5019
Ar	21.7344	21.7337	21.7339	20.5186	20.5177	20.5178
H_2O	10.3781	10.3792	10.3793	9.4848	9.4849	9.4848
C_2H_4	11.7476	11.7477	11.7477	10.5475	10.5475	10.5475

It is worth to mention that despite the presence the two-external 3-index integrals, which are absent in the MP2 method, the auxiliary basis sets optimized for MP2 seem to be perfectly applicable for CIS. We cannot compare our results directly to those obtained without the density fitting approximation, since the conventional 4-index integral generator has not been implemented. However, our method virtually exactly reproduces the results on the polyethylene reported in Ref. 52, obtained with the canonical non-density-fitted CIS method (see the supplementary material in Appendix A.1).

Finally we focus our attention on the influence of the starting CIS vector on the number of the Davidson iterations. As discussed in Sec. 2.3.5 the direct-space guesses have the advantage of the possibility to enforce the locality on the starting vector, but they suffer from having no (guess 1 and 2) or little (guess 3) information on the actual nature of the exciton. The reciprocal starting guess 4 on the contrary includes some knowledge on the

excitonic behaviour, but can be delocalized artificially. For the examples presented here the reciprocal space guess in fact turns out to be the most efficient. Guess 3, although including several starting vectors, rather than one, in most cases does not lead to any improvement even with respect to the guess 1 or 2.

Table 2.4: The number of iterations needed to calculate the lowest singlet exciton state using VDZ fitting basis set.

	number of iterations for guess			
system	1	2	3	4
LiH	15	15	5+7	11
Ar	15	15	5+7	10
H_2O	30	20	5+23	8
C_2H_4	31	32	5+31	11
styrene (iso)	21	18	5+27	14
styrene (syn)	37	38	5+35	12
biphenyl ($\parallel$)	20	16	5+23	9
biphenyl ($\perp$)	36	32	5+27	17

2.5 Conclusions

The periodic local density fitted CIS method presented in this contribution is the first step towards correlated optical band gaps described in the framework of local correlation methods. It explicitly includes the excitonic phenomenon, *i.e.*, the attraction between the hole and the electron. The screening effects due to electron correlation are, however, absent in this approach, which can lead to errors in the excitation energies of up to several eVs. A correlation treatment, which corrects this deficiency is planned to be added on top of CIS along the lines of the local correlation schemes, proven to be efficient for extended molecular systems. Indeed, for

molecular excited states, dominated by single excitations, the CIS method is known to usually provide a good description of the nature of the state, and is thus used as a starting point in correlated excited state treatment (like in TD-CC response theory). Besides, the ability of the periodic CIS method alone to provide a semi-quantitative theoretical description of the excitonic states makes this method useful also in its own right, due to a relative scarcity of inexpensive practical tools to study such states in the solid state computational science. Presently, the method is capable of treating Γ-point excitons in polymers with up to several dozens of atoms in the cell.

Chapter 3

Periodic DF local CIS method for solids

3.1 Introduction

Although the electronic band gap is one of the most important characteristic properties of crystalline systems, its rigorous theoretical description is difficult. Time-dependent density functional theory (TD-DFT), which is one of the most common techniques in molecular excited state studies, is hardly applicable for periodic systems. One of the intrinsic problems of DFT, the self-interaction error, artificially lowers the excitation energies of excited states with charge transfer character. In infinite systems this has extreme consequences: the lowest non-hybrid TD-DFT excitation energies are equal to the simple DFT HOCO-LUCO (highest occupied and lowest unoccupied crystalline orbital) orbital energy difference [52, 63]. An approach to excited states in periodic systems, based on the quasi-energy GW formalism [42, 86], is somewhat more successful. It provides a first-order correction to the Kohn-Sham (KS) orbital energies, and, if furthermore combined with solving the quasi-particle Bethe-Salpeter equation, includes the excitonic effects, *i.e.*, the electron-hole attraction (*a posteriori*). [42, 43, 58–62] Calculations employing these methods are, however,

computationally rather expensive.

The quantum chemical approach to the problem, *i.e.*, starting from a CIS wavefunction (containing excitonic effects *a priori*) und subsequently including correlation effects, which has been very successfully applied in countless molecular studies, is to a large extent unexplored for solids. Previous work in this context includes 1D-periodic implementations of the uncorrelated configuration interaction singles (CIS) method [52], and correlation corrections to it. [48,56] There are also examples of early applications of approximate CIS or time-dependent Hartree-Fock (TD-HF) techniques to simple 3D systems [52]. Recently, also a 3D-periodic semiempirical CIS implementation, based on the intermediate neglect of differential overlap approximation, has been reported [87]. There exists also a periodic implementation of the algebraic diagrammatic construction scheme for the self-energy in the canonical representation [88]. An alternative technique to evaluate the TD-HF excitation energies in periodic systems has been developed in Ref. 89. It implies fitting of the explicitly calculated values of the coupled perturbed HF polarizability to a model function, inversely dependent on frequency. The excitation energies are then evaluated as poles of this model function.

Finally, finite cluster approaches to excited states of periodic systems, based on the incremental scheme [36], or other fragment techniques, have been proposed [39, 90, 91]. However, the slow convergence with cluster size (depending on the character of the excited state) and the existence of parasitic cluster surface states renders such approaches as not straightforward.

The goal of our work is to develop a hierarchy of periodic quantum chemical excited state methods for solids. In Chapter 2 we have presented formalism, implementation, and test applications of a periodic local density fitted CIS method for 1D periodic systems like polymers. In the present work, the second paper in this series, the method is generalized to full 3D periodic systems (crystals). There are two fundamental complications com-

pared to 1D case. Firstly, the infinite lattice sums occurring in the Coulomb part of the matrix-vector product [92] no longer converge. Secondly, the direct space density fitting approach based on a single common fit-domain, as employed in the 1D case to calculate the exchange part of the matrix-vector product becomes prohibitively expensive for bulky systems. To remedy the first problem the Coulomb part is now calculated by employing an approach based on an approximate Ewald potential function [93], using multipole representations of the periodically repeated product densities beyond a certain distance. To fix the second problem a product-density specific local density fitting scheme in direct space with multiple different fit-domains is now used for the exchange part. In order for the fit to be robust, *i.e.*, to make the fitting error in the integrals second-order w.r. to the fitting error in the individual orbital product densities, the three-term formula for density fitting has to be used.

The paper is organized as follows: in the next section we briefly review the theory for periodic local CIS, and discuss the cyclic, and the Wigner-Seitz (WS) supercell truncated infinite models. Then, the calculation of the Coulomb and exchange parts of the matrix-vector product via Ewald, and local density fitting in direct space, respectively, are discussed. In Section III we briefly focus on some details of the implementation, relevant for accuracy and computational efficiency. In Section IV we present results from test calculations for different crystals, ranging from wide-gap insulators to semiconductors. The focus here is on the locality of the exciton in reciprocal and direct space. Section V finally concludes the paper.

3.2 Periodic local CIS theory

In the present paper we use the same convention for indices as in paper I: indices i, j, ... and a, b, ... denote Wannier functions (WFs) [23,78] ϕ_i, ϕ_j, ... and projected atomic orbitals (PAOs) [65,66,79,92] ϕ_a, ϕ_b, ..., respectively, or their Fourier images. WFs and PAOs are local orbitals spanning the

occupied and virtual spaces, respectively. For the corresponding canonical orbitals indices with an overbar are used. Indices P, Q, ... denote auxiliary fitting functions ϕ_P, ϕ_Q, ... and μ, ν, ... atomic orbitals (AOs) ϕ_μ, ϕ_ν, ... The calligraphic indices $\mathcal{I}$, $\mathcal{A}$, $\mathcal{P}$, $\mathcal{M}$, ... identify the lattice vectors $\mathbf{R}_\mathcal{I}$, $\mathbf{R}_\mathcal{A}$, $\mathbf{R}_\mathcal{P}$, $\mathbf{R}_\mathcal{M}$, ... of the cells, where the functions $\phi_{i\mathcal{I}}$, $\phi_{a\mathcal{A}}$, $\phi_{P\mathcal{P}}$, $\phi_{\mu\mathcal{M}}$, ..., respectively, are centered. Sums or differences between lattice vectors are denoted by $\oplus$ and $\ominus$ symbols, respectively, applied to the corresponding cell indices. Products of two orbitals are called product densities and designated by the symbol ρ, *e.g.* $\rho_{\mu\nu\mathcal{N}} = \phi_\mu\phi_{\nu\mathcal{N}}$. The atoms, the PAOs ϕ_a, ϕ_b, ... belong to, are denoted as A, B, ... Vectors $\mathbf{k}_i$, $\mathbf{k}_a$ and $\mathbf{k}_P$ are the wave-vectors of the first Brillouin zone (BZ) (*i.e.*, the so called **k**-vectors or **k**-points) corresponding to the occupied, virtual, or auxiliary functions. The chemical (Mulliken) notation is employed for the two-electron integrals.

The CIS wavefunction for a Γ-point exciton, as introduced in paper I, reads

$$\Psi^\Gamma_{\text{exc}} = \sum_{ia\mathcal{A}} c^i_{a\mathcal{A}} \sum_{\mathcal{I}} \Phi^{a(\mathcal{A}+\mathcal{I})}_{i\mathcal{I}} = \sum_{\bar{i}\bar{a}\mathbf{k}} c^{\bar{i}}_{\bar{a}}(\mathbf{k})\Phi^{\bar{a}}_{\bar{i}}(\mathbf{k}), \tag{3.1}$$

where **k** is the translational symmetry index of both the occupied and virtual canonical orbitals $\bar{i}$ and $\bar{a}$ (for the Γ-point excitons they have to coincide (*cf.* Eqs. (1.32) or (2.6)). $\Phi^{a(\mathcal{A}+\mathcal{I})}_{i\mathcal{I}}$ and $\Phi^{\bar{a}}_{\bar{i}}(\mathbf{k})$ are singly excited determinants in local and canonical space, respectively.

The CIS eigenvalue problem is solved by means of the Davidson diagonalization procedure [10], carried out in the canonical (reciprocal) space. The standard first-order update for the trial vector,

$$(\Delta\mathbf{c}^{(n)})^{\bar{i}}_{\bar{a}}(\mathbf{k}) = -\frac{(\mathbf{H}\mathbf{c}^{(n)})^{\bar{a}}_{\bar{i}}(\mathbf{k}) - \omega^{(n)}_{\text{CIS}}(\mathbf{c}^{(n)})^{\bar{i}}_{\bar{a}}(\mathbf{k})}{\varepsilon_{\bar{a}}(\mathbf{k}) - \varepsilon_{\bar{i}}(\mathbf{k}) - \omega^{(n)}_{\text{CIS}}}, \tag{3.2}$$

is used, with a subsequent orthogonalization to the previous-iteration trial vectors of the small Davidson space and normalization. Here, **H** stands for the CIS Hamiltonian, $\mathbf{c}^{(n)}$ and $\omega^{(n)}_{\text{CIS}}$ are the n-th iteration CIS vector and excitation energy, respectively, and the orbital energies at a certain **k**-point are denoted by $\varepsilon_{\bar{i}}(\mathbf{k})$ and $\varepsilon_{\bar{a}}(\mathbf{k})$.

The matrix-vector products $(\mathbf{Hc})_{\bar{i}}^{\bar{a}}(\mathbf{k})$ required to evaluate the small Davidson space Hamiltonian matrix [Eqs. (1.34) or (2.12)] and the residuum (here, **c** stands for a trial or full CIS vector) are partially calculated in canonical and partially in local space,

$$\begin{aligned}(\mathbf{Hc})_{\bar{i}}^{\bar{a}}(\mathbf{k}) = &\Big(\varepsilon_{\bar{a}}(\mathbf{k}) - \varepsilon_{\bar{i}}(\mathbf{k})\Big)c_{\bar{a}}^{\bar{i}}(\mathbf{k}) \\ &+ \mathcal{FT}_{\mathbf{R}_{\mathcal{A}}}\Big\{2\sum_{j\mathcal{J}b\mathcal{B}}(i\,a\mathcal{A}|j\mathcal{J}\,b\mathcal{B})c_{b\mathcal{B}}^{j\mathcal{J}} \\ &- \sum_{j\mathcal{J}b\mathcal{B}}(i\,j\mathcal{J}|a\mathcal{A}\,b\mathcal{B})c_{b\mathcal{B}}^{j\mathcal{J}}\Big\},\end{aligned} \tag{3.3}$$

where $\mathcal{FT}_{\mathbf{R}_{\mathcal{A}}}$ denotes the Fourier transformation with respect to the vector $\mathbf{R}_{\mathcal{A}}$.

The two-electron part **Vc** of the CIS matrix-vector product **Hc** = **Fc** + **Vc** consists of the so called Coulomb term (which describes the exciton-exciton interaction and vanishes for a triplet state)

$$({}^{\mathrm{coul}}\mathbf{Vc})_i^{a\mathcal{A}} = \sum_{j\mathcal{J}b\mathcal{B}}(i\,a\mathcal{A}|j\mathcal{J}\,b\mathcal{B})c_{b\mathcal{B}}^{j\mathcal{J}} \tag{3.4}$$

and the exchange term (which describes the electron-hole attraction)

$$({}^{\mathrm{exch}}\mathbf{Vc})_i^{a\mathcal{A}} = \sum_{j\mathcal{J}b\mathcal{B}}(i\,j\mathcal{J}|a\mathcal{A}\,b\mathcal{B})c_{b\mathcal{B}}^{j\mathcal{J}}. \tag{3.5}$$

These contractions are calculated with robust density fitting, which factorizes the four-index electron repulsion integrals (ERIs) into three- and two-index objects. [6, 16, 20, 72, 74, 94–97] Different decay behaviour of the lattice summations in Eqs. (3.4) and (3.5) lead to two principally different density fitting approaches. The Coulomb term Eq. (3.4), involving long-range summations, is fitted in the reciprocal space, while the relatively short-range exchange term Eq. (3.5) (governed by the locality of the exciton) is fitted in the direct space (*vide infra*). [92]

3.2.1 Cyclic model versus Wigner-Seitz supercell truncated infinite model of a crystal

The cell index $\mathcal{A}$ in the direct representation of the CIS coefficients $c^i_{a\mathcal{A}}$ in Eq. (3.1) or the matrix-vector products $(\mathbf{Vc})^{a\mathcal{A}}_i$ in Eqs. (3.4) or (3.5) formally runs to infinity. For obvious reasons, however, it is not possible to treat a crystal as an infinite object in practical calculations. Fortunately, locality of the exciton can effectively truncate the essential range for this index, which does not need to extend further than the exciton to be captured.

In Chapter 2 a *cyclic* model for a crystal, *i.e.*, a finite model with Born-von Karman periodic boundary conditions, was considered. Such a model features a finite number of **k**-points in the reciprocal space representation of the wave function (3.1), equal to the number of unit cells $\mathcal{A}$ in the supercell of the cyclic system [27,92,98]. The transformations between the direct and reciprocal spaces correspond in this case to the discrete Fourier and inverse-Fourier transforms [*e.g.*, in Eq. (3.3)]. The convergence of the excitation energies w.r. to the supercell size was explored in Chapter 2 by increasing the supercell size, and, with that, the density of the **k**-mesh.

Yet, in the *infinite* model of a crystal the direct space representation of *e.g.* the CIS-coefficients are, in fact, the coefficients of an infinite Fourier-series expansion of the reciprocal space CIS-coefficients $c^i_a(\mathbf{k})$, which are a *continuous* and *periodic* functions of the variable **k**,

$$c^i_a(\mathbf{k}) = \sum_{\mathcal{A}} c^i_{a\mathcal{A}} \exp(\imath \mathbf{k} \cdot \mathbf{R}_{\mathcal{A}}). \tag{3.6}$$

The Fourier-coefficients $c^i_{a\mathcal{A}}$ in turn are defined as integrals over the period in the **k**-space, *i.e.*, the BZ,

$$c^i_{a\mathcal{A}} = \int_{\mathrm{BZ}} \mathrm{d}\mathbf{k}\, c^i_a(\mathbf{k}) \exp(-\imath \mathbf{k} \cdot \mathbf{R}_{\mathcal{A}}). \tag{3.7}$$

The same holds for the matrix-vector products $(\mathbf{Vc})^a_i(\mathbf{k})$.

Starting from this model, an approximation can be introduced in Eq. (3.6), which restricts the number of the terms in the Fourier series, without

affecting the expression for the Fourier coefficients (3.7). In practice, of course, the integration (3.7) has to be performed numerically using a large, but finite number of **k**-points. But importantly, the density of the **k**-mesh, used for the integral quadrature, is now effectively decoupled from the number of the direct space vectors used in the finite summation (3.6). The truncation of the Fourier series is done in our approach by restricting the index $\mathcal{A}$ to a supercell, chosen in the WS form. For each CIS coefficient $c^i_{a\mathcal{A}}$ or matrix-vector product $(\mathbf{Vc})^{a\mathcal{A}}_i$ the origin of the WS supercell is chosen to coincide with centering point of the WF ϕ_i. With this definition the most rapid convergence of the truncated Fourier series to the untruncated result is expected, since for each i the truncating surface, *i.e.*, the border of the Wigner-Seitz supercell, is as distant and as spherical-like as possible. Furthermore, since the Wigner-Seitz supercell is invariant with respect to the point group symmetry of the crystal the symmetry of the exciton is not compromised by the truncation. For future reference we denote this model as the Wigner-Seitz supercell truncated infinite model (WSS-TIM) of a crystal as an alternative to the cyclic model.

For the CIS method for polymers reported in Chapter 2 very large supercells could be used without a considerable penalty in the computational time. Therefore, the number of unit cells in the supercell was set to be equal to the number of **k**-vectors in the mesh, *i.e.*, the cyclic model was always employed. In bulky systems the situation is, however, different. Expansion of a 3D supercell is very costly due to the cubic increase of the number of unit cells (and the ERIs to be computed) with linear increase in the supercell size. Therefore, in our approach, where the computational demands for the reciprocal space part of the calculation [Eqs. (3.2) and (3.3)] are negligible compared to that of the direct space (*vide infra*), at least for small and medium sized unit cells, WSS-TIM is clearly advantageous.

From the angle of WSS-TIM, the cyclic model for not yet converged results suffers from two independent sources of errors, (i) the inaccurate quadrature for the **k**-point integration (3.7), and (ii) the truncation of the

Fourier series (3.6). The integration over the BZ (3.7) in our case can be performed very accurately, employing very dense **k**-meshes, and hence, eliminating one (and, as the calculations show, *cf.* Sec. 3.4.3, the main) of these two deficiencies. This substantially speeds up the convergence of the results with respect to the $\mathcal{A}$-truncation range, which in WSS-TIM is the only remaining approximation.

3.2.2 Density fitting for the Coulomb term

As was shown in Ref. [92], evaluation of the Coulomb term Eq. (3.4) simplifies considerably within the reciprocal-space density fitting procedure. The orthogonality relations for the irreps of the translational symmetry group (represented by the **k**-vectors) eliminate all but the $\mathbf{k}_P$=0 term from the $\mathbf{k}_P$-summation (integration) of the back-Fourier transform [73, 74, 92], yielding

$$({}^{\text{coul}}\mathbf{Vc})_i^{a\mathcal{A}} = \sum_P (i\, a\mathcal{A}|P)^*_{(\mathbf{k}_P=0)} \sum_{j\, b\mathcal{B}'} d^{j\, b\mathcal{B}'}_{P\ (\mathbf{k}_P=0)} c^j_{b\mathcal{B}'}, \tag{3.8}$$

where $(i\, a\mathcal{A}|P)_{(\mathbf{k}_P)}$ and $d^{j\, b\mathcal{B}'}_{P\ (\mathbf{k}_P)}$ are the Fourier images of the 3-index Coulomb integrals and density fitting coefficients, respectively, and the vector $\mathcal{B}'$ is defined as $\mathcal{B} \ominus \mathcal{J}$. The DF coefficients, which correspond to the minimum of the fitting functional with the Coulomb metric, are evaluated also in the reciprocal space [92] as

$$d^{j\, b\mathcal{B}'}_{P\ (\mathbf{k}_P)} = \sum_Q (j\, b\mathcal{B}'|Q)_{(\mathbf{k}_P)} ([J_{(\mathbf{k}_P)}]^{-1})_{QP}, \tag{3.9}$$

whereas the 3-index integrals are calculated in the direct space and Fourier-transformed thereafter,

$$(i\, a\mathcal{A}|P)_{(\mathbf{k}_P=0)} = \sum_{\mathcal{P}} (i\, a\mathcal{A}|P\mathcal{P}). \tag{3.10}$$

The same applies also to the two-index metric matrix, the inverse of which is occurring in Eq. (3.9); it is the reciprocal image of the 2-index Coulomb

integral,

$$(J_{(\mathbf{k}_P=0)})_{QP} = (Q|P)_{(\mathbf{k}_P=0)} = \sum_{\mathcal{P}} (Q|P\mathcal{P}). \tag{3.11}$$

As is seen from Eqs. (3.10) and (3.11), evaluation of both the three-index $(i\,a\mathcal{A}|P)_{(\mathbf{k}_P=0)}$ and two-index $(Q|P)_{(\mathbf{k}_P=0)}$ reciprocal images of the Coulomb integrals imply non-convergent infinite lattice summations in the 3D case. This non-convergence issue is not a feature of the reciprocal space density fitting formalism, but reflects the true physics of the Coulomb CIS term (3.4), which indeed is of long-range nature.

Due to the mutual orthogonality of the occupied and virtual spaces, the interacting $ia\mathcal{A}$-product densities are chargeless. This guarantees that the lattice sum (3.4) of the Coulomb term is convergent, although only conditionally. *s*-type fitting functions, on the other hand, are not chargeless, which would lead to divergent summations (3.10) and (3.11). A remedy to this problem is the use of mixed auxiliary basis sets, containing Poisson-type-orbitals (PTOs), together with a few GTOs. The use of PTOs as a fitting basis [17–20] allows for a stable scheme, which does not involve any charge-multipole interactions. The PTOs, which are Laplacians of standard GTOs, are free of moments of any order. This property leads to an exponential decay of the Coulomb integrals, and therefore to a fast decay of the lattice sums (3.10) and (3.11). PTOs however must be complemented by a few GTOs in order to fully represent real product densities, which are not momentless. It is, in fact, sufficient to introduce just one GTO of each angular momentum per center. Since, as discussed above, $ia\mathcal{A}$-product densities are chargeless, the troublesome *s*-type GTOs are not needed.

The convergence of the lattice sums involving GTO-fitting functions (especially the *p*-GTOs) in 3D still remains an issue. Note that the use of a combined PTO-GTO fitting basis implies that for the main PTO-part of the fitting basis the lattice sums (3.10) and (3.11) converge exponentially [67]. Nevertheless, for the smaller GTO-part of the fitting basis the summations (3.10) and (3.11) converge either very slowly or even only conditionally and thus convergence acceleration techniques like the Ewald procedure

are needed.

The value, to which a conditionally convergent series converges, depends on the chosen order of summation. For Coulomb lattice sums this mathematical uncertainty in an infinite lattice reflects the strong dependence of the electrostatic potential on the particular shape of real finite crystals. The Ewald-type summation of the conditionally convergent series effectively corresponds to a specific choice of the summation order, each partial sum of which corresponds to zeroing the charge, dipole, and quadrupole moments of the unit cell, canceling thus the not absolutely convergent contributions. [99] Formally, this is equivalent to a substitution of the conditionally convergent Coulomb potential [Eq. (18) of Ref. 93] by an Ewald potential [Eqs. (43) and (44) of Ref. 93], which consists of two absolutely convergent sums. The Ewald technique dates back to more than 90 years [100], and different formulations of it have been proposed over the years. [99] Here we adopt an implementation used in the CRYSTAL program to compute the Coulomb part of the Fock matrix in HF or DFT calculations. [93, 101]

In the present context the Ewald procedure is utilized for calculating the three-index integrals in the AO basis,

$$\begin{aligned}(\mu\nu\mathcal{N}|P)_{(\mathbf{k}_P=0)} &= \sum_{\mathcal{P}}(\mu\nu\mathcal{N}|P\mathcal{P}) \\ &= \sum_{\mathcal{P}}(\mu(\ominus\mathcal{P})\nu(\mathcal{N}\ominus\mathcal{P})|P).\end{aligned} \tag{3.12}$$

Evaluation of such an integral proceeds via three quantities,

$$(\mu\nu\mathcal{N}|P)_{(\mathbf{k}_P=0)} = {}^{\mathrm{Ew}}\Theta^{P}_{\mu\nu\mathcal{N}} - \delta\Theta^{P}_{\mu\nu\mathcal{N}}(\{\mathcal{P}\}_{\mathrm{pen}}) + \delta K^{P}_{\mu\nu\mathcal{N}}(\{\mathcal{P}\}_{\mathrm{pen}}), \tag{3.13}$$

which are defined in the following.

The first term ${}^{\mathrm{Ew}}\Theta^{P}_{\mu\nu\mathcal{N}}$ is the contribution originating from the Ewald potential

$${}^{\mathrm{Ew}}\Phi_{\mu\nu\mathcal{N}}(\mathbf{r}) = \int \mathrm{d}\mathbf{r}'\,\rho_{\mu\nu\mathcal{N}}(\mathbf{r}')A(\mathbf{r}'-\mathbf{r}), \tag{3.14}$$

of an infinite lattice, generated by the periodic images of the AO product densities $\rho_{\mu\nu\mathcal{N}}$. Here, $A(\mathbf{r})$ is the Ewald potential function, defined in Eq. (44) of Ref. 93, which consists of two absolutely convergent series, one with respect to the direct space vectors, the other with respect to the reciprocal space vectors. The interaction between the lattice of the periodically repeated densities $\rho_{\mu\nu\mathcal{N}}$ and the fitting function ϕ_P is evaluated by invoking the multipole representation of the latter with the multipole moments η_P^{ml} of the angular momentum l and its projection m,

$$^{\mathrm{Ew}}\Theta^P_{\mu\nu\mathcal{N}} = {}^{\mathrm{Ew}}\Phi_{\mu\nu\mathcal{N}}(\mathbf{r}_P)\sum_{l=0}^{l_{max}}\sum_{m=-l}^{l} Z^{ml}(\mathbf{r}_P)\eta_P^{ml}(\mathbf{r}_P). \tag{3.15}$$

Here, $\mathbf{r}_P$ is the position vector of the center of the fitting function ϕ_P, and $Z^{ml}(\mathbf{r})$ denotes the renormalized solid harmonics, corresponding to the angular momentum l and m (Eqs. (97) and (98) of Ref. 93). The expression (3.15) utilizes the fact, that the fitting GTOs do not possess charge (*vide supra*), and thus their spheropole [93] is zero.

The second and third terms of (3.13) provide a correction to the Ewald potential in the region around the fitting function ϕ_P, where it overlaps with the (periodically repeated) densities $\rho_{\mu\nu\mathcal{N}}$, rendering the multipole representation of the former as invalid. This region (or cavity) is determined on the basis of the overlap between the most diffuse Gaussians of $\phi_{\mu(\ominus\mathcal{P})}$, $\phi_{\nu(\mathcal{N}\ominus\mathcal{P})}$, and ϕ_P as a subset $\{\mathcal{P}\}_{\mathrm{pen}}$ of $\mathcal{P}$-vectors. The densities $\rho_{\mu(\ominus\mathcal{P})\nu(\mathcal{N}\ominus\mathcal{P})}$ with $\mathcal{P} \in \{\mathcal{P}\}_{\mathrm{pen}}$ hence can significantly penetrate the fitting functions ϕ_P. By default, a threshold of 10^{-9} is used for the overlap criterion defining this cavity. The quantities $\delta\Theta^P_{\mu\nu\mathcal{N}}(\{\mathcal{P}\}_{\mathrm{pen}})$ and $\delta K^P_{\mu\nu\mathcal{N}}(\{\mathcal{P}\}_{\mathrm{pen}})$ are calculated within this cavity as

$$\begin{aligned}\delta\Theta^P_{\mu\nu\mathcal{N}}(\{\mathcal{P}\}_{\mathrm{pen}}) = &\sum_{\mathcal{P}\in\{\mathcal{P}\}_{\mathrm{pen}}}\left[\int \mathrm{d}\mathbf{r}\frac{\rho_{\mu\nu\mathcal{N}}(\mathbf{r})}{|\mathbf{r}-\mathbf{R}_{\mathcal{P}}-\mathbf{r}_P|}\right]\\ &\times\sum_{l=0}^{l_{max}}\sum_{m=-l}^{l} Z^{ml}(\mathbf{r}_P)\eta_P^{ml}(\mathbf{r}_P),\end{aligned} \tag{3.16}$$

and

$$\delta K^{P}_{\mu\nu\mathcal{N}}(\{\mathcal{P}\}_{\text{pen}}) = \sum_{\mathcal{P}\in\{\mathcal{P}\}_{\text{pen}}} (\mu(\ominus\mathcal{P})\nu(\mathcal{N}\ominus\mathcal{P})|P) = \sum_{\mathcal{P}\in\{\mathcal{P}\}_{\text{pen}}} (\mu\nu\mathcal{N}|P\mathcal{P}). \tag{3.17}$$

The term (3.16) subtracts from the integral (3.15) the contribution from the cavity $\{\mathcal{P}\}_{\text{pen}}$, treated at the point-multipole level. This contribution is then recalculated explicitly in (3.17), *i.e.*, without the multipole approximation, and added to the integral $(\mu\nu\mathcal{N}|P)_{(\mathbf{k}_P=0)}$.

After calculating the three-index integrals (3.12) in AO basis they are transformed to WF/PAO basis, yielding the transformed three-index integrals of Eq. (3.10), as required in Eq. (3.8),

$$(ia\mathcal{A}|P)_{(\mathbf{k}_P=0)} = \sum_{\nu\mathcal{N}} C_{\nu(\mathcal{N}\ominus\mathcal{A}),a} \times \sum_{\mu\mathcal{M}} C_{\mu\mathcal{M},i}(\mu\nu(\mathcal{N}\ominus\mathcal{M})|P)_{(\mathbf{k}_P=0)}. \tag{3.18}$$

Here, $C_{\nu(\mathcal{N}\ominus\mathcal{A}),a} = C_{\nu\mathcal{N},a\mathcal{A}}$ and $C_{\mu\mathcal{M},i}$ are the LCAO coefficients of the WF ϕ_i, and the PAO $\phi_{a\mathcal{A}}$, respectively.

The two-index integrals (3.11) are treated analogously, with the sole difference that instead of the orbital product density $\rho_{\mu\nu\mathcal{N}}$ an auxiliary function ϕ_Q enters, and an AO to MO transformation (3.18) is obviously not needed. To evaluate the objects ${}^{\text{Ew}}\Theta^{P}_{\mu\nu\mathcal{N}}$ and $\delta\Theta^{P}_{\mu\nu\mathcal{N}}(\{\mathcal{P}\}_{\text{pen}})$ already existing CRYSTAL routines, adapted for the current purpose, are employed. [93,102]

3.2.3 Density fitting for the exchange term

The ERIs occurring in the Coulomb (3.4) and exchange (3.5) terms are different. In the latter, the orbital product distributions of the ERIs in the latter generally are not chargeless. This, in turn, requires *s*-type GTOs to be included in the fitting basis sets. The reciprocal-space fit for such integrals then indeed becomes problematic due to divergent lattice sums

for three-index integrals involving s-GTO fitting functions. However, the actual lattice summations of (3.5) do not go to infinity, but are effectively truncated by the locality of the CIS coefficients. In our approach, where the direct space images of the CIS vectors are obtained by the back-Fourier-transform, [92] their locality is enforced by restricting the lattice vector $\mathbf{R}_{\mathcal{A}}$ to the Wigner-Seitz supercell (*cf.* Sec. 3.3). Since no long-range lattice summations are required, the local density-fitting scheme in direct space, is more appropriate for the exchange term.

In Sec. 2.2.5 a local-density fitting approach with a single, common, and sufficiently large fit-domain D was employed (*cf.* Eqs. (2.45) and (2.46)),

$$({}^{\text{exch}}\mathbf{Vc}) = \sum_{j\mathcal{J}b\mathcal{B}} \sum_{P\mathcal{P}\in D} d^{ij\mathcal{J}}_{P\mathcal{P}} (P\mathcal{P}|a\mathcal{A}b\mathcal{B}) c^{j\mathcal{J}}_{b\mathcal{B}}, \tag{3.19}$$

with the DF-coefficients

$$d^{i\,j\mathcal{J}}_{P\mathcal{P}} = \sum_{Q\mathcal{Q}\in D} (i\; j\mathcal{J}|Q\mathcal{Q})([J^D]^{-1})_{Q\mathcal{Q}\,P\mathcal{P}}. \tag{3.20}$$

Here, $J^D_{Q\mathcal{Q}\,P\mathcal{P}}$ is defined as the 2-index Coulomb metric matrix within the fit-domain D, *i.e.* $(P\mathcal{P}|Q\mathcal{Q})\big|_{(P\mathcal{P},Q\mathcal{Q})\in D}$. Such an approach has certain advantages: (i) robust fitting [8,9] is achieved with just the one- rather than the three-term formula (two of the terms in the latter cancel); (ii) only one inversion of the metric matrix in Eq. (3.20) needs to be computed, and (iii) its implementation, even when exploiting translational symmetry, is not too complicated. On the other hand, the common fit-domain D must be large enough to support all possible $ij\mathcal{J}$- or $a\mathcal{A}b\mathcal{B}$ orbital product distributions in the ERIs of Eq. (3.5). Consequently, D needs to be somewhat larger (due to $\mathcal{B}$) than the whole Wigner-Seitz supercell, to which the index $\mathcal{A}$ is restricted (*vide infra*). For the 1D polymers this is not problematic, but for 2D slabs, and especially 3D crystals, D would become prohibitively large.

To solve this problem we have implemented a robust three-term local

density fitting scheme with product-density-specific fit-domains, *i.e.*,

$$
\begin{aligned}
({}^{\mathrm{exch}}\mathbf{Vc})_i^{a\mathcal{A}} = & \sum_{j\mathcal{J}b\mathcal{B}} \sum_{P\mathcal{P}\in[ij\mathcal{J}]} d_{P\mathcal{P}}^{ij\mathcal{J}} (P\mathcal{P}|a\mathcal{A}b\mathcal{B}) c_{b\mathcal{B}}^{j\mathcal{J}} \\
& + \sum_{j\mathcal{J}b\mathcal{B}} \sum_{P\mathcal{P}\in[a\mathcal{A}b\mathcal{B}]} (ij\mathcal{J}|P\mathcal{P}) d_{P\mathcal{P}}^{a\mathcal{A}b\mathcal{B}} c_{b\mathcal{B}}^{j\mathcal{J}} \\
& - \sum_{j\mathcal{J}b\mathcal{B}} \sum_{P\mathcal{P}\in[ij\mathcal{J}]} \sum_{Q\mathcal{Q}\in[a\mathcal{A}b\mathcal{B}]} d_{P\mathcal{P}}^{ij\mathcal{J}} (P\mathcal{P}|Q\mathcal{Q}) d_{Q\mathcal{Q}}^{a\mathcal{A}b\mathcal{B}} c_{b\mathcal{B}}^{j\mathcal{J}},
\end{aligned}
\tag{3.21}
$$

with the two-internal DF coefficients

$$
d_{P\mathcal{P}}^{i\,j\mathcal{J}} = \sum_{Q\mathcal{Q}\in[ij\mathcal{J}]} (i\;j\mathcal{J}|Q\mathcal{Q}) ([J^{[ij\mathcal{J}]}]^{-1})_{Q\mathcal{Q}\,P\mathcal{P}} \tag{3.22}
$$

and the two-external DF coefficients

$$
d_{P\mathcal{P}}^{a\mathcal{A}b\mathcal{B}} = \sum_{Q\mathcal{Q}\in[a\mathcal{A}b\mathcal{B}]} (a\mathcal{A}\;b\mathcal{B}|Q\mathcal{Q}) ([J^{[a\mathcal{A}b\mathcal{B}]}]^{-1})_{Q\mathcal{Q}\,P\mathcal{P}}. \tag{3.23}
$$

In Eqs. (3.21)-(3.23) the summations over auxiliary functions and the dimensions of the metric matrices are restricted to $ij\mathcal{J}$- or $a\mathcal{A}b\mathcal{B}$-density specific fit-domains, denoted as $[ij\mathcal{J}]$, or $[a\mathcal{A}b\mathcal{B}]$, respectively. The (multiple) metric matrices to be inverted (for each $ij\mathcal{J}$- and $a\mathcal{A}b\mathcal{B}$-density) thus are quite small. As demonstrated below in Sec. 3.4 high accuracy in the fit is already achieved with just a few atoms per fit domain.

By exploiting the translational symmetry the above expressions simplify. For example, the expression for the 2-external DF coefficients (3.23) can be rewritten as

$$
d_{P\mathcal{P}''}^{ab\mathcal{B}''} = \sum_{Q\mathcal{Q}''\in[ab\mathcal{B}'']} (a\;b\mathcal{B}''|Q\mathcal{Q}'') ([J^{[ab\mathcal{B}'']}]^{-1})_{Q\mathcal{Q}''\,P\mathcal{P}''}, \tag{3.24}
$$

with $\mathcal{B}'' = \mathcal{B} \ominus \mathcal{A}$, $\mathcal{P}'' = \mathcal{P} \ominus \mathcal{A}$, and $\mathcal{Q}'' = \mathcal{Q} \ominus \mathcal{A}$.

First and second terms of Eq. (3.21) can be treated similarly. The first

term then reads as

$$\sum_{j\mathcal{J}b\mathcal{B}} \sum_{P\mathcal{P}\in[ij\mathcal{J}]} d^{ij\mathcal{J}}_{P\mathcal{P}}(P\mathcal{P}|a\mathcal{A}b\mathcal{B})c^{j\mathcal{J}}_{b\mathcal{B}} = \sum_{P\mathcal{P}\in[ij\mathcal{J}]} \sum_{j\mathcal{J}} d^{i\,j\mathcal{J}}_{P\mathcal{P}} \sum_{b\mathcal{B}'} c^{j}_{b\mathcal{B}'} \times\Big(P(\mathcal{P}\ominus\mathcal{A})|a\; b(\mathcal{B}'\ominus\mathcal{A}\oplus\mathcal{J})\Big). \tag{3.25}$$

with $\mathcal{B}' = \mathcal{B}\ominus\mathcal{J}$. The second term can be recast as

$$\sum_{j\mathcal{J}b\mathcal{B}} \sum_{P\mathcal{P}\in[a\mathcal{A}b\mathcal{B}]} (ij\mathcal{J}|P\mathcal{P})d^{a\mathcal{A}b\mathcal{B}}_{P\mathcal{P}} c^{j\mathcal{J}}_{b\mathcal{B}} = \sum_{P\mathcal{P}''\in[ab\mathcal{B}'']} \sum_{j\mathcal{J}} \Big(ij\mathcal{J}|P(\mathcal{P}''\oplus\mathcal{A})\Big) \sum_{b\mathcal{B}''} d^{ab\mathcal{B}''}_{P\mathcal{P}''} c^{j}_{b(\mathcal{B}''\oplus\mathcal{A}\ominus\mathcal{J})}. \tag{3.26}$$

Finally, the third term of Eq. (3.21) can be rewritten as

$$\sum_{j\mathcal{J}b\mathcal{B}} \sum_{P\mathcal{P}\in[ij\mathcal{J}]} \sum_{Q\mathcal{Q}\in[a\mathcal{A}b\mathcal{B}]} d^{ij\mathcal{J}}_{P\mathcal{P}}(P\mathcal{P}|Q\mathcal{Q})d^{a\mathcal{A}b\mathcal{B}}_{Q\mathcal{Q}} c^{j\mathcal{J}}_{b\mathcal{B}} = \sum_{j\mathcal{J}} \sum_{P\mathcal{P}\in[ij\mathcal{J}]} d^{i\,j\mathcal{J}}_{P\mathcal{P}} \sum_{b\mathcal{B}''} c^{j}_{b(\mathcal{B}''\oplus\mathcal{A}\ominus\mathcal{J})} \times \sum_{Q\mathcal{Q}''\in[ab\mathcal{B}'']} (P(\mathcal{P}\ominus\mathcal{A})|Q\mathcal{Q}'')d^{ab\mathcal{B}''}_{Q\mathcal{Q}''}. \tag{3.27}$$

The contraction of the two-index integrals $(P(\mathcal{P}\ominus\mathcal{A})|Q\mathcal{Q}'')$ with the two-external DF coefficients $d^{ab\mathcal{B}''}_{Q\mathcal{Q}''}$ in Eq. (3.27) leads to an object which has exactly the same structure as the two-external integrals $(P(\mathcal{P}\ominus\mathcal{A})|a\; b(\mathcal{B}'\ominus\mathcal{A}\oplus\mathcal{J}))$ of the first term, Eq. (3.25) (note that $\mathcal{B}'\ominus\mathcal{A}\oplus\mathcal{J} = \mathcal{B}''$). Since the remaining contractions are identical for the first and the third term, this object can simply be added to the two-external integrals of the first term, calculating first and third term contributions to $({}^{\text{exch}}\mathbf{Vc})^{a\mathcal{A}}_{i}$ in one sweep.

Similarly to the Coulomb term, the 4-index integrals of Eq. (3.5) are never assembled (this would nominally scale as $O(N^5)$). Instead, the CIS coefficients are first contracted with the two-external 3-index integrals [first term, Eq. (3.25)] or DF coefficients [second term, Eq. (3.26)] . The results of these contractions are directly assembled to the **Vc** matrix-vector products. Both procedures have a nominal scaling of $O(N^4)$.

Evidently, only translationally irreducible sets of 3- or 2-index objects (*i.e.* those with the first index belonging to the reference cell) are to be evaluated and explicitly kept. However, these objects are to be correctly translated in the contractions, which leads to a somewhat complicated bookkeeping. Furthermore, note that the calculation of the fitting coefficients Eq. (3.24) does not involve any translations by $\mathbf{R}_{\mathcal{A}}$. On the other hand, for the assembly of the matrix-vector product $({}^{\text{exch}}\mathbf{Vc})_i^{a\mathcal{A}}$ such translation vectors do occur in the two-external, and two-internal integrals of Eqs. (3.25) and (3.26), respectively. This implies that these integral distributions, primarily the two-external one, are rather large, since $\mathbf{R}_{\mathcal{A}}$ runs over the whole Wigner-Seitz supercell (*vide infra*).

3.3 Implementation remarks

First of all, we note that in the direct space part of the calculations the translational symmetry is fully exploited (point group symmetry is not yet utilized). This implies that only translationally irreducible direct-space objects, where the first index is restricted to the zero cell, are computed, stored, or read from disk. In contractions involving objects with the first index outside the zero cell, their translationally equivalent counterparts are found and processed instead.

As discussed in the previous section, the three-term density fitting scheme used for calculating the exchange term (*cf.* Sec. 3.2.3), employs local fit-domains $[ij\mathcal{J}]$ and $[ab\mathcal{B}'']$, specific for each product-density $\rho_{ij\mathcal{J}}$ and $\rho_{ab\mathcal{B}''}$. The fit-domains represent a set of fitting functions, centered on several atoms, such that they provide sufficient support for the densities to be fitted. The fit domains are constructed by using a similar technique as proposed in Ref. 20: for a WF-pair $\phi_i\phi_{j\mathcal{J}}$, or a pair of PAO-atoms $AB\mathcal{B}''$ a quasi-population $q_{D\mathcal{D}}^{ij\mathcal{J}}$, or $q_{D\mathcal{D}}^{AB\mathcal{B}''}$ of the associated product densities on an

atom $D\mathcal{D}$ is defined as

$$q_{D\mathcal{D}}^{ij\mathcal{J}} = \sum_{\mu\mathcal{M}\in D\mathcal{D}} [1 + P(i, j\mathcal{J})] \times \left(C_{\mu\mathcal{M}i} \sum_{\nu\mathcal{N}\in D\mathcal{D}} S_{\mu\mathcal{M}\nu\mathcal{N}} C_{\nu\mathcal{N}j\mathcal{J}} \right)^2, \tag{3.28}$$

or

$$q_{D\mathcal{D}}^{AB\mathcal{B}''} = \sum_{a\in A} \sum_{b\in B\mathcal{B}''} \left[\sum_{\mu\mathcal{M}\in D\mathcal{D}} [1 + P(a, b\mathcal{B}'')] \times \left(C_{\mu\mathcal{M},a} \sum_{\nu\mathcal{N}\in D\mathcal{D}} S_{\mu\mathcal{M}\nu\mathcal{N}} C_{\nu\mathcal{N},b\mathcal{B}''} \right)^2 \right], \tag{3.29}$$

respectively. Here $C_{\nu\mathcal{N},j\mathcal{J}}$ an $C_{\nu\mathcal{N},b\mathcal{B}''}$ are the LCAO coefficients of the WF $j\mathcal{J}$ and PAO $b\mathcal{B}''$, respectively, $\mathbf{S}$ is the AO overlap matrix, and P is an index permutation operator. Each fit-domain comprises a predefined number N_D of atoms $D\mathcal{D}$ with the highest populations $q_{D\mathcal{D}}$. For all PAO pairs $ab\mathcal{B}''$ belonging to a common pair of atoms $AB\mathcal{B}''$, the same fit-domains $[AB\mathcal{B}'']$ are used. As is shown in the next section, the resulting fit domains are very compact; already with a very low number of atoms N_D per fit domain a very accurate fit is achieved.

The ERIs $(ij\mathcal{J}|P(\mathcal{P}'' \oplus \mathcal{A}))$, and $(ab\mathcal{B}''|P(\mathcal{P} \ominus \mathcal{A}))$ in Eqs. (3.26) and (3.25) become very small for large $R_{\mathcal{J}}$, and $R_{\mathcal{B}''}$, respectively, due to the spatial locality of the WFs and PAOs in the respective orbital product densities. The ranges of the cell indices $\mathcal{J}$ and $\mathcal{B}''$ hence can effectively be prescreened on the basis of the quasi-populations defined in Eqs. (3.28) and (3.29). In our implementation the ERIs are evaluated and transformed only for those $\mathcal{J}$ and $\mathcal{B}''$-cells, for which

$$\max_{(D\mathcal{D}ij)} q_{D\mathcal{D}}^{ij\mathcal{J}} > T^{\mathcal{J}}, \text{ and } \max_{(D\mathcal{D}AB)} q_{D\mathcal{D}}^{AB\mathcal{B}''} > T^{\mathcal{B}''}, \tag{3.30}$$

where $T^{\mathcal{J}}$ and $T^{\mathcal{B}''}$ are appropriate thresholds. It turns out, that the convergence of the resulting excitation energies w.r. to $T^{\mathcal{B}''}$ is relatively slow, despite reasonably good localization of the PAOs. Therefore, in order to

reach meV convergence in the CIS excitation energies several spheres of lattice vectors $\mathcal{B}''$ need to be included.

The ranges of the fitting functions $P\mathcal{P}$ and $P\mathcal{P}''$ in the fitting coefficients $d^{ij\mathcal{J}}_{P\mathcal{P}}$ and $d^{ab\mathcal{B}''}_{P\mathcal{P}''}$ are restricted to the corresponding fit-domains, *i.e.*, $P\mathcal{P} \in [ij\mathcal{J}]$, and $P\mathcal{P}'' \in [ab\mathcal{B}'']$, and thus are relatively small and close to the zeroth unit cell. In particular, the dependence on $\mathbf{R}_{\mathcal{A}}$ drops out, on going from Eq. (3.23) to Eq. (3.24). This, however, is not the case for the 3-index ERIs, which are contracted with these coefficients in Eqs. (3.25) and (3.26). Here, the dependence on $\mathbf{R}_{\mathcal{A}}$ remains, and the ranges of the fitting functions are substantially extended due to addition of all possible $\mathbf{R}_{\mathcal{A}}$ vectors. These $\mathbf{R}_{\mathcal{A}}$ appear in the final matrix-vector product $(\mathbf{Hc})^{a\mathcal{A}}_i$, and thus in the residual vector; the $\mathcal{A}$ range hence reflects the locality of the exciton.

The $\mathcal{B}''$ and $\mathcal{A}$ ranges thus are the two critical parameters influencing the size of the $(ab\mathcal{B}''|P(\mathcal{P} \ominus \mathcal{A}))$ integral distribution. Calculation (transformation), storage, and reading of these ERIs presently constitutes the computational bottleneck in terms of CPU time, input/output, memory and disk resources. The transformation of the 3-index ERIs from AO to PAO basis is done similarly as for the $(ia\mathcal{A}|P\mathcal{P})$ ERIs used for the LMP2 method. [6] However, since there are substantially more PAOs per cell than WFs, and since the former are usually less localized, the number of half-tranformed ERIs is much larger in the present, than in the LMP2 case. Therefore, an efficient transformation procedure requires a lot of memory, and, in addition, special paging techniques.

As is explained in Sec. 3.2.1, the range for the $\mathcal{A}$-cells is restricted to the WS supercell. Moreover, each WF ϕ_i possesses its own WS supercell, hence, its own $\mathcal{A}$ range. Note that since the ERIs $(ab\mathcal{B}''|P(\mathcal{P}\ominus\mathcal{A}))$ appearing in Eq. (3.25) do not explicitly refer to index i, the index $\mathcal{A}$ here is element of the union of all WS supercells belonging to different i. Yet, since all i are restricted to the zero cell the union of all WS supercells belonging to different i is not much larger than the individual Wigner-Seitz supercells

themselves. The implications on the size of this integral set thus are not excessive.

3.4 Calculations and discussions

The method as described above has been applied to several 3D test systems, ranging from wide-gap insulators to semiconductors. These comprise crystals with different type of bonding, *i.e.*, hydrogen bonded hexagonal ice, the ionic crystals LiH, MgO, and LiF, and the covalent crystals diamond, SiC, and Si. Structural data and the AO basis sets are provided as supplementary material (*vide infra* Appendix A.2).

3.4.1 Convergence with respect to the parameters of the computational scheme

Density fitting with a common, sufficiently large fit-domain, used for all orbital product densities to be fitted, has been employed in Chapter 2 for the 1D-case. There, it was shown that a sufficiently high accuracy of the fitting was achieved already with a small fitting basis set, *e.g.*, a GTO cc-pVDZ DF-MP2 fitting basis [103] converted into the mixed cc-pVDZ (GTO/PTO) basis [20]) for a DZ+P AO basis set. The same holds true also for the 3D case based on our local fitting scheme with much smaller, density-specific fit domains and the robust three-term formula (*vide supra*): *e.g.*, for a CIS calculation on the LiF crystal in a DZ+P AO basis, extending the fitting basis set from cc-pVDZ to cc-pVTZ quality the resulting excitation energies are affected only in the sub-microhartree range. As is evident from Table 3.1, the resulting excitation energies are very insensitive with respect to the fit-domain size (even a very few atoms in the fit domain suffice for microhartree-accuracy). A default threshold of 6 atoms appears as a conservative choice, and has been employed in all further calculations. We note that additional atoms are added to these domains for particular

densities, if dictated by their symmetry. Interestingly, for the density-fitted periodic LMP2 method, based on local density fitting, microhartree accuracy in the correlation energy is only achieved when using somewhat larger fit-domains [20].

Table 3.1: Singlet and triplet CIS excitation energies with respect to the variation of the fit domain size. The given domain sizes are the minimal domain sizes plus symmetry related atoms. The energies for LiF and MgO are calculated with a $5 \times 5 \times 5$ and $6 \times 6 \times 6$ cells in the WS supercell, respectively and a threshold $T^{\mathcal{B}''} = 10^{-5}$.

	ω_S / eV		ω_T / eV	
domain size	MgO	LiF	MgO	LiF
2	11.9208	15.8371	11.2565	15.1146
4	11.9209	15.8371	11.2566	15.1144
6	11.9209	15.8371	11.2567	15.1143
8	11.9209	15.8370	11.2567	15.1142
12	11.9210	15.8371	11.2567	15.1142

Other important parameters of the current scheme are the thresholds $T^{\mathcal{J}}$ and $T^{\mathcal{B}''}$ defining the ranges for the 3-index integrals to be evaluated and processed according to the spatial proximity of WF ϕ_i to WF $\phi_{j\mathcal{J}}$ or PAO ϕ_a to PAO $\phi_{b\mathcal{B}}$, respectively (*cf.* Sec. 3.3). The two-internal ERIs $(ij\mathcal{J}|P(\mathcal{P}''\oplus\mathcal{A}))$ are relatively inexpensive and not numerous, and therefore can be calculated with tight $T^{\mathcal{J}}$ without too much effort. Moreover, the results turned out to be insensitive with respect to this threshold. In all reported calculations a value of $T^{\mathcal{J}} = 10^{-5}$ was used.

Yet for the two external ERIs $(ab\mathcal{B}''|P(\mathcal{P}\ominus\mathcal{A}))$ the situation is different: tightening the $T^{\mathcal{B}''}$-threshold noticeably increases the size of this integral distribution, making the calculation considerably more expensive. Unfortunately, as shown in Table 3.2, the convergence of the excitation energies w.r. to this threshold is relatively slow: with $T^{\mathcal{B}''} = 10^{-4}$ the error can be still as large as 0.1 eV. Thus, a conservative value of $T^{\mathcal{B}''} = 10^{-5}$ has been

employed in the subsequent calculations. Compared to $T^{\mathcal{B}''} = 10^{-4}$ this implies on average an increase in the computing time by about 40%.

Table 3.2: Singlet and triplet CIS excitation energies of MgO and LiF (calculated with $6 \times 6\times$ and $5 \times 5 \times 5$ cells in the WS supercell, respectively) for different values of the threshold $T^{\mathcal{B}''}$.

	ω_S / eV		ω_T / eV	
$T^{\mathcal{B}''}$	MgO	LiF	MgO	LiF
10^{-2}	12.3243	15.9471	11.6740	15.2305
10^{-3}	12.1917	15.9249	11.5163	15.1960
10^{-4}	11.9785	15.8476	11.3068	15.1229
10^{-5}	11.9209	15.8371	11.2567	15.1143
10^{-6}	11.8781	15.8345	11.2176	15.1117
10^{-7}	11.8687	15.8344	11.2101	15.1117

3.4.2 Localization of the CIS coefficients

The physical nature of an exciton manifests itself (i) in the localization of the CIS coefficients in the reciprocal-space canonical representation with respect to the band and **k**-vector indices, and (ii) in their spatial localization in the direct-space representation. These characteristics influence various physical properties, as well as the computational effort needed to correctly evaluate the corresponding excitation energies.

The relative contributions of the squared CIS coefficients related to different bands (summed over the **k**-points), of the CIS wave functions calculated for the SiC and MgO crystals, are shown in Fig. 3.1. Since the lowest excited states in these systems are degenerate (triply degenerate in MgO, and doubly in SiC) the contributions are averaged over these states. It is seen that for the lowest excited states the major contribution comes from the LUCO-band, while the other unoccupied bands virtually do not contribute. Indeed, the exclusion of all the virtual bands apart from

the LUCO-band affects the CIS excitation energy only marginally, *i.e.*, it increases by only 0.5 eV in MgO, and by 0.6 eV in SiC.

A modification of the AO basis set itself, on the other hand, has a much larger impact on the resulting energies: as was shown in Ref. 104 for the case of the MgO crystal, a variation of the exponent of only one *sp*-shell of the AOs centered on the Mg atoms reduces the excitation energy by nearly 2 eV. This originates from the fact that the standard basis sets, optimized for the ground state, are suboptimal for excited states, which leads to an unbalanced description of ground and excited states, and thus to a substantial overestimation of the excitation energies. In molecular calculations this problem is usually alleviated by augmenting the basis set with diffuse functions, which in many cases returns the desired balance, although Rydberg states are often overcorrected.

For solids, due to linear dependencies, diffuse orbitals are difficult to process, and, furthermore, hardly useful in 3D-packed systems [104, 105]. This is quite a general issue for AO-based calculations of excited states, asking, in our view, for considerable attention in the future.

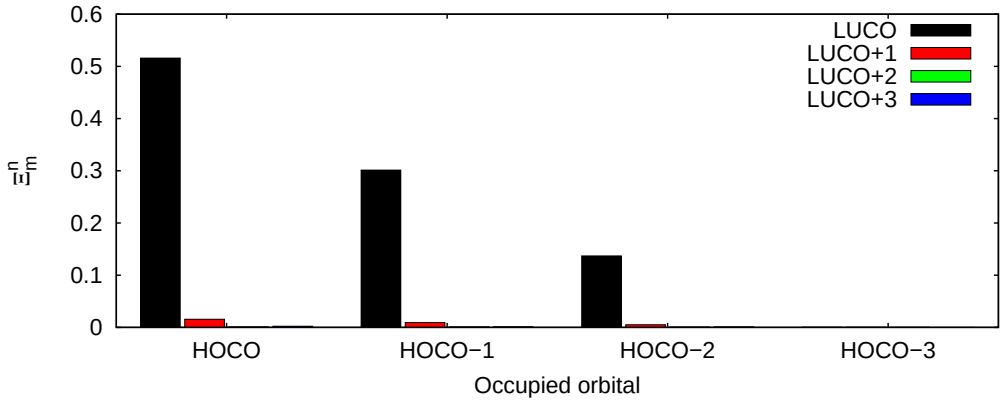

(a) MgO

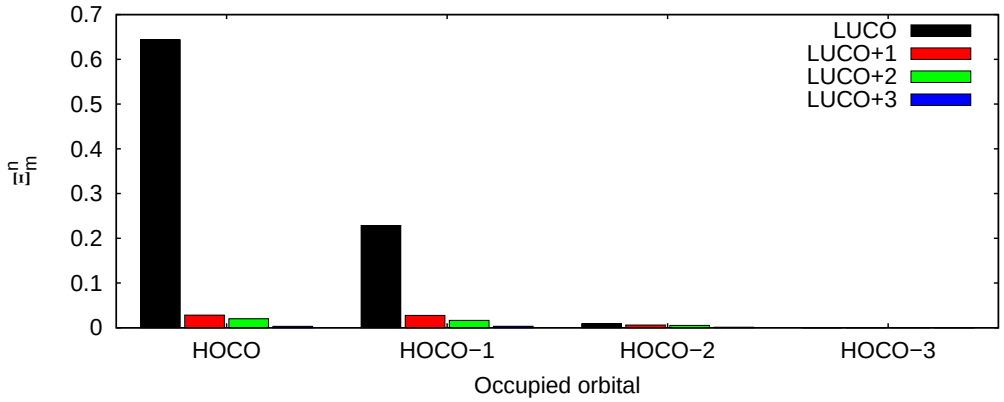

(b) SiC

Figure 3.1: The CIS coefficients in canonical space. The columns show a HOCO-band$-n$ to a LUCO-band$+m$ ($m, n = 0, 1, 2, 3$) contribution to the squares of the CIS coefficient of the singlet state (summed over all $\mathbf{k}$-points) $\Xi_m^n = \sum_{\mathbf{k}} \left| c_{\mathrm{LUCO}+m}^{\mathrm{HOCO}-n}(\mathbf{k}) \right|^2$. The contributions are averaged over the 3 and 2 degenerate excitonic states in (a) MgO and (b) SiC, respectively.

The limited size of the virtual space required for a proper description of the lowest CIS state, as illustrated in Fig. 3.1, unfortunately cannot straightforwardly be exploited in our scheme, since a truncation of the virtual space in reciprocal space to specific bands does not translate to a corresponding truncation of the PAOs in direct space. Possibly, the virtual space could be represented by a limited number of specially constructed

Wannier functions, designed to reproduce the low-lying virtual bands as accurately as possible [57, 106, 107], yet this was not tried in the present work. On the other hand, the CIS method presented here is meant as an integral part of a higher-order correlated treatment, which in turn will demand a rich virtual space to properly describe electron correlation effects.

The canonical CIS coefficients, as displayed in Fig. 3.2, are also localized w.r. to the **k**-vectors within the respective band, yet not as pronounced as w.r. to the band index. The CIS coefficients of the lowest energy excitons of MgO tend to localize around the Γ-point, while those of SiC around the X-point of the BZ, which in both cases correlates with the position of HOCO-LUCO energy difference minimum.

The degeneracy of the HOCO of MgO at the Γ-point is 3, while the related LUCO is not degenerate. Therefore, the orbital energies of the HOCO, HOCO-1 and HOCO-2 bands around the Γ-point are quite close, implying that the weights of the determinants related to these orbitals are similar. This explains why in Fig. 3.1 the excitations from the three uppermost occupied bands of MgO have similar weight in the CIS wavefunction. The bands HOCO-3 and LUCO+1, on the other hand, are energetically well separated within this region of the BZ from HOCO and LUCO, respectively, the weights of the determinants related to these bands, therefore, are much smaller compared to the weights related to excitations from HOCO, HOCO-1, or HOCO-2 to LUCO.

A similar situation occurs for the SiC crystal, with the sole difference that the essential contributions come from **k**-vectors in the vicinity of the X-point. The HOCO state is doubly degenerate there, while the LUCO state is again non-degenerate. Therefore, only excitations from HOCO and HOCO-1 to LUCO are mainly involved in building the CIS wavefunction.

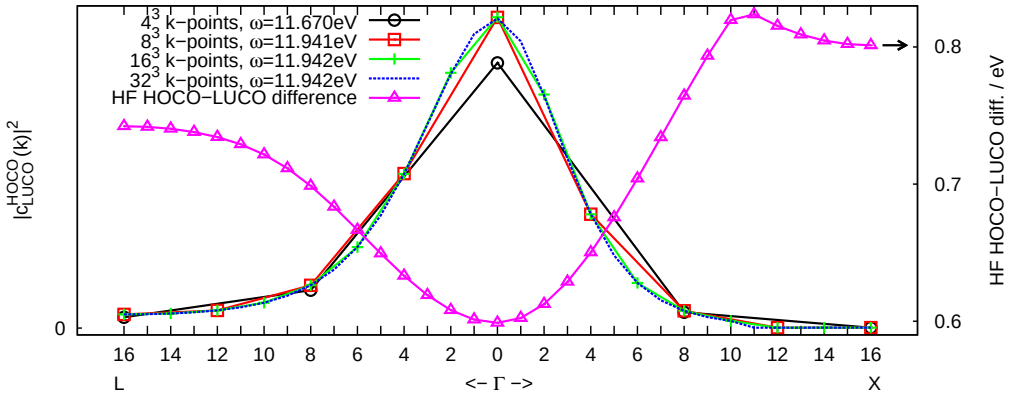

(a) MgO

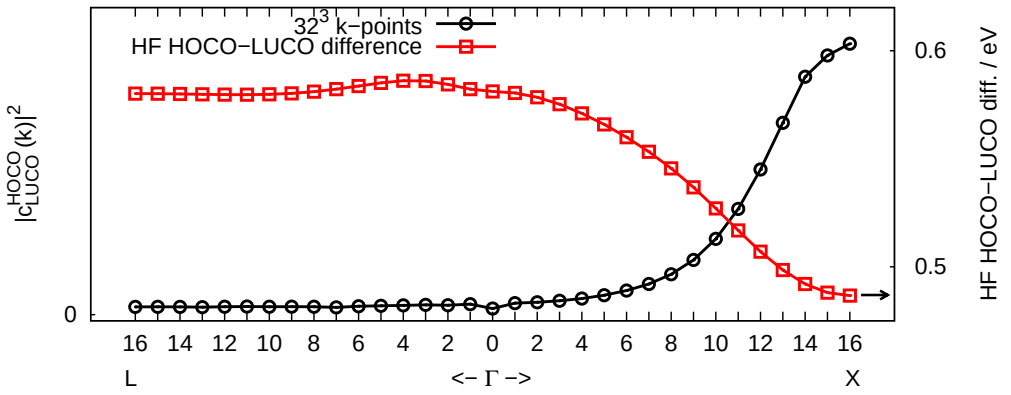

(b) SiC

Figure 3.2: HOCO-LUCO contribution to the CIS wavefunction, $|c^{\mathrm{HOCO}}_{\mathrm{LUCO}}(\mathbf{k})|^2$, of (a) MgO and (b) SiC and corresponding HF HOCO-LUCO differences. In the case of MgO different **k**-meshes are taken.

The better the localization of the CIS coefficients in the **k**-space is, *i.e.*, the less smooth these coefficients as a function of **k** are, the denser a uniform **k**-grid has to be chosen for the numerical quadrature over the BZ (*cf.* Sec. 3.3 for a detailed discussion). The degree of localization of the CIS coefficients in the **k**-space (non-smoothness as a function of **k**) relates conversely to their localization in direct space, which in turn is related to the electron-hole attraction. It thus provides a measure for the nature of the exciton. Moreover, the localization of the CIS coefficients

in direct space determines to large extent the computational resources needed to perform the calculation. Indeed, in order to obtain a converged value for the excitation energy the Wigner-Seitz supercell truncating the $\mathbf{R}_{\mathcal{A}}$ vectors must be chosen large enough that it covers all non-negligible CIS coefficients $c^i_{a\mathcal{A}}$, making delocalized excitons more difficult to treat.

Fig. 3.3 displays a histogram of the maximal CIS coefficients $\max_{ia}|c^i_{a\mathcal{A}}|$ for different distances between a WF and a PAO. Evidently, the localization of the exciton correlates with the value for the band gap (*cf.* Sec. 3.4.4). Among the systems considered here, the most localized exciton is observed for the wide-gap insulator LiF, while the localization of the exciton in the semiconductor Si is the weakest. Interestingly, despite a lesser localization of the exciton in Si relative to that in diamond in terms of the absolute distance; both excitons have very similar localization in terms of the number of unit cells to be included in the Wigner-Seitz supercell. The computational cost hence is similar for both systems. For all exemplary systems ranging from wide-gap insulators to semiconductors the lowest-energy excitons are all reasonably well localized, such that they can be treated with the proposed approach.

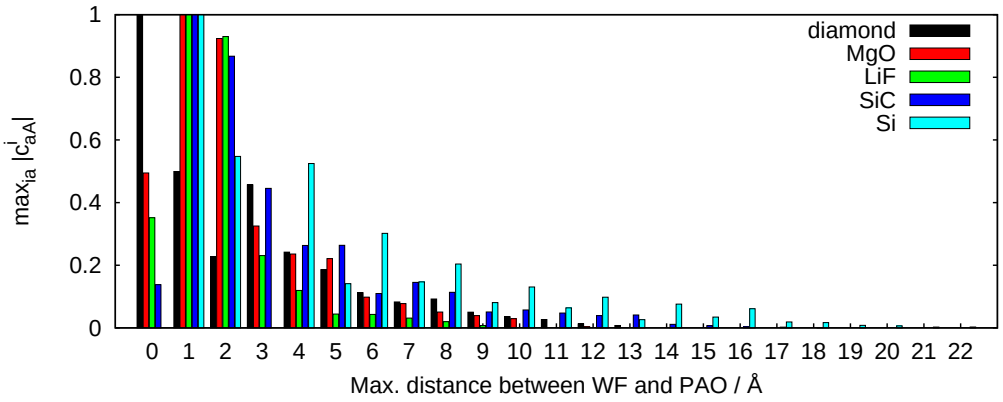

Figure 3.3: The maximal CIS coefficients of the singlet state in direct space against the maximal distance between WF and PAO, $\max_{ia}|c^i_{a\mathcal{A}}|$, for the systems diamond, MgO, LiF, SiC and Si.

3.4.3 Convergence with respect to reciprocal space sampling and Wigner-Seitz supercell size

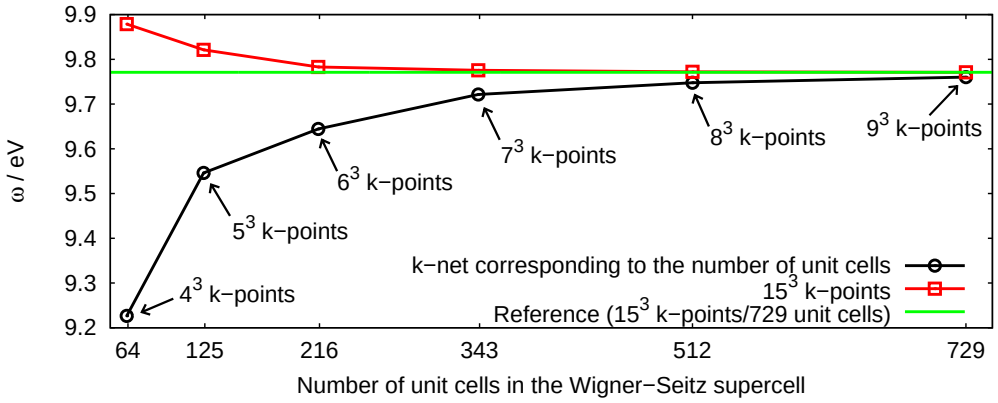

(a) SiC

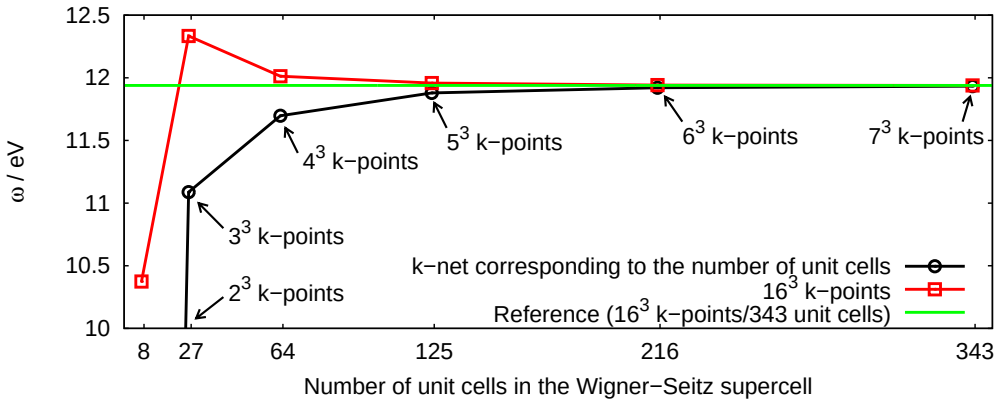

(b) MgO

Figure 3.4: Singlet state excitation energies of (a) SiC and (b) MgO as a function of the number of unit cells included in the direct space description of the exciton. Calculations are performed for the cyclic model (black curves with dots), and for the WSS-TIM with a very dense **k**-mesh ($15 \times 15 \times 15$, and $16 \times 16 \times 16$ for SiC and MgO (red curves with squares), respectively). The reference values are obtained by employing the WSS-TIM, employing a $15 \times 15 \times 15$ **k**-mesh with a WS supercell of 729 unit cells (SiC), and a $16 \times 16 \times 16$ **k**-mesh with a Wigner-Seitz supercell of 343 unit cells (MgO), respectively (horizontal green lines).

In Sec. 3.2.1 two finite models of a crystal, namely the cyclic model [27, 92, 98] and WSS-TIM were discussed. Here we investigate the convergence of the excitation energies with respect to the truncation parameter within both models. Fig. 3.4 displays, for the cases of the MgO and SiC crystals, the calculated excitation energies as a function of the Wigner-Seitz supercell, (i) for the cyclic model, and (ii) for the WSS-TIM with a very dense **k**-mesh ($15 \times 15 \times 15$, and $16 \times 16 \times 16$ for SiC and MgO, respectively). Evidently, for the WSS-TIM the convergence of the excitation energies to the infinite crystal values is much better than for the pure cyclic model. Already for a Wigner-Seitz supercells corresponding to **k**-meshes of modest density ($7 \times 7 \times 7$ for SiC, and $5 \times 5 \times 5$ for MgO) the resulting excitation energies are essentially converged. The error of the cyclic model thus originates mainly from an inadequate quadrature over the BZ. Increasing the density of the **k**-mesh is, as already stated above, computationally inexpensive, but significantly improves the quality of the calculation. On the other hand, due to good spatial localization of the CIS coefficients $c^i_{a\mathcal{A}}$ in direct space (*cf.* Fig. 3.3), restricting them (and their matrix-vector products $(\mathbf{Hc})^{a\mathcal{A}}_i$ to a finite Wigner-Seitz supercell, *i.e.*, truncating $\mathbf{R}_{\mathcal{A}}$, causes a much smaller error.

The importance of improved BZ quadrature is also hinted at by Fig. 3.2 showing the locality of the (most important) HOCO-LUCO contribution to the CIS vector in the BZ: apparently only 16^3 **k**-points provide sufficient support to accurately describe it along the L-Γ-X direction.

3.4.4 Comparison to experiment

Table 3.3 compares the lowest CIS excitation energies to the corresponding experimental values of our set of test systems. The used threshold of $T^{\mathcal{B}''} = 10^{-5}$ (*cf.* Sections 3.3 and 3.4.1), as well as the obtained value for the norm of the exciton in direct space representation (*cf.* Sec. 2.3.2) suggest, that the values for the CIS excitation energies are converged up to a few hundredths of an eV w.r. to the size of the Wigner-Seitz supercell and the

$T^{\mathcal{B}''}$ threshold. From Table 3.3 it is evident, that the CIS method grossly overestimates the experimental excitation energies with errors up to 5 eV (for diamond). In molecular calculations the errors of the CIS method usually do not exceed 1-2 eV for the lowest states. There are two possible origins of the larger discrepancy for solids, as observed in our calculations. First of all, the CIS description lacks dynamical electron correlation effects (screening). The magnitude of the correlation energy is generally larger in the excited state than in the ground state, hence the uncorrelated CIS treatment tends to overestimate the excitation energy. The error due to the neglect of screening is expected to be more significant in 3D bulky systems than in molecules, or in 1D or 2D systems. [108]

The other origin is the AO basis set deficiency, which becomes a major issue in solids. Indeed, augmenting the basis by diffuse functions, which is usually a good strategy to obtain a decent description of excited states in molecules, however, is difficult in 3D packed systems and does little good. The basis sets commonly used in periodic calculations are clearly biased towards the ground state, which leads to a further overestimation of the excitation energy. As already mentioned in Sec. 3.4.2, and demonstrated in the next Chapter [Chapter 4], tweaking the basis set significantly affects the excitation energies and can easily lead to a decrease by several eV. Both issues, *i.e.*, the lack of dynamical electron correlation, and the basis set problem, will be addressed in future work.

Table 3.3: Experimental band gaps, Hartree-Fock HOMO-LUMO vertical band gaps (E_g^{HF}), vertical CIS excitation energies to the lowest singlet and triplet exciton state (calculated using WSS-TIM) and corresponding norms of the CIS vector in direct space [92]. The fitting basis set related to the cc-pVDZ AO basis was used.

			singlet		triplet	
system	exp. / eV	E_g^{HF} / eV	ω / eV	norm	ω / eV	norm
LiH	6.5	12.82	7.68	0.9993	7.13	0.9997
Ice	10.9	18.28	12.13	0.9999	11.17	1.0000
diamond	6.5	16.66	11.72	0.9916	10.34	0.9981
MgO	8.7	16.29	11.94	0.9993	11.27	0.9997
LiF	13.6	22.40	15.84	1.0000	15.12	1.0000
SiC	6.0	13.80	9.74	0.9957	9.29	0.9967
Si	3.4	8.43	6.05	0.9886	5.62	0.9917

All the calculations presented in this article were performed by using a serial version of our program. The computational time is mainly determined by the size of the Wigner-Seitz supercell, *i.e.*, by the locality of an exciton. The calculations took from a few hours (for the relatively well localized exciton in LiF, where a $6 \times 6 \times 6$ supercell was sufficient) to a few days for Si (where a $9 \times 9 \times 9$ supercell was needed). Note that for larger unit cells smaller Wigner-Seitz supercells can be used to capture an exciton of a certain locality. *E.g.*, for ice, already a $3 \times 3 \times 3$ supercell was sufficient. The present bottleneck of the calculations are evaluation, sorting, and storage of the three-index ERIs ($ab\mathcal{B}''|P(\mathcal{P} \ominus \mathcal{A})$) (*cf.* Sections 3.2.3 and 3.3).

3.5 Conclusions

In this contribution we presented theory, implementation, and first results for a general 3D-periodic density-fitted local CIS method. The method is a generalization of a 1D-periodic CIS method presented recently (*cf.* Chapter 2). The Davidson diagonalization of the CIS Hamiltonian matrix is

carried out in reciprocal space, while the diagrams of the residual calculation are evaluated partially in the direct, and partially in the reciprocal space. For the Coulomb diagram describing exciton-exciton interaction an Ewald technique was utilized to efficiently carry out the necessary infinite lattice summations. The exchange diagram describing the electron-hole interaction is calculated entirely in direct space, employing a robust product-density specific density fitting scheme. The sparsity due to the spatial locality of the orbitals and CIS coefficients is fully utilized.

The reciprocal-space parts of the calculation are inexpensive, which allows for the use of dense **k**-meshes, decoupled from the actual size of the WS supercell via the Wigner-Seitz supercell truncated infinite model, WSS-TIM. It turns out that such a decoupling is very beneficial, leading to much quicker convergence of the resulting excitation energies w.r. to the size of the underlying supercell in direct space.

The CIS method itself, although substantially improving the zeroth-order band gap energy, (*i.e.*, the HOCO-LUCO energy difference), still noticeably overestimates the experimental band gaps by several eV. Reasons for this are (i) the lack of dynamical correlation effects (screening), and (ii) deficiencies in the AO basis sets. The CIS method presented here, is to be seen as the first building block of a more elaborate treatment including dynamical correlation effects via *e.g* local CIS(D) [30] or CC2 [14, 83, 109] methods. A promising possibility to fix the problem of AO basis set deficiencies would be to augment the AO basis sets by a small amount of plain waves (with low energy cutoff). Another route to explore is the combination of the present periodic CIS method with TD-DFT (or its Tamm-Dancoff approximation) in the framework of a long-range–short-range separation of the electron-electron interaction operator [110].

Chapter 4

Investigations on basis set effects

4.1 Introduction

The CIS exciton wavefunction with the symmetry $\mathbf{k}_{\text{exc}}$ is defined as (*cf.* Chapters 2 and 3)

$$\begin{aligned} |\Psi_{\text{exc}}(\mathbf{k}_{\text{exc}})\rangle &= \hat{C}_1(\mathbf{k}_{\text{exc}})|0\rangle, \quad \text{with} \\ \hat{C}_1(\mathbf{k}_{\text{exc}}) &= \sum_{i\mathcal{I}a\mathcal{A}} c_{a\mathcal{A}}^{i\mathcal{I}}(\mathbf{k}_{\text{exc}})\hat{E}_{i\mathcal{I}}^{a\mathcal{A}} \\ &= \sum_{\bar{i}\mathbf{k}_i\bar{a}\mathbf{k}_a} c_{\bar{a}\mathbf{k}_a}^{\bar{i}\mathbf{k}_i}(\mathbf{k}_{\text{exc}})\hat{E}_{\bar{i}\mathbf{k}_i}^{\bar{a}\mathbf{k}_a} , \end{aligned} \tag{4.1}$$

in the direct and reciprocal (canonical) space, respectively. Here $c_{a\mathcal{A}}^{i\mathcal{I}}(\mathbf{k}_{\text{exc}})$ denotes the CIS coefficients in the direct space (the orbital and cell indices for WFs and PAOs are i, $\mathcal{I}$ and a, $\mathcal{A}$, respectively), while $c_{\bar{a}\mathbf{k}_a}^{\bar{i}\mathbf{k}_i}(\mathbf{k}_{\text{exc}})$ are their canonical counterparts ($\bar{i}$,$\bar{a}$ denote the occupied and virtual Bloch orbitals with translational symmetry $\mathbf{k}_i$ and $\mathbf{k}_a$). The spin-conserving one particle excitation operators $\hat{E}_{i\mathcal{I}}^{a\mathcal{A}}$ (direct space) or $\hat{E}_{\bar{i}\mathbf{k}_i}^{\bar{a}\mathbf{k}_a}$ (reciprocal space) act on the Hartree-Fock reference $|0\rangle$. Presently, Γ-point ($\mathbf{k}_{\text{exc}} = 0$) excitons can be calculated, which correspond to *vertical* excitations ($\mathbf{k}_a = \mathbf{k}_i$) in the canonical basis or periodic excitations $c_{a\mathcal{A}}^{i\mathcal{I}} = c_{a(\mathcal{A}\ominus\mathcal{I})}^{i0}$ in the direct space. Non-vertical excitations ($\mathbf{k}_{\text{exc}} \neq 0$) can presently be calculated by the supercell method.

The CIS eigenvalue problem $\hat{H}\hat{C}_1|0\rangle = \omega_{\mathrm{CIS}}\hat{C}_1|0\rangle$ is solved in the canonical basis by employing the Davidson diagonalization method. [10] The electron repulsion integrals in $\hat{H}\hat{C}_1|0\rangle$ are decomposed in the direct space employing density fitting (DF). [92] The DF integrals and coefficients are evaluated in the local basis of WFs and PAOs and at each iteration contracted with the direct-space images of the trial CIS coefficients. The actual 4-index electron repulsion integrals are thus never assembled, which reduces the nominal scaling of the method with system size to $O(N^4)$. The resulting two-electron part of $\hat{H}_N\hat{C}_1|0\rangle$ then is Fourier-transformed to the reciprocal space in each iteration of the Davidson diagonalization procedure.

Our first implementation, reported in Chapter 2, was limited to polymers. The reason was that the lattice sums required for the construction of the Coulomb two-electron part of $\hat{H}\hat{C}_1|0\rangle$ converge only in the 1D case. Yet in the present version of the program this restriction has been overcome by implementing a multipole expansion for non-overlapping DF integrals in combination with an Ewald-like procedure to carry out the infinite lattice sums inside the DF procedure. This new approach was discussed in detail in Chapter 3.

In the following we will present some test calculations of CIS excitonic band gaps of the MgO and LiF crystals and explore how the band gaps depend on the diffuseness of the basis set. The use of atom-centered basis sets in periodic systems is generally a long-standing issue, [102] which does not yet have an ultimate solution. Standard Gaussian basis sets (optimized for molecular calculations) are hardly applicable even at the HF level because of quasi-linear dependencies, leading to numerical instability. It is usually argued, however, that in well-packed periodic systems devoid of voids, diffuse atomic orbitals are needless and even counterproductive. An accurate description of electron correlation in the ground state of periodic systems requires somewhat more diffuse basis functions compared to HF, but still substantially less diffuse than those of molecular basis sets. [105] The situ-

ation, though, is different for excitation energies, and the basis set problem is much more delicate even for molecules. Since standard Gaussian basis sets are usually optimized for the description of electronic ground states they naturally are less optimal for the excited states. Due to this lack of balance, the excitation energies as the difference of ground and excited state energies are generally overestimated. In molecular calculations, augmenting the basis set by additional diffuse functions usually leads to an appreciable lowering of the excitation energy (of the same valence state). In the following we investigate the effect of increasing diffuseness of the basis set on the fundamental and excitonic band gaps of dense 3D crystals.

4.2 Calculations and discussions

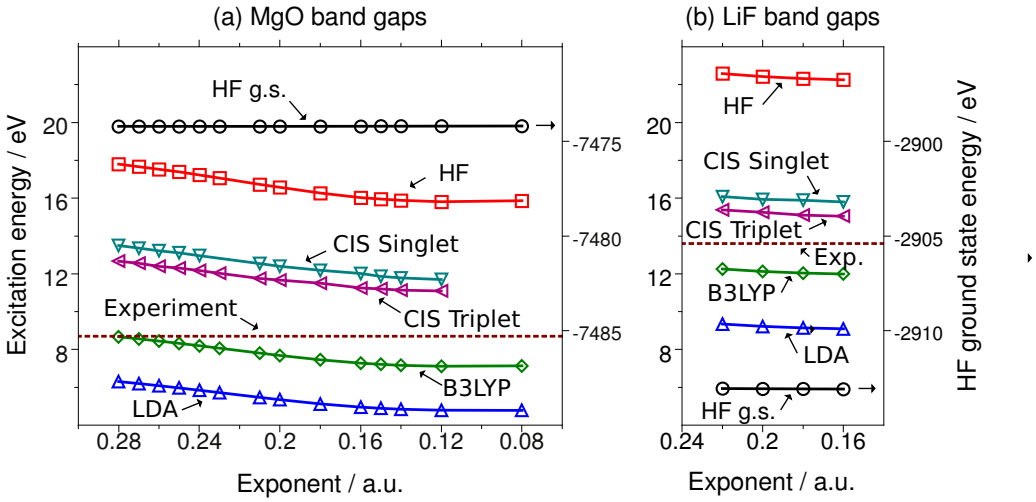

Figure 4.1: The HF ground state energies (in the right y-axis) and Γ-point HOCO-LUCO (HF, DFT) and CIS band gap energies (in the left y-axis) for the MgO (a) and LiF (b) crystals as functions of the exponent of the most diffuse *sp*-shell in the Mg or Li basis set, respectively. The widths of the plots have been chosen to maintain the same scale of the x-axis.

First, we consider the excitonic (optical) Γ-point band gap of the MgO crystal. The basis sets we used for the calculations are 8-511G* for Mg and 8-51G* for oxygen, which have been employed in a number of periodic

HF or DFT calculations. [111, 112] It is noteworthy that the most diffuse Mg *sp*-primitive Gaussians of that basis are, with an exponent of 0.28 a.u., far less diffuse than in any molecular Mg basis set. For instance, in Pople's 3-21G basis set the most diffuse primitive has an exponent of 0.0464011 a.u. Such diffuse basis set are definitely not applicable in periodic calculations, but even much less diffuse ones, which still can be processed in the periodic SCF procedure apparently do not improve the ground state energy. Yet this is no longer fulfilled for the excited states. Fig. 4.1 (a) shows the dependence of the CIS band gap, the HF total energy, and the DFT (B3LYP and LDA) Γ-point difference between the highest occupied and lowest unoccupied crystalline orbitals (HOCO-LUCO), on the value of the exponent of the most diffuse orbital. For the largest value of the exponent (0.28 a.u.) the CIS band gap is much closer to the experimental value than the HF HOCO-LUCO difference, but still grossly overestimates it (by about 5 eV). However, the diffuseness of the *sp*-primitives has a strong effect on both the CIS energy and the HF HOCO-LUCO difference: decreasing the exponent of the sp-primitives from 0.28 a.u. to 0.14 a.u. decreases both quantities by nearly 2 eV. The curve of the CIS energy, of which the HF HOCO-LUCO difference is its zeroth-order contribution, is nearly parallel to the curve of the latter. Evidently, the lowering of the band gap indeed is due to an improved description of the excited state, rather than a degradation in the ground state energy: the latter remains virtually unaffected by the variation of the basis set. Still, very diffuse functions (like in molecular basis sets) are still not of a much use in crystals even for excited states: CIS energy and HF HOCO-LUCO difference both saturate for exponents smaller than 0.15 a.u.

Interestingly, the DFT HOCO-LUCO difference, which is often interpreted and used as the optical band gap (for non-hybrid functionals the time-dependent DFT band gap in solids indeed coincides with the HOCO-LUCO difference [52, 63]), is also severely affected by the diffuseness of the basis set. For instance, the B3LYP HOCO-LUCO difference obtained

for the largest exponent, is indeed quite close to the experimental value. However, with improvement of the basis set it decreases parallel to HF, and for exponents smaller than 0.15 a.u. it finally deviates noticeably from the experiment.

In the case of the LiF crystal (shown in Fig. 4.1 (b)) the decrease of the exponent of the most diffuse lithium *sp*-shell (from 0.22 to 0.14 a.u.) does not alter the value of the band gap much. At the same time, the initial CIS error in this case is much smaller than in the MgO case (around 2.5 eV).

4.3 Conclusions

To summarize, these calculations indicate that basis set effects can play an important role for excited states in 3D solids even at the uncorrelated CIS level. With well balanced basis sets the CIS error can be reduced to 2-3 eV, or even less, which is about twice as large as the usual CIS error in molecular calculations (1-2 eV). The accuracy can be further improved by including dynamic correlation (or screening) effects, which are larger in 3D solids than in 2D slabs or molecules. [108]. The problem of imbalance in the description of electronic ground and excited states asks for a rigid solution, particularly in the context of periodic systems. Since diffuse functions are of prime importance here, augmenting standard Gaussian basis set by low energy plane waves might be a promising way forward.

Chapter 5

Summary

In this work a new configuration interaction singles method for Frenkel- and intermediate excitons with one-dimensional, two-dimensional and three-dimensional periodicity is presented. The method is based on the Davidson diagonalization procedure, carried out in reciprocal space. The one-electron part of the matrix-vector products is also evaluated in the reciprocal space, where the diagonality of the Fock matrix can be exploited. The contraction of the CIS vectors with the two electron integrals is performed in the direct space in the basis of localized occupied (Wannier) and virtual (projected atomic) orbitals. The direct space approach allows to utilize the sparsity of the integrals due to the local representation and locality of the exciton. The Ewald technique is employed to carry out infinite lattice summations for the exciton-exciton interaction, and robust product-density specific local density fitting in direct space for the electron-hole interaction. Moreover, an alternative to the usual cyclic model with Born-von Karman periodic boundary conditions is considered, the so called Wigner-Seitz supercell truncated infinite model, which exhibits much improved convergence of the CIS excitation energy with respect to the size of the supercell.

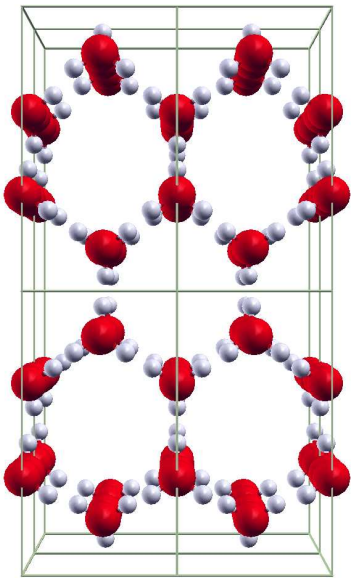

Figure 5.1: Hexagonal ice.

Test calculations on a series of prototypical systems, for instance hexagonal ice (*cf.* Fig. 5.1), demonstrate that the method at the present stage can be used to calculate the excitonic band gaps of 1D, 2D and 3D periodic systems with up to a dozen atoms in the unit cell, ranging from wide-gap insulators to semiconductors.

Since the CIS method is lacking dynamical electron correlation (screening) and moreover the utilized AO basis sets do not allow for convergence with respect to the basis set size, the accuracy of the reported results is not very high. Nevertheless, the first-time insights in the direct space physics of the exciton make the method valueable. Additionally, the quantum mechanical hierachy of methods ennobles the presented method to be the keystone to further developments in the direction of including dynamical electron correlation, *e.g.* local CIS(D) [30] or CC2 [14,83,109] methods. Also it can be combined with density functional based methods to include electron correlation by splitting electron-electron interactions into long-range and short-range contributions [110].

Appendix A

Supplementary data

A.1 Supplementary data for Chapter 2

```
Argon polymer
POLYMER
1
3.6982
1
18   0.5   0.0   0.0
ENDG
```

Figure A.1: Input geometry of argon polymer according to CRYSTAL [69] specification. The basis set is 6-31G**. The Hartree Fock energy is -526.771 769 Hartree.

```
LiH polymer
POLYMER
1
4.084
2
3    0.5   0.00000000  0.
1    0.00   0.00000000  0.
ENDG
```

Figure A.2: Input geometry of LiH polymer according to CRYSTAL [69] specification. The basis set is 6-31G** with an increased exponent (.35961972D-01 to .6D-01) The Hartree Fock energy is -8.028 720 Hartree.

```
h2o polymer
POLYMER
1
4.965635
6
8    0.000000000000   0.6852945000000   0.000000000000
8    0.500000000000  -0.6852945000000   0.000000000000
1    0.032558000000   1.5213825000000  -0.400375000000
1   -0.467442000000  -1.5213825000000   0.400375000000
1    0.168195000000   0.2242435000000   0.000000000000
1   -0.331805000000  -0.2242435000000   0.000000000000
ENDG
```

Figure A.3: Input geometry of water polymer according to CRYSTAL [69] specification. The basis set is 6-31G**. The Hartree Fock energy is -152.069 755 Hartree.

```
polyethene
POLYMER
1
2.567862325
6
6   0    -0.420090505   0
1   0    -1.082848037   0.87855148
1   0    -1.082848037  -0.87855148
6   0.5   0.420090505   0
1   0.5   1.082848037   0.87855148
1   0.5   1.082848037  -0.87855148
END
```

Figure A.4: Input geometry of polyethene according to CRYSTAL [69] specification. The basis set is 6-31G**. The Hartree Fock energy is -78.075 002 Hartree.

```
polybiphenyl parallel
POLYMER
1
4.37084638
10
6     1.701231102572E-01  0.000000000000E+00  0.000000000000E+00
6    -1.701231102572E-01  0.000000000000E+00  0.000000000000E+00
6     3.410921962585E-01  1.193204388641E+00  0.000000000000E+00
6     3.410921962585E-01 -1.193204388641E+00  0.000000000000E+00
6    -3.410921962585E-01 -1.193204388641E+00  0.000000000000E+00
6    -3.410921962585E-01  1.193204388641E+00  0.000000000000E+00
1     2.257231904049E-01  2.153916890503E+00  0.000000000000E+00
1     2.257231904049E-01 -2.153916890503E+00  0.000000000000E+00
1    -2.257231904049E-01 -2.153916890503E+00  0.000000000000E+00
1    -2.257231904049E-01  2.153916890503E+00  0.000000000000E+00
ENDG
```

Figure A.5: Input geometry of parallel polybiphenyl according to CRYSTAL [69] specification. The basis set is 6-31G with an increased exponent of the most diffuse sp-function of carbon from 0.16871448 to 0.18. The Hartree Fock energy is -229.462 964 Hartree.

```
polybiphenyl perpendicular
POLYMER
1
8.65690152
20
6     8.639856680011E-02 -5.641504670495E-06 -5.025915220729E-07
6    -8.639854904065E-02 -2.360798721063E-05 -1.483528005619E-05
6     1.694178140767E-01  1.203722104692E+00  1.154731232944E-04
6     1.694252573254E-01 -1.203684934167E+00 -3.037786166373E-05
6    -1.694211160439E-01 -2.322134992836E-05  1.203690842168E+00
6    -1.694219431371E-01 -1.601663980468E-04 -1.203716305436E+00
1     1.071328567863E-01  2.148138879745E+00  9.910722693041E-05
1     1.071462614543E-01 -2.148130576646E+00 -1.431112165953E-04
1    -1.071389472799E-01 -5.864268586688E-06  2.148120489552E+00
1    -1.071401977038E-01 -2.424004103089E-04 -2.148149048345E+00
6    -4.136014481773E-01  9.354611784515E-05 -2.621161059496E-06
6     4.136014379005E-01  8.588118754088E-05 -4.770748004308E-06
6    -3.305789761094E-01 -7.146022631342E-05 -1.203709748018E+00
6    -3.305779576460E-01  6.924899163095E-05  1.203697366094E+00
6     3.305821026234E-01 -1.203640620743E+00 -3.117247601549E-05
6     3.305748370739E-01  1.203766342017E+00  1.009321510258E-04
1    -3.928612327159E-01 -1.424443112123E-04 -2.148138959112E+00
1    -3.928596251785E-01  1.008823292615E-04  2.148130565509E+00
1     3.928669705713E-01 -2.148057628580E+00 -1.254004900583E-04
1     3.928538884209E-01  2.148211681512E+00  1.120769121366E-04
ENDG
```

Figure A.6: Input geometry of perpendicular polybiphenyl according to CRYSTAL [69] specification. The basis set is 6-31G with an increased exponent of the most diffuse sp-function of carbon from 0.16871448 to 0.18. The Hartree Fock energy is -458.929 101 Hartree.

```
polystyrene isotactic
POLYMER
1
2.93173381
16
6     0.000000000000E+00  2.550517134746E-01  9.050475385592E-01
6     0.000000000000E+00  4.428389595750E-01  2.409399230249E+00
1     0.000000000000E+00  1.521029603390E+00  2.610873077117E+00
6    -5.000000000000E-01 -1.187475505336E-01  3.035727266938E+00
1    -5.000000000000E-01  9.453778917554E-02  4.111193789567E+00
1    -5.000000000000E-01 -1.208879788252E+00  2.927471191342E+00
6     0.000000000000E+00 -1.021176337447E+00  3.327124925266E-01
6     0.000000000000E+00 -1.185409000648E+00 -1.046372347168E+00
6     0.000000000000E+00 -7.564430598468E-02 -1.885660220021E+00
6     0.000000000000E+00  1.198455697754E+00 -1.332533687562E+00
6     0.000000000000E+00  1.357388682195E+00  4.876024627336E-02
1     0.000000000000E+00 -1.902862841013E+00  9.699996168946E-01
1     0.000000000000E+00 -2.184930761274E+00 -1.474302780637E+00
1     0.000000000000E+00 -2.071650481986E-01 -2.964340132497E+00
1     0.000000000000E+00  2.078244032949E+00 -1.971183812014E+00
1     0.000000000000E+00  2.357269054837E+00  4.777661304326E-01
ENDG
```

Figure A.7: nput geometry of isotactic polystyrene according to CRYSTAL [69] specification. The basis set is 6-31G with an increased exponent of the most diffuse sp-function of carbon from 0.16871448 to 0.18. The Hartree Fock energy is -307.415 316 Hartree.

```
polystyrene syndiotactic
POLYMER
1
5.15351747
32
6     0.000000000000E+00 -3.011434296429E-01 -1.650104935774E+00
6    -5.000000000000E-01  1.676281143074E+00  3.129444394401E-01
6     0.000000000000E+00  1.754853066221E-03 -1.534957686844E-01
6    -5.000000000000E-01  1.774697515521E-01  2.134218481315E-02
1     0.000000000000E+00  1.092244467519E+00 -4.664122840638E-02
1    -5.000000000000E-01  6.242681404307E-02 -1.068293379050E+00
6    -2.499960947716E-01 -5.117500346253E-01  5.396120592340E-01
6     2.499960947716E-01 -5.117500346253E-01  5.396120592340E-01
1    -2.313848558423E-01 -3.534640981885E-01  1.622320350465E+00
1     2.313848558423E-01 -3.534640981885E-01  1.622320350465E+00
1    -2.685513818111E-01 -1.595442268930E+00  3.883374637167E-01
1     2.685513818111E-01 -1.595442268930E+00  3.883374637167E-01
6     0.000000000000E+00 -1.617564074356E+00 -2.137442584772E+00
6    -5.000000000000E-01  2.174005904716E+00  1.625535878919E+00
6     0.000000000000E+00 -1.878034456206E+00 -3.509064133504E+00
6    -5.000000000000E-01  3.547705781112E+00  1.875030781226E+00
6     0.000000000000E+00 -8.254292550434E-01 -4.427141344375E+00
6    -5.000000000000E-01  4.457460056891E+00  8.151187204272E-01
6     0.000000000000E+00  4.887062886314E-01 -3.959428213946E+00
6    -5.000000000000E-01  3.979328673451E+00 -4.953255812288E-01
6     0.000000000000E+00  7.435473877317E-01 -2.586261016594E+00
6    -5.000000000000E-01  2.604180742399E+00 -7.391113262251E-01
1     0.000000000000E+00 -2.454929817994E+00 -1.444263540800E+00
1    -5.000000000000E-01  1.487671817423E+00  2.468630227462E+00
1     0.000000000000E+00 -2.905089418907E+00 -3.863993126557E+00
1    -5.000000000000E-01  3.911266319567E+00  2.899107329193E+00
1     0.000000000000E+00 -1.027917934876E+00 -5.494667910270E+00
1    -5.000000000000E-01  5.526531496756E+00  1.009423820737E+00
1     0.000000000000E+00  1.321245142873E+00 -4.657530918139E+00
1    -5.000000000000E-01  4.670627343711E+00 -1.333620086721E+00
1     0.000000000000E+00  1.768230925732E+00 -2.226363241410E+00
1    -5.000000000000E-01  2.235731039811E+00 -1.760743294612E+00
ENDG
```

Figure A.8: Input geometry of syndiotactic polystyrene according to CRYSTAL [69] specification. The basis set is 6-31G with an increased exponent of the most diffuse sp-function of carbon from 0.16871448 to 0.18. The Hartree Fock energy is -614.988 536 Hartree.

Table A.1: HF energies, fundamental band gaps (E_g) and vertical excitation energies to the lowest singlet exciton state of all-*trans* polyethylene at the B3LYP/6-31G* optimized geometry of Ref. 52 compared to the CRYSCOR results.

basis set	quantity	Ref. 52	CRYSCOR
STO-3G	HF / Hartree	−77.159 644	−77.159 640
	E_g / eV	23.80	23.81
	CIS / eV	15.89	15.89
3-21G	HF / Hartree	−77.637 596	−77.637 589
	E_g / eV	17.85	17.85
	CIS / eV	12.53	12.52
6-31G	HF / Hartree	−78.036 449	−78.036 465
	E_g / eV	16.88	16.87
	CIS / eV	11.70	11.70
6-31G*	HF / Hartree	−78.068 975	−78.068 645
	E_g / eV	17.02	17.01
	CIS / eV	11.77	11.77
6-31G**	HF / Hartree	−78.075 058	−78.075 002
	E_g / eV	17.00	17.00
	CIS / eV	11.75	11.75

A.2 Supplementary data for Chapter 3

In Figs. A.9 to A.15 we provide the structural parameters and the AO basis sets (exponents and contraction coefficients), in Fig. A.16 the Hartree-Fock parameters, and in Fig. A.17 the parameters used for the localization of the WFs of our test systems. The fitting basis set was generated by adopting the GTO cc-pVDZ DF-MP2 fitting basis of Ref. 103, and converting it to a mixed cc-pVDZ (GTO/PTO) basis as described in Ref. 20.

```
LiH crystal
CRYSTAL
0 0 0
225
4.084
2
3    0.5   0.5  0.5
ENDG
3 6
0 0 7 2.0 1.0
   1469.0000000              0.0007660
    220.5000000              0.0058920
     50.2600000              0.0296710
     14.2400000              0.1091800
      4.5810000              0.2827890
      1.5800000              0.4531230
      0.5640000              0.2747740
0 0 7 2.0 1.0
   1469.0000000             -0.0001200
    220.5000000             -0.0009230
     50.2600000             -0.0046890
     14.2400000             -0.0176820
      4.5810000             -0.0489020
      1.5800000             -0.0960090
      0.5640000             -0.1363800
0 0 1 0.0 1.0
      0.18                   1.0000000
0 2 2 0.0 1.0
      1.5340000              0.0227840
      0.2749000              0.1391070
0 2 1 0.0 1.0
      0.18                   1.0000000
0 3 1 0.0 1.0
      0.20                   1.0000000
1 3
0 0 3 0.0 1.0
     13.0100000              0.0196850
      1.9620000              0.1379770
      0.4446000              0.4781480
0 0 1 0.0 1.0
      0.18                   1.0000000
0 2 1 0.0 1.0
      0.7270000              1.0000000
```

Figure A.9: Specification of the structural parameters and basis set for LiH according to the CRYSTAL [69] input syntax. The basis set originates from the cc-pVDZ basis set [113,114]. The most diffuse *s*- and *p*-type GTOs of Li are removed. The second most diffuse *s*- and *p*-type GTOs of Li are decontracted and their exponents are increased to 0.18 a.u. The exponent of the *d*- type GTOs of Li are increased to 0.20 a.u. The most diffuse *s*-type GTO of H is decontracted and its exponent is increased to 0.18 a.u.

```
Ice
CRYSTAL
0 0 0
36
4.56809668     8.39571979     7.68649018
5
8     5.000000000000E-01 -1.601578768184E-01 -6.017732631203E-02
8     4.959512687672E-17 -3.362333334428E-01  6.489954166435E-02
1     5.000000000000E-01  1.580764889115E-01  1.885982006903E-01
1     5.000000000000E-01  5.707276708341E-02  2.305373501461E-02
1    -3.331398431318E-01 -2.167393426513E-01 -1.918707552860E-02
ENDG
1 3
0 0 3 1.0 1.0
     13.0100000              0.0196850
      1.9620000              0.1379770
      0.4446000              0.4781480
0 0 1 0.0 1.0
      0.18                   1.0000000
0 2 1 0.0 1.0
      0.7270000              1.0000000
8 6
0 0 8 2.0 1.0
  11720.0000000              0.0007100
   1759.0000000              0.0054700
    400.8000000              0.0278370
    113.7000000              0.1048000
     37.0300000              0.2830620
     13.2700000              0.4487190
      5.0250000              0.2709520
      1.0130000              0.0154580
0 0 8 2.0 1.0
  11720.0000000             -0.0001600
   1759.0000000             -0.0012630
    400.8000000             -0.0062670
    113.7000000             -0.0257160
     37.0300000             -0.0709240
     13.2700000             -0.1654110
      5.0250000             -0.1169550
      1.0130000              0.5573680
0 0 1 2.0 1.0
      0.3023000              1.0000000
0 2 3 2.0 1.0
     17.7000000              0.0430180
      3.8540000              0.2289130
      1.0460000              0.5087280
```

```
0 2 1 0.0 1.0
      0.2753000             1.0000000
0 3 1 0.0 1.0
      1.1850000             1.0000000
```

Figure A.10: Specification of the structural parameters and basis set for ice according to the CRYSTAL [69] input syntax. The basis set originates from the cc-pVDZ basis set [113,114]. The most diffuse *s*-type GTO of H is decontracted and its exponent is increased to 0.18 a.u. The most diffuse *s*- and *p*-type GTOs of O are removed. The second most diffuse *s*- and *p*-type GTOs of O are decontracted.

```
Diamond
CRYSTAL
0 0 1
227
3.56679
1
6   0. 0. 0.
ENDG
6  6
0  0  9  2.0  1.0
 6665          0.000692
 1000          0.005329
  228          0.027077
   64.71       0.101718
   21.06       0.27474
   7.495       0.448564
   2.797       0.285074
   0.5215      0.015204
   0.1596     -0.003191
0  0  9  2. 0 1.0
 6665         -0.000146
 1000         -0.001154
  228         -0.005725
   64.71      -0.023312
   21.06      -0.063955
    7.495     -0.149981
    2.797     -0.127262
    0.5215     0.544529
    0.1596     0.580496
0  0  1  0.0  1.0
    0.20        1.0
0  2  3  2. 0 1.0
    9.439      0.038109
    2.002      0.20948
    0.5456     0.508557
0  2  1  0.0  1.0
    0.20        1.0
0  3  1  0.0  1.0
    0.55        1.0
```

Figure A.11: Specification of the structural parameters and basis set for diamond according to the CRYSTAL [69] input syntax. The basis set originates from the cc-pVDZ basis set [114]. The exponents of the most diffuse *s*- and *p*-type GTOs are increased to 0.20 a.u.

```
MgO crystal
CRYSTAL
0 0 0
 225
4.20
2
 12 0.    0.    0.
  8 0.5   0.5   0.5
END
12 8
0 0 10 2.0 1.0
  47390.0000000              0.346023D-03
   7108.0000000              0.268077D-02
   1618.0000000              0.138367D-01
    458.4000000              0.551767D-01
    149.3000000              0.169660D+00
     53.5900000              0.364703D+00
     20.7000000              0.406856D+00
      8.3840000              0.135089D+00
      2.5420000              0.490884D-02
      0.8787000              0.286460D-03
0 0 10 2.0 1.0
  47390.0000000             -0.877839D-04
   7108.0000000             -0.674725D-03
   1618.0000000             -0.355603D-02
    458.4000000             -0.142154D-01
    149.3000000             -0.476748D-01
     53.5900000             -0.114892D+00
     20.7000000             -0.200676D+00
      8.3840000             -0.341224D-01
      2.5420000              0.570454D+00
      0.8787000              0.542309D+00
0 0 10 2.0 1.0
  47390.0000000              0.169628D-04
   7108.0000000              0.129865D-03
   1618.0000000              0.688831D-03
    458.4000000              0.273533D-02
    149.3000000              0.931224D-02
     53.5900000              0.223265D-01
     20.7000000              0.411195D-01
      8.3840000              0.545642D-02
      2.5420000             -0.134012D+00
      0.8787000             -0.256176D+00
0 0 1 2.0 1.0
      0.18                   1.0000000
0 2 6 2.0 1.0
    179.9000000              0.538161D-02
     42.1400000              0.392418D-01
     13.1300000              0.157445D+00
      4.6280000              0.358535D+00
      1.6700000              0.457226D+00
      0.5857000              0.215918D+00
```

```
0 2 6 0.0 1.0
    179.9000000             -0.865948D-03
     42.1400000             -0.615978D-02
     13.1300000             -0.261519D-01
      4.6280000             -0.570647D-01
      1.6700000             -0.873906D-01
      0.5857000             -0.122990D-01
0 2 1 0.0 1.0
      0.18                   1.0000000
0 3 1 0.0 1.0
      0.1870000              1.0000000
8 6
0 0 8 2.0 1.0
  11720.0000000              0.0007100
   1759.0000000              0.0054700
    400.8000000              0.0278370
    113.7000000              0.1048000
     37.0300000              0.2830620
     13.2700000              0.4487190
      5.0250000              0.2709520
      1.0130000              0.0154580
0 0 8 2.0 1.0
  11720.0000000             -0.0001600
   1759.0000000             -0.0012630
    400.8000000             -0.0062670
    113.7000000             -0.0257160
     37.0300000             -0.0709240
     13.2700000             -0.1654110
      5.0250000             -0.1169550
      1.0130000              0.5573680
0 0 1 2.0 1.0
      0.3023000              1.0000000
0 2 3 4.0 1.0
     17.7000000              0.0430180
      3.8540000              0.2289130
      1.0460000              0.5087280
0 2 1 0.0 1.0
      0.2753000              1.0000000
0 3 1 0.0 1.0
      1.1850000              1.0000000
```

Figure A.12: Specification of the structural parameters and basis set for MgO according to the CRYSTAL [69] input syntax. The basis set originates from the cc-pVDZ basis set [113,114]. The most diffuse *s*- and *p*-type GTOs of Mg are removed. The second most diffuse *s*- and *p*-type GTOs of Mg are decontracted and their exponents are increased to 0.18 a.u. The most diffuse *s*- and *p*-type GTOs of O are removed. The second most diffuse *s*- and *p*-type GTOs of O are decontracted.

```
LiF crystal
CRYSTAL
0 0 0
225
3.99
2
3 0.    0.    0.
9 0.5   0.5   0.5
ENDG
3 6
0 0 7 2.0 1.0
   1469.0000000              0.0007660
    220.5000000              0.0058920
     50.2600000              0.0296710
     14.2400000              0.1091800
      4.5810000              0.2827890
      1.5800000              0.4531230
      0.5640000              0.2747740
0 0 7 2.0 1.0
   1469.0000000             -0.0001200
    220.5000000             -0.0009230
     50.2600000             -0.0046890
     14.2400000             -0.0176820
      4.5810000             -0.0489020
      1.5800000             -0.0960090
      0.5640000             -0.1363800
0 0 1 0.0 1.0
      0.18                   1.0000000
0 2 2 0.0 1.0
      1.5340000              0.0227840
      0.2749000              0.1391070
0 2 1 0.0 1.0
      0.18                   1.0000000
0 3 1 0.0 1.0
      0.20                   1.0000000
9 6
0 0 8 2.0 1.0
  14710.0000000              0.0007210
   2207.0000000              0.0055530
    502.8000000              0.0282670
    142.6000000              0.1064440
     46.4700000              0.2868140
     16.7000000              0.4486410
      6.3560000              0.2647610
      1.3160000              0.0153330
```

```
0 0 8 2.0 1.0
  14710.0000000             -0.0001650
   2207.0000000             -0.0013080
    502.8000000             -0.0064950
    142.6000000             -0.0266910
     46.4700000             -0.0736900
     16.7000000             -0.1707760
      6.3560000             -0.1123270
      1.3160000              0.5628140
0 0 1 2.0 1.0
      0.3897000              1.0000000
0 2 3 2.0 1.0
     22.6700000              0.0448780
      4.9770000              0.2357180
      1.3470000              0.5085210
0 2 1 0.0 1.0
      0.3471000              1.0000000
0 3 1 0.0 1.0
      1.6400000              1.0000000
```

Figure A.13: Specification of the structural parameters and basis set for LiF according to the CRYSTAL [69] input syntax. The basis set for Li originates from the cc-pVDZ basis set [113]. The most diffuse *s*- and *p*-type GTOs of Li are removed. The second most diffuse *s*- and *p*-type GTOs of Li are decontracted and their exponents are increased to 0.18 a.u. The exponent of the *d*-type GTOs of Li are increased to 0.20 a.u. For F, the cc-pVDZ basis set is utilized. [114]

```
SiC
CRYSTAL
0 0 0
216
4.36
2
6 .25 .25 .25
14 .0 .0 .0
ENDG
14 5
0 0 8 2.0 1.0
 149866.0    0.0001215
  22080.6    0.0009770
   4817.5    0.0055181
   1273.5    0.0252000
    385.11   0.0926563
    128.429  0.2608729
     45.4475 0.4637538
     16.2589 0.2952000
0 1 8 8.0 1.0
    881.111  -0.0003  0.0006809
    205.84   -0.0050   0.0059446
     64.8552 -0.0368  0.0312000
     23.9    -0.1079   0.1084000
     10.001   0.0134  0.2378000
      4.4722  0.3675 0.3560066
      2.034   0.5685  0.3410000
      0.9079  0.2065 0.1326000
0 1 3 4.0 1.0
      2.6668 -0.0491  0.0465000
      1.0780 -0.1167 -0.1005000
      0.3682  0.2300 -1.0329000
0 1 1 0.0 1.0
      0.193   1.0   1.0
0 3 1 0. 1.
      0.610   1.0
6  6
0  0  9  2.  1.
 6665    0.000692
 1000    0.005329
 228     0.027077
 64.71   0.101718
 21.06   0.27474
 7.495   0.448564
 2.797   0.285074
 0.5215  0.015204
 0.1596 -0.003191
```

```
0  0  9  2.  1.
 6665   -0.000146
 1000   -0.001154
 228    -0.005725
 64.71  -0.023312
 21.06  -0.063955
 7.495  -0.149981
 2.797  -0.127262
 0.5215  0.544529
 0.1596  0.580496
0  0  1  0.  1.
 0.1596  1.
0  2  3  2.  1.
 9.439   0.038109
 2.002   0.20948
 0.5456  0.508557
0  2  1  0.  1.
 0.17 1.0
0  3  1  0.  1.
 0.55    1.
```

Figure A.14: Specification of the structural parameters and basis set for SiC according to the CRYSTAL [69] input syntax. The basis set for Si is from Ref. 115. The basis set for C originates from the cc-pVDZ basis set [113]. The exponent of the most diffuse *p*-type GTO of C is increased to 0.17 a.u. according to Ref. 116.

```
Si crystal
CRYSTAL
0 0 1
227
5.48
1
14  0.0 0.0 0.0
END
14 5
0 0 8 2.0 1.0
 149866.0    0.0001215
  22080.6    0.0009770
   4817.5    0.0055181
   1273.5    0.0252000
    385.11   0.0926563
    128.429  0.2608729
     45.4475 0.4637538
     16.2589 0.2952000
0 1 8 8.0 1.0
    881.111  -0.0003  0.0006809
    205.84   -0.0050   0.0059446
     64.8552 -0.0368  0.0312000
     23.9    -0.1079    0.1084000
     10.001   0.0134  0.2378000
      4.4722  0.3675  0.3560066
      2.034   0.5685   0.3410000
      0.9079  0.2065  0.1326000
0 1 3 4.0 1.0
      2.6668 -0.0491  0.0465000
      1.0780 -0.1167 -0.1005000
      0.3682  0.2300 -1.0329000
0 1 1 0.0 1.0
      0.193   1.0 1.0
0 3 1 0. 1.
      0.610   1.0
```

Figure A.15: Specification of the structural parameters and basis set for Si according to the CRYSTAL [69] input syntax. The basis set is from Ref. 115.

```
SHRINK
8 8 8
TOLINTEG
7 7 7 20 80
FMIXING
30
TOLDEE
7
END
ENDSCF
```

Figure A.16: Parameters used in Hartree-Fock calculations according to the CRYSTAL [69] input syntax.

```
NEWK
12 12 12
1 0
LOCALWF
SYMMWF
END
VALENCE
CYCTOL
5 5 5
BOYSCTRL
8 8 100
WANDM
-2 4 1
FULLBOYS
6
END
END
```

Figure A.17: Parameters used for the localization procedure according to the CRYSTAL [69] syntax.

A.3 Supplementary data for Chapter 4

The MgO and LiH crystals with the lattice constants of 4.20 Å and 3.99 Å, respectively, were studied. Calculations employed the following parameters: shrinking factor 8, TOLINTEG 7 7 7 20 80, FMIXING 30. The corresponding LDA calculations used VWN as the correlation functional. In the DFT calculations LEVSHIFT 10 0 was used.

In the CIS calculations the $6\times6\times6$ and $7\times7\times7$ k-meshes were utilized for MgO and LiH, respectively. In both cases the PG-VDZ fitting basis set was employed.

Bibliography

[1] Fock, V. *Zeitschrift für Physik A Hadrons and Nuclei* **1930**, *61*, 126–148.

[2] Euwema, R. N.; Wilhite, D. L.; Surratt, G. T. *Phys. Rev. B* **1973**, *7*, 818–831.

[3] Pisani, C.; Dovesi, R. *Int. J. Quantum Chem.* **1980**, *17*, 501–516.

[4] Pulay, P.; Saebø, S. *Theoretical Chemistry Accounts: Theory, Computation, and Modeling (Theoretica Chimica Acta)* **1986**, *69*, 357–368.

[5] Pisani, C.; Busso, M.; Capecchi, G.; Casassa, S.; Dovesi, R.; Maschio, L.; Zicovich-Wilson, C.; Schütz, M. *J. Chem. Phys.* **2005**, *122*, 094113.

[6] Maschio, L.; Usvyat, D.; Manby, F. R.; Casassa, S.; Pisani, C.; Schütz, M. *Phys. Rev. B* **2007**, *76*, 075101.

[7] Foresman, J. B.; Head-Gordon, M.; Pople, J. A.; Frisch, M. J. *J. Phys. Chem.* **1992**, *96*, 135–149.

[8] Dunlap, B. I.; Connolly, J. W. D.; Sabin, J. R. *J. Chem. Phys.* **1979**, *71*, 3396.

[9] Dunlap, B. I. *Phys. Chem. Chem. Phys.* **2000**, *2*, 2113–2116.

[10] Davidson, E. R. *J. Comput. Phys.* **1975**, *17*, 87–94.

[11] Lipkowitz, K. B.; Boyd, D. B.; Crawford, T. D.; III, H. F. S. *Reviews in Computational Chemistry* **2007**, *14*, 31–136.

[12] Kats, D. Ph.D. thesis, Universität Regensburg, 2010.

[13] Feyereisen, M.; Fitzgerald, G.; Komornicki, A. *Chem. Phys. Lett.* **1993**, *208*, 359–363.

[14] Hättig, C.; Weigend, F. *J. Chem. Phys.* **2000**, *113*, 5154.

[15] Usvyat, D.; Maschio, L.; Manby, F. R.; Casassa, S.; Schütz, M.; Pisani, C. *Phys. Rev. B* **2007**, *76*, 075102.

[16] Pisani, C.; Maschio, L.; Casassa, S.; Halo, M.; Schütz, M.; Usvyat, D. *J. Comput. Chem.* **2008**, *29*, 2113–2124.

[17] Mintmire, J. W.; Dunlap, B. I. *Phys. Rev. A* **1982**, *25*, 88–95.

[18] Manby, F. R.; Knowles, P. J. *Phys. Rev. Lett.* **2001**, *87*, 163001.

[19] Manby, F. R.; Knowles, P. J.; Lloyd, A. W. *J. Chem. Phys.* **2001**, *115*, 9144.

[20] Schütz, M.; Usvyat, D.; Lorenz, M.; Pisani, C.; Maschio, L.; Casassa, S.; Halo, M. *Accurate Condensed-Phase Quantum Chemistry*; CRC Press, 2010.

[21] Boys, S. F. *Quantum Theory of Atoms, Molecules, and the Solid State*; Academic Press, New York, 1966; p 253.

[22] Pipek, J.; Mezey, P. *J. Chem. Phys.* **1989**, *90*, 4916.

[23] Zicovich-Wilson, C. M.; Dovesi, R.; Saunders, V. R. *J. Chem. Phys.* **2001**, *115*, 9708.

[24] Marzari, N.; Vanderbilt, D. *Phys. Rev. B* **1997**, *56*, 12847–12865.

[25] Schütz, M.; Werner, H.-J.; Lindh, R.; Manby, F. R. *J. Chem. Phys.* **2004**, *121*, 737.

[26] Loibl, S.; Schütz, M. *J. Chem. Phys.* **2012**, *137*, 084107.

[27] Évarestov, R. A.; Tupitsyn, I. I. *Phys. Solid State* **2002**, *44*, 1656–1670.

[28] Christiansen, O.; Jørgensen, P.; Hättig, C. *Int. J. Quantum Chem.* **1998**, *68*, 1–52.

[29] Trofimov, A. B.; Schirmer, J. *J. Phys. B: At. Mol. Opt. Phys* **1995**, *28*, 2299.

[30] Head-Gordon, M.; Ricoa, R. J.; Oumia, M.; Leeb, T. J. *Chem. Phys. Lett.* **1994**, *219*, 21–29.

[31] Roos, B. O.; Fülscher, M. P.; Malmqvist, P.-A.; Merchán, M.; Serrano-Andrés, L. *Quantum Mechanical Electronic Structure Calculations with Chemical Acuracy*; Kluwer Academic Publishers, Dordrecht, The Netherlands, 1995; p 357.

[32] Kats, D.; Korona, T.; Schütz, M. *J. Chem. Phys.* **2006**, *125*, 104106.

[33] Freundorfer, K.; Kats, D.; Korona, T.; Schütz, M. *J. Chem. Phys.* **2010**, *133*, 244110.

[34] Ayala, P. Y.; Kudin, K. N.; Scuseria, G. E. *J. Chem. Phys.* **2001**, *115*, 9698.

[35] Marsman, M.; Grüneis, A.; Paier, J.; Kresse, G. *J. Chem. Phys.* **2009**, *130*, 184103.

[36] Stoll, H. *Phys. Rev. B* **1992**, *46*, 6700–6704.

[37] Paulus, B. *Physics Reports* **2006**, *428*, 1–52.

[38] Nolan, S. J.; Gillan, M. J.; Alfè, D.; Allan, N. L.; Manby, F. R. *Phys. Rev. B* **2009**, *80*, 165109.

[39] Stoyanova, A.; Hozoi, L.; Fulde, P.; Stoll, H. *J. Chem. Phys.* **2009**, *131*, 044119.

[40] Suhai, S. *Phys. Rev. B* **1984**, *29*, 4570–4581.

[41] Suhai, S. *Int. J. Quantum Chem.* **1986**, *29*, 469–476.

[42] Onida, G.; Reining, L.; Rubio, A. *Rev. Mod. Phys.* **2002**, *74*, 601–659.

[43] Rohlfing, M.; Louie, S. G. *Phys. Rev. Lett.* **1998**, *81*, 2312–2315.

[44] Rohlfing, M.; Louie, S. G. *Phys. Rev. Lett.* **1999**, *82*, 1959–1962.

[45] Lucero, M. J.; Niklasson, A. M. N.; Tretiak, S.; Challacombe, M. *J. Chem. Phys.* **2008**, *129*, 064114.

[46] Friedrich, C.; Schindlmayr, A. *Computational Nanoscience: Do It Yourself!*; John von Neumann Institute for Computing, Julich, Germany, 2006; p 335–355.

[47] Suhai, S. *Int. J. Quantum Chem.* **1984**, *26*, 223–235.

[48] Hirata, S.; Bartlett, R. J. *J. Chem. Phys.* **2000**, *112*, 7339.

[49] Hirata, S.; Shimazaki, T. *Phys. Rev. B* **2009**, *80*, 085118.

[50] Grüneis, A.; Marsman, M.; Kresse, G. *J. Chem. Phys.* **2010**, *133*, 074107.

[51] Vracko, M. G.; Zaider, M. *Int. J. Quantum Chem.* **1992**, *43*, 321–326.

[52] Hirata, S.; Head-Gordon, M.; Bartlett, R. J. *J. Chem. Phys.* **1999**, *111*, 10774.

[53] Ko, C.; Malick, D. K.; Braden, D. A.; Friesner, R. A.; Martínez, T. J. *J. Chem. Phys.* **2008**, *128*, 104103.

[54] Vracko, M. G.; Zaider, M. *Int. J. Quantum Chem.* **1993**, *47*, 119–127.

[55] Vracko, M.; Champagne, B.; Mosley, D. H.; André, J. *J. Chem. Phys.* **1995**, *102*, 6831.

[56] Katagiri, H. *J. Chem. Phys.* **2005**, *122*, 224901.

[57] Hanke, W.; Sham, L. J. *Phys. Rev. B* **1975**, *12*, 4501–4511.

[58] Hahn, P. H.; Schmidt, W. G.; Seino, K.; Preuss, M.; Bechstedt, F.; Bernholc, J. *Phys. Rev. Lett.* **2005**, *94*, 037404.

[59] Shishkin, M.; Marsman, M.; Kresse, G. *Phys. Rev. Lett.* **2007**, *99*, 246403.

[60] Hummer, K.; Puschnig, P.; Ambrosch-Draxl, C. *Phys. Rev. Lett.* **2004**, *92*, 147402.

[61] Sottile, F.; Marsili, M.; Olevano, V.; Reining, L. *Phys. Rev. B* **2007**, *76*, 161103.

[62] Palummo, M.; Pulci, O.; Sole, R. D.; Marini, A.; Hahn, P.; Schmidt, W. G.; Bechstedt, F. *J. Phys.: Condens. Matter* **2004**, *16*, S4314.

[63] Izmaylov, A. F.; Scuseria, G. E. *J. Chem. Phys.* **2008**, *129*, 034101.

[64] Wannier, G. *Phys. Rev.* **1937**, *52*, 191–197.

[65] Sæbø, S.; Pulay, P. *Chem. Phys. Lett.* **1985**, *113*, 13–18.

[66] Schütz, M.; Hetzer, G.; Werner, H.-J. *J. Chem. Phys.* **1999**, *111*, 5691.

[67] Maschio, L.; Usvyat, D. *Phys. Rev. B* **2008**, *78*, 073102.

[68] Roos, B. O.; Siegbahn, P. E. M. *Modern Theoretical Chemistry, Methods of Electronic Structure*,; Plenum Press, New York, 1977; Vol. 3, p 277–318.

[69] Dovesi, R.; Saunders, V. R.; Roetti, C.; Orlando, R.; Zicovich-Wilson, C. M.; Pascale, F.; Doll, K.; Harrison, N. M.; Civalleri, B.; Bush, I. J.; D'Arco, P.; Llunell, M. *CRYSTAL09 User's Manual*; 2010, http://www.crystal.unito.it.

[70] Cloizeaux, J. D. *Phys. Rev.* **1964**, *135*, A685–A697.

[71] Kats, D.; Usvyat, D.; Schütz, M. *Phys. Chem. Chem. Phys.* **2008**, *10*, 3430–3439.

[72] Trickey, S. B.; Alford, J. A.; Boettger, J. C. *Computational Materials Science*; Elsevier, Oxford, 2004; Vol. 15, p 171.

[73] Milko, S. V. M.; Noga, J. *J. Chem. Phys.* **2006**, *124*, 034106.

[74] Burow, A. M.; Sierka, M.; Mohamed, F. *J. Chem. Phys.* **2009**, *131*, 214101.

[75] Werner, H.-J.; Manby, F. R.; Knowles, P. J. *J. Chem. Phys.* **2003**, *118*, 8149.

[76] Izmaylov, A. F.; Scuseria, G. E. *Phys. Chem. Chem. Phys.* **2008**, *10*, 3421–3429.

[77] Schütz, M.; Manby, F. R. *Phys. Chem. Chem. Phys.* **2003**, *5*, 3349–3358.

[78] Casassa, S.; Zicovich-Wilson, C. M.; Pisani, C. *Theoretical Chemistry Accounts: Theory, Computation, and Modeling (Theoretica Chimica Acta)* **2006**, *116*, 726–733.

[79] Usvyat, D.; Maschio, L.; Pisani, C.; Schütz, M. *Z. Phys. Chem.* **2010**, *224*, 441–454.

[80] Kohn, W. *Phys. Rev.* **1959**, *115*, 809–821.

[81] Cloizeaux, J. D. *Phys. Rev.* **1964**, *135*, A698–A707.

[82] Less, K. J.; Wilson, E. G. *J. Phys. C* **1973**, *6*, 3110.

[83] Christiansen, O.; Koch, H.; Jørgensen, P. *Chem. Phys. Lett.* **1995**, *243*, 409–418.

[84] Hättig, C. *Advances in Quantum Chemistry*; Elsevier, Oxford, 2005; Vol. 50, p 37.

[85] Costner, E. A.; Long, B. K.; Navar, C.; Jockusch, S.; Lei, X.; Zimmerman, P.; Campion, A.; Turro, N. J.; Willson, C. G. *J. Phys. Chem. A* **2009**, *113*, 9337–9347.

[86] Hedin, L. *Phys. Rev.* **1965**, *139*, A796–A823.

[87] Gadaczek, I.; Hintze, K. J.; Bredow, T. *Phys. Chem. Chem. Phys.* **2012**, *14*, 741–750.

[88] Buth, C.; Birkenheuer, U.; Albrecht, M.; Fulde, P. *Phys. Rev. B* **2005**, *72*, 195107.

[89] Bernasconi, L.; Tomić, S.; Ferrero, M.; Rérat, M.; Orlando, R.; Dovesi, R.; Harrison, N. M. *Phys. Rev. B 83* **2011**, *83*, 195325.

[90] Bezugly, V.; Birkenheuer, U. *Chem. Phys. Lett.* **2004**, *399*, 57–61.

[91] Fulde, P. *Theoretical Chemistry Accounts: Theory, Computation, and Modeling (Theoretica Chimica Acta)* **2005**, *114*, 255–258.

[92] Lorenz, M.; Usvyat, D.; Schütz, M. *J. Chem. Phys.* **2011**, *134*, 094101.

[93] Saunders, V.; Freyria-Fava, C.; Dovesi, R.; Salasco, L.; Roetti, C. *Molecular Physics* **1992**, *77*, 629.

[94] Varga, S. *Phys. Rev. B* **2005**, *71*, 073103.

[95] Milko, M.; Noga, J.; Varga, S. *Int. J. Quantum Chem.* **2007**, *107*, 2158–2168.

[96] Varga, S. *Int. J. Quantum Chem.* **2008**, *108*, 1518–1527.

[97] Varga, S. *J. Math. Chem.* **2011**, *49*, 1–5.

[98] Evarestov, R. A.; Smirnov, V. P. *Site Symmetry in Crystals*; Springer, 1996.

[99] Harris, F. E. *Theoretical Chemistry: Advances And Perspectives, Vol 1 (p. 147)*; Academic Press, New York, 1975.

[100] Ewald, P. P. *Annalen der Physik* **1921**, *369*, 253–287.

[101] Dovesi, R.; Orlando, R.; Civalleri, B.; Roetti, C.; Saunders, V. R.; Zicovich-Wilson, C. M. *Z. Kristollgr.* **2005**, *220*, 571–573.

[102] Pisani, C.; Dovesi, R.; Roetti, C. *Hartree-Fock Ab Initio Treatment of Crystalline solids*; Springer Verlag: Berlin, 1988; Vol. 48.

[103] Weigend, F.; Häser, M.; Patzelt, H.; Ahlrichs, R. *Chem. Phys. Lett.* **1998**, *294*, 143–152.

[104] Pisani, C.; Schütz, M.; Casassa, S.; Usvyat, D.; Maschio, L.; Lorenz, M.; Erba, A. *Phys. Chem. Chem. Phys.* **2012**, *14*, 7615–7628.

[105] Usvyat, D.; Civalleri, B.; Maschio, L.; Dovesi, R.; Pisani, C.; Schütz, M. *J. Chem. Phys.* **2011**, *134*, 214105.

[106] Souza, I.; Marzari, N.; Vanderbilt, D. *Phys. Rev. B* **2001**, *65*, 035109.

[107] Birkenheuer, U.; Izotov, D. *Phys. Rev. B* **2005**, *71*, 125116.

[108] Schmitt-Rink, S.; Chemla, D. S.; Miller, D. A. B. *Phys. Rev. B* **1985**, *32*, 6601–6609.

[109] Kats, D.; Schütz, M. *J. Chem. Phys.* **2009**, *131*, 124117.

[110] Stoll, H.; Savin, A. *Density Functional Methods in Physics*; Plenum: New York, 1985; p 177.

[111] Lichanot, A.; Gelize, M.; Larrieu, C.; Pisani, C. *J. Phys. Chem. Solids* **1991**, *52*, 1155–1164.

[112] Valenzano, L.; Noël, Y.; Orlando, R.; Zicovich-Wilson, C. M.; Ferrero, M.; Dovesi, R. *Theor. Chem. Acc.* **2006**, *117*, 991–1000.

[113] Dunning, T. H. *J. Chem. Phys.* **1989**, *90*, 1007.

[114] Prascher, B. P.; Woon, D. E.; Peterson, K. A.; Dunning, T. H.; Wilson, A. K. *Theor. Chem. Acc.* **2011**, *128*, 69–82.

[115] Nada, R.; Nicholas, J. B.; McCarthy, M. I.; Hess, A. C. *Int. J. Quantum Chem.* **1996**, *60*, 809–820.

[116] Voloshina, E.; Usvyat, D.; Schütz, M.; Dedkov, Y.; Paulus, B. *Phys. Chem. Chem. Phys.* **2011**, *13*, 12041–12047.

Erklärung

Ich erkläre hiermit an Eides statt, daß ich die vorliegende Arbeit ohne unzulässige Hilfe Dritter und ohne Benutzung anderer als der angegebenen Hilfsmittel angefertigt habe; die aus anderen Quellen direkt oder indirekt übernommenen Daten und Konzepte sind unter Angabe des Literaturzitats gekennzeichnet.

Regensburg, September 2012

Marco Lorenz